MEASUREMENT OF MAGNETIC FLUCTUATIONS
AT SMALL SPATIAL SCALES
IN THE TOKAPOLE II TOKAMAK

by

EDWARD JOSEPH HAINES

A thesis submitted in partial fulfillment of the
requirements for the degree of

Doctor of Philosophy
(Physics)

at the
UNIVERSITY OF WISCONSIN–MADISON
1991

MEASUREMENT OF MAGNETIC FLUCTUATIONS
AT SMALL SPATIAL SCALES
IN THE TOKAPOLE II TOKAMAK

Edward Joseph Haines
Under the supervision of Professor Stewart C. Prager
at the University of Wisconsin–Madison

ABSTRACT

This thesis is a presentation of the measurements of short-wavelength, high-frequency radial magnetic fluctuations performed on the Tokapole II tokamak at the University of Wisconsin–Madison. Theories of electron temperature gradient (η_e) driven turbulence predict the existence of increased magnetic fluctuation power at small spatial scales near the collisionless skin depth c/ω_{pe} and over a wide range of frequencies near and below the electron diamagnetic drift frequency ω^*_{ne}. Small magnetic probes of sizes down to 1 m m ($< \rho_i < c/\omega_{pe}$) have been constructed and used to resolve short poloidal and radial wavelength magnetic fluctuations. These probes have been used with larger probes to make comparisons of fluctuation spectra measured in various ranges of wavelength and over the range of frequencies from 10 kHz to 6 MHz in Tokapole II plasmas. A calculation of the short-wavelength, high-frequency response of an electrostatically shielded model

$\dot{B}_r$ probe has been performed to guide the interpretation of the power comparison measurements. At the higher frequencies (~500 kHz to ~2 MHz) the smaller probes measure an order of magnitude more power than the large probes. This implies that fluctuation activity is stronger at the short, c/ω_{pe}- and ρ_i-size wavelengths than at the longer wavelengths at these high frequencies and may be due to η_e turbulence. At the lower frequencies (< 250kHz), where the fluctuation levels are largest, no enhanced fluctuation power is observed at the small poloidal and toroidal wavelengths. The ratio of the fluctuation power at small scales to that at larger scales is largest inside the separatrix, at high frequencies, and in low-q (q~1) discharges. The enhancement is reduced or does not exist outside the separatrix, at low frequencies, or in the higher-q discharges. Comparisons of magnetic fluctuation spectra at various positions within the plasma, and for discharges with edge safety factor of 1, 2 and 3 are presented. The linear and nonlinear theories and numerical simulations of η_e turbulence are reviewed and compared, where possible with the experimental parameters and results.

ACKNOWLEDGMENTS

I am deeply indebted to my family for their love, support and encouragement. The love and encouragement from my parents, Edward and Hildegard, have persisted since my earliest recollections. I can never repay them for the dividends their support has paid. My *other* parents Don and Bea also furnished much encouragement which I deeply appreciate. This thesis is dedicated to my wife, Beth, and children, Meghan and Ryan. Over the years Beth has tolerated my frequent sabbaticals from being a husband and father so I could run the machine, analyze data and write this thesis. Her patience and understanding were matched only by her dedication: "Write your thesis and get a job." Her assistance and support have been equaled only by her encouragement: "*Write* your thesis and *get* a job!" Her love and devotion are rivaled only by her perseverance: "*Write your thesis and get a job!!*" Seriously, Beth's hard work and 'real job' helped us to live very comfortably during our stay in Madison. I am extremely fortunate to have Beth as my wife and Eigenfriend. And no matter how tired or frustrated I became at work, I could always count on Meg and Ryan to cheer me up. Coming home to smiling little faces, excited screams, and open little arms would instantly brighten my mood.

I would like to acknowledge my advisor, Prof. Stewart Prager, for his interest, patience and guidance. His many insightful comments and

suggestions on both experiment and theory have shaped the course of my research and my development as a scientist.

Special thanks are due to D. Kortbawi, M. LaPointe and T. Lovell (who has been called "The Keeper Of All Answers" and "The Master Of All Trades"). They taught me everything I know – that did not have to be learned by doing – about high-gain and high-frequency electronics and pulsed high-power systems. My research would certainly have taken longer to complete had it not been for the invaluable assistance each has provided.

Prof. R. N. Dexter conceived and developed the first mini-probes, and J. Goetz and I. Tan produced the first plasma-worthy prototypes. Their work was the basis for my mini-probes and was extended to the development of the micro-probes used in my thesis research. Without their contributions this thesis would not have been possible.

Special thanks are also due to Dr. Wendell Horton and coHorts at the Institute for Fusion Studies, Austin, TX, for numerous discussions concerning η_e microturbulence theory and simulation. I am grateful to Dr. D. Lindberg for sending me a copy of the LINEIGS code.

S. Assadi, G. Fleet and many others have also assisted in numerous ways during the course of my research, and I am grateful to them.

And finally, I would like to remember Mr. Jerry Jiullerat, my sixth grade science teacher, who first showed me that science could be fun.

This research was financially supported by the NSF and the USDoE. During this research I was supported primarily by MYWIFE.

CONTENTS

CHAPTER 1

Introduction

1.1 Background and Motivation

Many experimental studies have attempted to characterize the properties of long-wavelength low-frequency turbulence and transport in plasmas and relate the measurements to theory. Most of these experiments have relied on probes or electromagnetic scattering diagnostics and have tended to emphasize measurements at large spatial scales. Less experimental effort has been devoted to studying magnetic fluctuation activity at small spatial scales. This thesis is a presentation of the measurements of radial magnetic fluctuations at short wavelengths near and below the collisionless skin depth, c/ω_{pe}, where $\omega_{pe} = \left(n_e e^2/\epsilon_0 m_e\right)^{1/2}$ is the electron plasma frequency. The motivation for this work is two-fold. First, the use of very small magnetic probes permits the exploration of magnetic turbulence in ranges of short wavelength that cannot be accessed by other fluctuation diagnostic currently in use. Electromagnetic scattering techniques, primarily CO_2-laser scattering, far-infrared scattering and heavy-ion-beam probes, provide line- or volume-averaged measurements and typically cannot resolve c/ω_{pe}- or ρ_i-size spatial scales. Second, nonlinear simulations of electron-temperature-gradient-driven (η_e) turbulence[1] predict the existence of increased magnetic fluctuation power at spatial scales near the collisionless skin depth which may produce significant transport.

Magnetic probes have been a standard diagnostic in laboratory plasmas

for over 30 years[2]. They have traditionally been used to measure either equilibrium fields or fluctuating fields at low frequencies (ω^{-1} >> resistive time of probe shield) and long wavelengths (λ >> probe dimensions). In this thesis the standard diagnostic has been adapted and used in a novel way to measure magnetic fluctuations at high frequencies and short wavelengths. These new probes have been used to make the first direct observations of enhanced high-frequency fluctuation levels at c/ω_{pe} and ρ_i scales in plasmas.

During the past 3 years an effort has been underway within our group to miniaturize the magnetic probes used for measuring the fluctuating and equilibrium magnetic fields in Tokapole II plasmas. Minimizing the overall size of the probe (down to less than 1 mm, for example) affords two main advantages. First, with an overall diameter of the order of ρ_i or c/ω_{pe}, a small probe can measure magnetic fluctuations at smaller wavelengths than is possible with a larger probe. Second, the probes may be inserted deeper into the plasma current channel with less perturbation than is possible with our larger standard probes. The ability to make direct, local measurements of small-scale magnetic fluctuations well inside the plasma edge opens the door to the study of micro-turbulence.

The nonlinear simulations predict increased magnetic fluctuation power at small spatial ($\sim c/\omega_{pe}$) scales and over a wide range of frequencies near and below the electron diamagnetic drift frequency, $\omega^*_{de} = k_y v_e^2/L_n \omega_{ce}$, where k_y is the poloidal wavenumber, v_e is the electron thermal speed, L_n is the density gradient scale length, and ω_{ce} is the electron cyclotron frequency. In the Tokapole II tokamak, the drift frequency evaluated for c/ω_{pe} scale

lengths ($\lambda_y \sim c/f_{pe} \sim 12$ mm) is ~ 700 kHz, while for ρ_i scale lengths ($\lambda_y \sim \rho_i \sim 2$ mm) it is ~ 3 MHz. Small magnetic probes of sizes down to 1 mm ($< \rho_i$) have been constructed and used to resolve short poloidal and radial wavelength magnetic fluctuations. These probes have been used with larger probes to make comparisons of fluctuation spectra measured in various ranges of wavelength and over the range of frequencies from 10 kHz to 6 MHz in Tokapole II plasmas. At the higher frequencies (~0.5 MHz to ~3 MHz) the small probes have measured as much as 10 to 20 times more fluctuation power than large probes. This implies that the short wavelengths resolved by the small probes contain greater levels of fluctuation power than the long wavelengths resolved by the larger probe at these high frequencies. At the lower frequencies (<100 kHz) small and large probes measure nearly equal amounts of power. A detailed boundary-value calculation of the diffusion of the fluctuating magnetic field into a model $\dot{B}_r$ probe gives the short-wavelength and high-frequency response of the probe and is used to guide the interpretation of the experimental results.

1.2 Organization of this Thesis

Presented in this thesis are the comparisons of radial magnetic fluctuation spectra measured at small spatial scales down to the collisionless skin depth and over a wide range of frequencies. The Tokapole II Tokamak and its plasmas and diagnostic systems will be discussed in Chapter 2. The magnetic probes and amplifier systems used in the experiments will also be discussed in detail.

Chapter 3 contains a discussion of several models of microturbulence and focuses on those that relate to the small-scale magnetic fluctuation measurements. The emphasis of Chapter 3 is a review of the features, assumptions, and predictions of the linear and nonlinear models of η_e turbulence. This chapter does not survey the theories of anomalous transport in plasmas. It is intended to provide a basis on which to characterize and understand the results of the power comparison experiments.

The experimental results and their relation to the theoretical models will be discussed at length in Chapter 4. Finally, Chapter 5 contains a brief summary of the results of this thesis and a few suggestions for those pursuing related work.

Occasionally, reference will be made in this thesis to University of Wisconsin–Madison PLP documents and Ph.D. Theses. The PLP's are unpublished internal reports or preprints of the Plasma Physics Group. Copies of these reports and Ph.D. theses may be obtained by writing to the group at the Department of Physics, University of Wisconsin–Madison, 1150 University Avenue, Madison, WI 53706.

References

[1] W. Horton, B. G. Hong and W. M. Tang, Phys. Fluids 31(10), 2971 (1988).

N. Bekki, W. Horton, B.-G. Hong and T. Tajima, Institute for Fusion Studies Report #364, University of Texas–Austin, February, 1989.

W. Horton, B.-G. Hong and T. Tajima, Comments Plasma Phys. Contr. Fusion E 13(4), 207 (1990).

W. Horton, S. Hamaguchi, C.-B. Kim, presented at U.S.-Japan Workshop on Fluctuations in RFP and ULQ Plasmas, University of Wisconsin–Madison, Madison, WI, 1990.

[2] R. H. Loveberg, Annals of Physics 3, 311 (1959).

CHAPTER 2

The Tokapole II Tokamak and its Diagnostic Systems

2.1 The Tokapole II Tokamak

The experiments described in this thesis were performed on the Tokapole II tokamak at the University of Wisconsin–Madison[1]. Shown in Figure 2.1 without diagnostic hardware, the Tokapole II tokamak is a small, 4-node poloidal divertor tokamak that can be operated over a relatively wide range of edge safety factor, $q_a \sim 0.6$ to 3.5. Only the general machine description and details relevant to the experiments described in this thesis will be presented in this section. The physics and engineering considerations of the design of Tokapole II are summarized in references [2], [3] and [4].

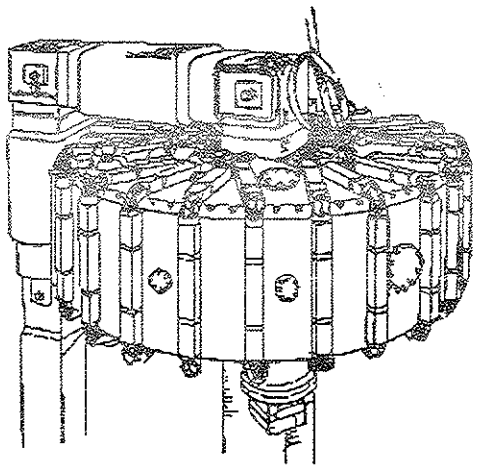

Figure 2.1. The Tokapole II Tokamak shown without diagnostic hardware.

The vacuum vessel is an aluminum torus with a 50 cm major radius and a square cross section (Figure 2.2). The conducting walls are 3 cm thick and have a toroidal and poloidal gap to allow the toroidal magnetic field and electric field to enter the vacuum vessel. The poloidal magnetic divertor configuration is formed by four inductively driven rings. Each ring is supported at three points by high-strength insulated rods. Because the cross section of Tokapole II is square, a Cartesian coordinate system is often used to specify positions within the machine. By convention, the horizontal and vertical directions are labeled by an x and y axis, respectively, with the origin of the coordinate system located at the geometric center of the vacuum vessel. Positive values of x lie toward the outer wall, and positive y lie above

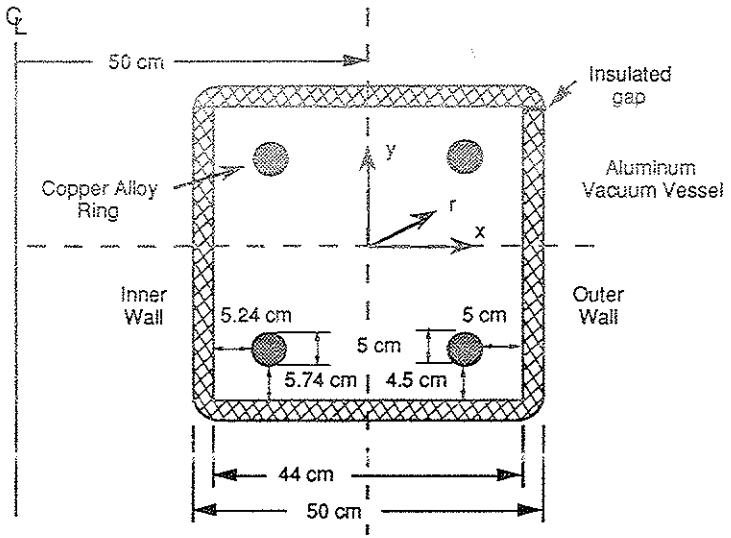

Figure 2.2. Cross section of the Tokapole II Tokamak

the midplane. A polar coordinate system originating at the geometric center of the vacuum vessel is also used. All values of plasma radii quoted in this thesis are measured from the geometric axis of the machine rather than from the magnetic axis of the discharge.

The main vacuum pumping system is a Sargent-Welch 1500 l/s turbomolecular pump. Two titanium sublimators provided additional pumping via titanium gettering of the inner wall of the vacuum vessel. Vacuum pressures and quality were monitored on a Bayard-Alpert ionization gauge and a quadrupole gas analyzer[5]. Typical base pressures obtained were in the mid 10^{-7} Torr range.

Diagnostic access for the magnetic probes described in this thesis was provided by numerous 1.5 inch ports located on the side, top and bottom of the machine. Most of these ports were fitted with air lock valves designed to pass and seal on a 1/4 inch diameter probe body or assembly.

The toroidal magnetic field is generated by 96 turns of 4/0 welding cable wound poloidally around the vacuum vessel. The windings are driven directly by a 78 mF, 5 kV capacitor bank configured as a 2-stage pulse forming network. The bank is switched by a class E ignitron and is passively crowbarred at peak field by a second class E ignitron. The pulse forming network and the passive crowbar maintain a relatively flat toroidal field for 10 to 15 ms. Typical values of toroidal field in the experiments described in this thesis ranged from 3.0 kG to 5.3 kG. Routine conditioning of the vacuum vessel walls and probes is accomplished by rapidly pulsing low-current, low-field discharges. Rapid-pulse cleaning was typically done at the

beginning of each run day or after one or more new probes have been inserted into the machine.

The poloidal magnetic field is generated by the inductively driven toroidal plasma current and ring currents. The plasma and rings constitute the secondary of an iron core transformer with a 0.17 V s flux swing (total reversed-biased). The primary winding consists of 80 turns of 2 AWG wire wound on the core in a 40:1 turns ratio configuration. The primary windings are driven by a 7.5 mF, 5 kV capacitor bank which is switched by a class E ignitron. A bank of 960 mF, 450 V electrolytic capacitors wired through a diode stack serves as a power crowbar which clamps the voltage at the poloidal gap at the peak value of the current. The circuit also contains an optional damping resistor.

In the absence of plasma the magnetic field generated by the current induced in the four internal rings is an octupole field configuration with a single null (x-point) near the center of the machine as shown in Figure 2.3. The addition of toroidal plasma current flowing in the same direction as the current in the rings modifies the flux plot as shown in Figure 2.4. Four x-points are formed, one between each of the rings and the plasma current channel. The flux surface called the separatrix separates the private flux surfaces that enclose any one current carrier from the common flux surfaces that enclose all the current carriers. In magnetically limited discharges (without material limiters) the majority of the plasma current is contained in the current channel[6][7] located in the central flux region inside the separatrix. However, some current and plasma exist outside the separatrix.

Material limiters consisting of stainless steel plates can optionally be inserted to the separatrix to limit the current flowing outside the separatrix. The

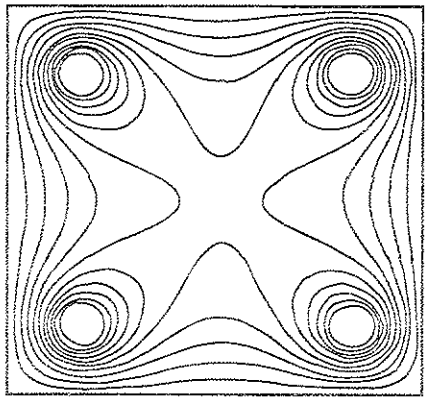

Figure 2.3. Poloidal flux plot in the absence of plasma current.

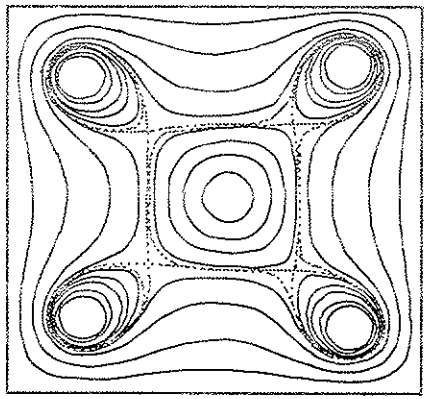

Figure 2.4. Poloidal flux plot with plasma current. Flux plot shows typical shape and location of the separatrix (dotted line) and the common and private flux regions.

characteristics of plasmas produced in materially limited discharges are generally different from those produced in magnetically limited discharges [7] (i.e., those with the material limiters retracted). For all the data presented in this thesis the discharges were magnetically limited.

2.2 Plasma Characteristics

The results presented in this thesis are organized by the edge safety factor, q_a, of the discharges in which the data was taken. Because the edge of Tokapole II plasmas is located approximately at the separatrix, a $q = \infty$ surface, the value quoted for q_a is an effective edge safety factor. The effective q_a for Tokapole II plasmas is the safety factor of a cylindrical plasma with the same plasma current I_p and toroidal field B_t and the same cross sectional area as that enclosed by the separatrix in Tokapole II. The value of q_a and other general discharge parameters are calculated using a circuit model of the Tokapole II device and plasma[8]. The inputs to the model are the readily measurable quantities ion saturation current J_{sat}, toroidal magnetic field B_t, poloidal gap voltage V_{pg}, and total ring current I_R as a function of time during the discharge. A Langmuir probe positioned between the upper-outer ring and the wall is used to measure J_{sat}. The effective edge safety factor is determined by B_t, I_p and I_R. Based on various assumptions about the Tokapole II plasmas, its drive systems and the vacuum vessel, the model provides estimates of the time histories of plasma radius a, edge safety factor q_a, loop voltage V_{loop}, I_p, ohmic heating power P_{OH}, electron temperature T_e, average electron density n_e, and electron energy confinement time τ_E.

Figure 2.5 shows a timing diagram of several key events near the end of a typical charging cycle. A fast piezoelectric valve is used to puff hydrogen gas into the vacuum vessel 16.66 ms prior to pulsing the poloidal field. Additional gas can be puffed into the machine at later times for an extra measure of control over the time history of the plasma density. The toroidal field is pulsed 9ms before the poloidal field and is passively crowbarred at peak field to achieve a relatively flat B_t during the discharge. Approximately

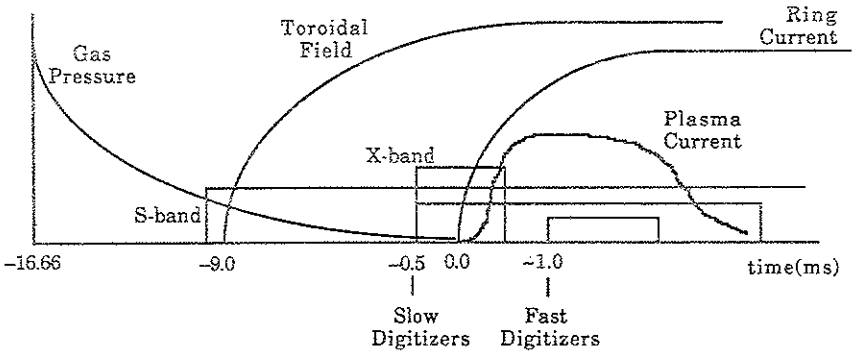

Figure 2.5. Schematic of timing of events near the end of a charging cycle.

10 kW of preionizing X-band microwaves (9.0 GHz; fundamental frequency for ECH in 3.2 kG fields) are pulsed 0.5 ms before B_p is fired. The start-up phase of the discharge is assisted by 100 W of continuous-wave S-band microwaves (2.45 GHz for ECH in 1.1 kG fields) and a hot emissive probe located 1cm from the inner wall of the machine. The slow digitizers (100 kHz and 1 MHz), which were used primarily for storing general diagnostic information, were triggered 0.5 ms before the poloidal field to allow for a

measurement and subsequent subtraction of any DC offset. The fast digitizers (typically run at 20 MHz) were used for storing both the low- and high-frequency $\dot{B}$ signals. With only 32 kilobytes of memory, the fast digitizers have a relatively short total record length and were triggered after the start-up phase of the discharge, typically at ~1 ms after firing B_p.

The experiments described in this thesis were performed in discharges with nominal q_a of 1, 2 and 3. The effective edge q was varied by changing the plasma current and the toroidal magnetic field. Figure 2.6 shows the plots of I_p and q_a for typical shots. The shaded region on each pair of plots indicates the times where 'acceptable' data records could be chosen for analysis. In this region the $\dot{B}$ signals had to be relatively free from erratic behavior associated with the start-up phase of the discharge and soft x-ray activity. In general, the range of 'acceptable' data records corresponded closely to the portion of the discharge where q_a was fairly flat and approximately equal to the nominal edge q values of 1, 2 and 3. However, the values of the plasma currents in the range of 'acceptable' data records decreased somewhat as q was increased. I_p was fairly constant with respect to variation in shot number and nominal edge q value. The value of B_t during the discharge increased from ~3 kG at $q_a = 1$ to ~5.25 kG at $q_a = 3$. At a given q_a and during the 'acceptable' data record region, B_t was fairly flat in time and constant as a function of shot number. Nearly all the variation in the values of B_t averaged over different shots was due to warming of the B_t winding and transmission lines with time. The warming gradually increased the resistance in the B_t circuit and reduced slightly the values of

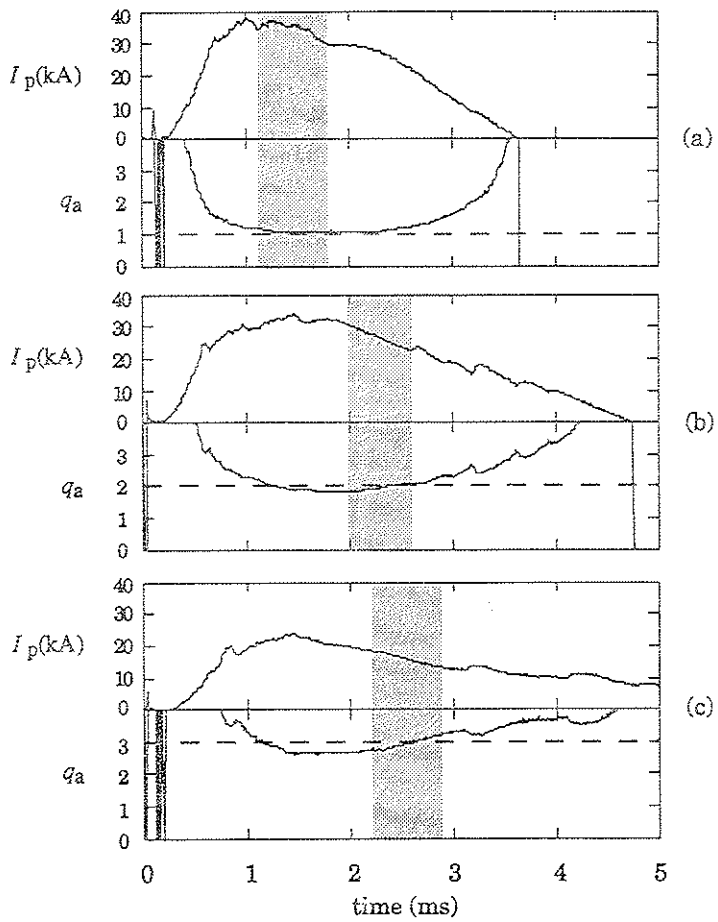

Figure 2.6. Typical plots of plasma current and effective edge q for (a) $q_a = 1$, (b) $q_a = 2$ and (c) $q_a = 3$ discharges. The shaded regions indicate the portions of the discharges analyzed.

B_t. The total variation of B_t from all sources was less than 1% in nearly all cases. Table 2.1 summarizes several of the equilibrium characteristics of the Tokapole II discharges described above. The approximate values of the

line-averaged density and temperature information were taken from reference [7].

Table 2.1 Summary of approxiamate equilibrium characteristics of Tokapole II discharges for experiments described in this thesis. The line-averaged density is a floor-to-ceiling average, whereas the core-average is a separatrix-to-separatrix average.

Nom. q_a	I_p (kA)	B_t (kG)	n ($\cdot 10^{12}$ cm^{-3}) line-av	core-av	T_e(eV) edge	core	T_i (eV)
1	30	3.2	~6	~12	~30	80-100	~50
2	25	5.2	~5	~10	~50	80-100	~40
3	20	5.3	~4	~8	~30	~100	~30

2.3 General Diagnostics

In addition to the diagnostic information obtained from the circuit model described above, Tokapole II has three diagnostic systems that are used primarily for assessing discharge behavior and conditioning.

Soft X-Ray Array

Soft x-ray emissions between 60 eV and 300 eV are measured with an array of polypropylene-filtered, surface barrier diodes. The side soft x-ray (SXR) array measures emissions along seven equally spaced parallel chords through the center, top and bottom of the plasma from the side of the machine. The SXR signals are a fairly sensitive indicator of discharge reproducibility and aid in the process of selecting low-frequency and high-frequency $\dot{B}$ signal data records to be analyzed.

Impurity Radiation Array

Impurity radiation is monitored by an array of four filtered photomultiplier tubes directed at the geometric center of the machine. Each has a different filter for monitoring a specific impurity source. The CIII line measures the contribution of hydrocarbon impurities. A strong NIII radiation line typically indicates an air leak or excessive deterioration of a boron nitride probe shield assembly. The OIII line monitors the presence of water, many organic contaminants and air. Finally, the CuI radiation line provides a measure of how strongly the plasma is interacting with the beryllium-copper poloidal divertor rings.

Microwave Interferometer

Tokapole II has a 70 GHz digital fringe shift interferometer[9] for measuring the line-average density. The line average is effectively performed across the entire length of the inside of the machine through the center. This region includes the scrape-off region outside the separatrix where the density is as much as an order of magnitude lower than in the current channel[7]. Thus, the line-averaged core density (top separatrix to bottom separatrix) is roughly a factor of 2 larger than the nominal line-averaged density (floor-to-ceiling).

For the majority of the experiments described in this thesis, however, the interferometer was turned off. When high-frequency $\dot{B}$ signals are being stored, the high-gain, high-frequency probe-amplifier system is a sensitive detector of interference at 1 MHz (and harmonics) generated by the digital section of the interferometer.

2.4 Magnetic Probes and Amplifier Systems

2.4.1 Magnetic Probe Design and Construction

In the past we have used 1/4 inch (6.35 mm) OD (outer diameter) cylindrical probe jackets (ID ~ 0.200 in.) made of a thin-wall stainless-steel tube surrounded by a thin, close-fitting, non-conducting cylindrical particle shield made of boron nitride. The steel tube serves as an electrostatic shield and provides structural support for the fragile boron nitride piece. The 1/4 inch magnetic probes are described in greater detail in references [7] and [13].

More recently our efforts to develop smaller "mini-probes" (OD~2.0 mm to 2.5 mm) and "micro-probes" (OD ~1 mm) have produced two types of electrostatic and particle shield designs. The first, a cylindrical boron-nitride-clad thin-wall stainless-steel tube design, is a scaled-down version of the "standard" 1/4 inch probe jacket design. The second design is a cylindrical graphite tube that is closed at one end and serves as both particle shield and electrostatic shield. Because the stainless-steel tube is not required for structural support or electrostatic shielding in this design, precious extra thousandths of an inch are made available for reducing further the overall OD of the probe (for micro-probes) or for allowing larger, more sensitive coils inside the probe. In addition, the graphite shields, because of their larger resistivity, do not attenuate the high-frequency magnetic fluctuations as strongly as the stainless steel shields. The mini-probes are described in greater detail in references [10] and [14].

The micro-probes were developed for the experiments described in this

thesis. A micro-probe is similar to the graphite-shielded version of the mini-probes except that the micro-probe has been optimized for minimum overall diameter. The main differences between mini- and micro-probes are the size of the wire used, the type of coil form the wire is wound on, and the shape and thickness of the graphite shielding. Table 2.2 summarizes the physical characteristics of the probes used in this thesis.

		1/4" (6.35 mm) Probe	2 mm Probe *	1 mm Probe
Coil	radius (mm)	1.5	0.37	0.125
	length (mm)	0.5	2.0 & 0.6	2.4
	low-freq A_{eff} (mm^{-2})	50	37 & 10	10
	wire size (AWG, μm)	50, 33	48, 39 & 50, 33	50, 33
Shield	material	stainless	graphite	graphite
	resistivity (μΩ·cm)	90	2032	2032
	outer radius (mm)	2.67	1.0	0.5
	inner radius (mm)	2.54	0.56	0.33
	wall thickness (mm)	0.11	0.47	0.19

* two versions: short and long coil length

Table 2.2. Summary of properties of the various sizes of probes used in the magnetic fluctuation measurements.

The coil was wound with AWG #50 HML-coated magnet wire, the smallest commercially available stock magnet wire. The wire is coated with a double layer of ML high-temperature insulation. The maximum 'theoretical' diameter of the wire is 0.0014 inches (35.6 μm) and gives a

turns density of about 28/mm. (Ultra-fine wire is commonly specified directly by its resistivity per unit length and indirectly by a calculated theoretical diameter and AWG number, so the actual diameter and turns density of the wire may vary slightly.)

The radial coil of the micro-probe was wound on a 0.012 inch (0.305 mm) quartz tube. The fine quartz tube was made by heating and then stretching a standard piece of 1/2 inch quartz tube. As the soft quartz stretches its diameter shrinks preserving the hole in the center and the ratio of diameter to wall thickness. The coil was wound in two ~63-turn layers, and had a low-frequency effective area of just under 10 mm^2. The length of the finished coil was 2.4 mm. The coil was painted with a thin layer of Sauereisen #29 high-temperature cement to hold the turns together and to provide electrical insulation from the close-fitting conducting shield. The leads were twisted and fed down the inside of the coil form and insulated support structure to a vacuum feed-through. The effective area of 10 mm^2 was an operationally defined lower limit required to resolve the high-frequency magnetic fluctuations with the high-frequency amplifier/filter system when the coils were located in the edge of Tokapole II plasmas. When the coil was near the separatrix in the higher q_a discharges, which generally have smaller magnetic fluctuation levels, the 10 mm^2 effective area was barely sufficient to bring the high-frequency probe signals out of the amplifier noise.

The graphite shield used for the micro-probe was machined from graphite rod and is comparable in many respects to the graphite mini-probe shields except at the end of the shield where the micro-coil is located. For

strength and support most of the 11 cm length of the micro-probe shield has a relatively large diameter (2.74 mm) and wall thickness (0.58 mm). The end of the shield containing the micro-coil was tapered to a diameter of 1.0 mm with ~0.1 mm walls. The shield was plugged at the end with a short graphite cap.

2.4.2 Response of $\dot{B}_r$ Probes to Short-Wavelength, High-Frequency Magnetic Fluctuations

Miniaturized probes seem well suited to accessing the small-wavelength regime of plasma fluctuation phenomena. However, as the size of the magnetic probe approaches the short wavelengths of interest, the wavelength resolution of the shielded coil (the λ-dependence of the probe response) becomes strongly dependent on (1) the usual *attenuation* and *phase shift* associated with the diffusion of a magnetic field through the electrostatic shield, and (2) '*modulation*' effects resulting from spatial averaging of the magnetic flux over the area and length of the coil. A $\dot{B}_r$ probe in a magnetized plasma measures a radial fluctuation spectrum that is averaged over all axial and transverse wavelengths larger than some minimum resolvable wavelengths. The wavelength-dependent modulation effects determine the minimum resolvable wavelengths for a particular probe and are important when the wavelengths of interest are comparable to the probe and coil dimensions.

The attenuation and phase shift are important at higher frequencies where the electromagnetic skin depth in the shielding material is comparable

to or smaller than the thickness of the shield wall. The effects of the attenuation and phase shift alone (i.e. in the long-wavelength limit) on a particular probe can be taken into account by a straightforward bench calibration of amplitude and phase. However, the modulation effects due to short wavelengths cannot as easily be measured because appropriate short-scale-length magnetic field variations are not easily produced on the bench. Even if a wavelength calibration were practical, one would need to apply it to the data in k-space. However, measurements of the necessary k spectra are also difficult and have not been performed.

Because the wavelength-dependent effects are not taken into account by calibration, I have derived expressions for the response of a model probe[11] which are used to estimate the minimum resolvable wavelengths for a particular probe. A prescribed fluctuating field is assumed outside the model probe, and the magnetic diffusion boundary-value problems are solved for the fields, first in the conducting shield region and then in the dielectric region where the coil is located. The emf induced in the coil is calculated as a function of frequency and the transverse and axial wavelengths. Estimates of the minimum resolvable wavelengths are then inferred from the wavelength dependence of the emf. The results are valid for short wavelengths, high frequencies and realistic probe geometries.

Figure 2.7 shows an end view of the model $\dot{B}_r$ probe. An N-turn radial pick-up coil of radius r_c and length L_c is centered on the z-axis (which corresponds to the minor radial direction in the torus). The coil is surrounded by a long ($>> L_c$), concentric, conducting tube of inner radius a, outer radius

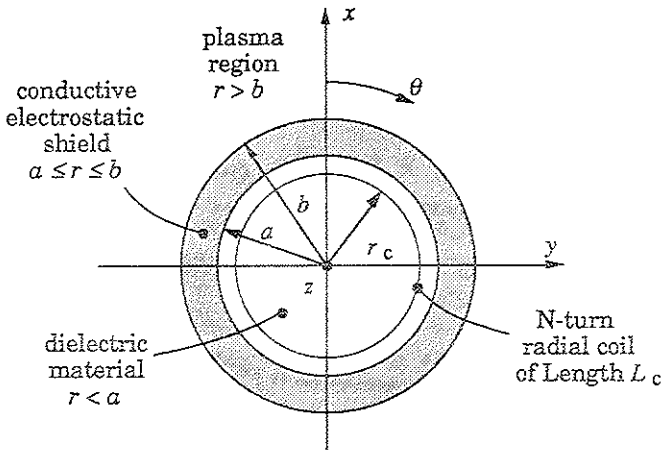

Figure 2.7. End view of the model $\dot{B}_r$ probe. The probe x, y, and z directions correspond to the plasma toroidal, poloidal and radial directions, respectively.

b and conductivity σ. (In practice, the long-shield approximation is justified by placing the coil several coil diameters or coil lengths away from the end cap of the shield.) The coil has a uniform density of turns $n = L_c / N$, and the wire diameter is much smaller than the shortest radial wavelengths of interest. The plasma outside the tube is assumed to produce a short-wavelength, fluctuating, axial magnetic field at the outer probe surface. In general, the fluctuating field will have spatial variations in all plasma directions. The axial component at the outer surface $r = b$ of the probe may take the basic form

$$B_z(r=b,\theta,z,t) = B_0 \sin\omega t \cos(k_x b\cos\theta)\cos(k_y b\sin\theta)\cos k_z z, \qquad (2.1)$$

where k_x, k_y and k_z are the toroidal, poloidal and radial wave numbers. The standing wave form is a natural choice for the basic form of the field variations because it is separable. More complex external surface fields, including traveling waves, can be formed from combinations of such terms for various k_x, k_y, k_z, and ω. Because the boundary-value problems and the boundary conditions are linear, the solutions can be generalized accordingly. The other components of B, though nonzero if $k_z \neq 0$ due to the condition $\nabla \cdot \mathbf{B} = 0$, do not effect the coil signal.

The magnetic field will soak through the conducting electrostatic shield and into the dielectric region in accordance the generalized wave-diffusion equation for B,

$$\nabla^2 \mathbf{B} = \mu\sigma\frac{\partial \mathbf{B}}{\partial t} + \mu\epsilon\frac{\partial^2 \mathbf{B}}{\partial t^2}. \qquad (2.2)$$

Because the emf induced in the radial pick-up coil depends only on the axial component of the field in the dielectric region, we seek only the solution for $B_z(r,\theta,z,t)$. In cylindrical coordinates the generalized wave equation for B gives three PDE's: two coupled equations in B_r and B_θ, and the B_z equation,

$$\left(\frac{\partial^2}{\partial r^2}+\frac{1}{r}\frac{\partial}{\partial r}+\frac{1}{r^2}\frac{\partial^2}{\partial\theta^2}+\frac{\partial^2}{\partial z^2}-\mu\sigma\frac{\partial}{\partial t}-\mu\epsilon\frac{\partial^2}{\partial t^2}\right)B_z = 0, \qquad (2.3)$$

subject to the appropriate boundary conditions.

There are two boundary-value problems to solve: a diffusion BVP in the

conducting shield region ($a \le r \le b$, $\sigma \neq 0$) and a wave BVP in the dielectric region ($r \le a$, $\sigma = 0$). Each BVP can be solved by the method of separation of variables with a substitution of the form $B_z(r,\theta,z,t) = R(r)\,\Theta(\theta)\cos k_z z\, e^{i(\omega t + \phi)}$. The general solution in the conducting region is matched to the field at the outer surface $r=b$ given by Eq. (2.1). And the general solution in the dielectric region is matched to the solution in the conducting region at the inner surface $r=a$. In the limit of long toroidal wavelengths ($k_x = 0$), the final form of the axial field in the dielectric region is

$$\begin{aligned} B_z(r,\theta,z,t) = B_o \sum_{n=0}^{\infty} & \frac{\overline{M}_n(a/\delta, k_z\delta)}{\overline{M}_n(b/\delta, k_z\delta)} \\ & \times \sin\left[\omega t + \overline{\vartheta}_n(a/\delta, k_z\delta) - \overline{\vartheta}_n(b/\delta, k_z\delta)\right] \\ & \times \frac{J_n\left(k_z r \cdot i\sqrt{1-(\omega/k_z c)^2}\right)}{J_n\left(k_z a \cdot i\sqrt{1-(\omega/k_z c)^2}\right)} \\ & \times \left[c_n(k_y b)\cos n\theta + s_n(k_y b)\sin n\theta\right] \\ & \times \cos k_z z \end{aligned} \tag{2.4}$$

where $J_n(z)$ is the Bessel function of the first kind of integer order, $\overline{M}_n(r/\delta, k_z\delta)$ and $\overline{\vartheta}_n(r/\delta, k_z\delta)$ are defined as the amplitude and phase of $J_n\left(i^{3/2}\frac{r}{\delta}\sqrt{1-ik_z^2\delta^2}\right)$, and $\delta = \sqrt{\mu\sigma\omega}$ is the is the resistive scale length in the conducting shield material at frequency ω. This scale length is *not* an e-folding length because the dependence is not strictly exponential. At 1MHz, δ~1.6 m m for graphite, and δ ~ 0.3 m m for stainless steel. By comparison, typical mini- and micro-probe scales vary from 0.3 m m to 2.7 m m (Table

2.2). Thus, the quantity r/δ is typically of order unity, and the shield soak-in effects due to shield dimensions as well as conductivity will play an important role in determining the probe response. The coefficients $c_n(k_y b)$ and $s_n(k_y b)$ are proportional to $J_n(k_y b)$. In particular, the n=0 coefficients,

$$c_0(k_y b) = J_0(k_y b) \text{ and } s_0(k_y b) = 0, \tag{2.5}$$

are the most important coefficients in the calculation of the emf. The expression for B_z, Eq. (2.4), is valid for all transverse and axial wavelengths and includes the effects of high frequencies and realistic probe characteristics. A spatial variation in the toroidal direction as well as spatial phase shifts in each direction are neglected in Eqs. (2.4) and (2.5) but can be easily included[11]. However, as is discussed later, these additional effects do not significantly alter the basic features of the wavelength response of the probe.

The first and second factors in the solution for the field in the dielectric region, Eq. (2.4), give the attenuation and phase shift associated with the diffusion of B_z through the resistive shield. The third factor contains the r dependence and also contributes to the overall attenuation and phase shift. Because $\omega/k_z c = \lambda_z^{\text{plasma}}/\lambda^{\text{vacuum}} << 1$, however, the Bessel function ratio simplifies (via $J_n(ix)/J_n(iy) = I_n(x)/I_n(y)$) to a real quantity. Thus the contribution from the third factor to the overall phase shift is negligible. The θ dependence of the axial field (fourth factor) is set by the boundary condition at the plasma-shield boundary, $r=b$, and is *independent* of radius. The coefficient c_0 depends only on the transverse wavelengths and the outer

diameter of the probe and is predominantly responsible for determining the minimum resolvable transverse wavelengths. The z dependence (last factor) is preserved because no boundary condition was imposed on the axial behavior of the solutions – the shielding tube is assumed to be infinitely long. In addition, because it is the only z-dependent quantity in the solution, the $\cos k_z z$ factor determines the minimum resolvable axial wavelength.

The emf induced in the radial coil by B_z is calculated directly from Faraday's law, $\mathcal{E}(k_x, k_y, k_z, \omega) = -\partial_t \Phi_{B_z}$, and gives the wavelength and frequency dependence of the probe response. The axial field B_z is integrated over the area of the coil and along its length to obtain the magnetic flux Φ_{B_z}. Only the n=0 term survives the integration over θ, and a subsequent integration over r gives a factor of A_c, the single-turn area of the coil. The ratio of the peak emf $\mathcal{E}^{\max}$ induced in the shielded coil to the peak emf $\omega N B_0 A_c$ induced in an identical unshielded coil in a uniform harmonically varying field of the same amplitude is

$$\frac{\left|\mathcal{E}^{\max}\right|}{\omega N B_0 A_c} = \underbrace{\frac{\overline{M}_0(a/\delta, k_z\delta)}{\overline{M}_0(b/\delta, k_z\delta)}}_{1} \underbrace{\left|J_0(k_y b)\right|}_{2} \underbrace{\frac{2I_1(k_z r_c)}{k_z r_c}}_{3} \underbrace{\frac{1}{I_0(k_z a)}}_{4} \underbrace{\left|\frac{\sin k_z L_c}{k_z L_c}\right|}_{5}. \tag{2.6}$$

The phase shift between the emf induced in the shielded and unshielded coils is

$$\Delta\varphi = \overline{\vartheta}_n(a/\delta, k_z\delta) - \overline{\vartheta}_n(b/\delta, k_z\delta). \tag{2.7}$$

The high-frequency, short wavelength response of the probe is a complicated function of all 7 plasma and probe parameters, λ_y, λ_z, r_c, L_c, a, b, and δ (8 parameters if finite λ_x is included). However, the interpretation of each part of the overall response is fairly straightforward. The features of the response are due primarily to (1) the *attenuation* and *phase shift* of the magnetic field caused by the diffusion through the conducting shield and (2) the *spatial averaging* of the axial field over the volume of the coil. The spatial averaging gives rise to the wavelength-dependent features of the response. Each factor in the probe response, Eq. (2.6), is discussed in greater detail below.

Factor 1 in the probe response is the attenuation due to the electrostatic shield but includes the effects of high frequencies, short wavelengths and cylindrical geometry. The attenuation factor always lies between 0 and 1 and the phase shift always lies between $-\pi/2$ and 0. The attenuation and phase shift approach 1 and 0, respectively, in the limit of thin shield walls, $b - a \to 0$. (This qualitative behavior was built into the solution as a condition to eliminate an unphysical part of the general solution in the conducting region[11].) For a given probe (fixed a, b) the attenuation and phase shift depend not only on frequency but also on the axial wavelength λ_z. Thus, a complete calibration for attenuation and phase shift at high frequency and short wavelength requires sweeping both f and λ_z. Bench calibrations of the frequency effects in locally uniform fields ($\lambda_z \to \infty$) are routinely performed. However, calibrations for $\lambda_z \sim \delta$ at high frequency are very

difficult. The existence of a finite axial wavelength modifies the shield attenuation factor [1] in Eq. (2.6). A given probe at a given frequency (fixed δ, a, and b) will attenuate more strongly an axial field with a finite λ_z than a field with no or very long axial variation:

$$\frac{\overline{M}_0(a/\delta, k_z\delta)}{\overline{M}_0(b/\delta, k_z\delta)} \le \frac{\overline{M}_0(a/\delta, 0)}{\overline{M}_0(b/\delta, 0)}. \qquad (2.8)$$

Equality holds only for $k_z\delta = 0$. This behavior can be readily inferred from the definition of $\overline{M}_0$ and the contour plots of $|J_0(z)|$ in the complex plane found in Ref. [12]. The variation of the attenuation factor [1] with f and λ_z is plotted in Figure 2.8(b).

Averaging the axial field over the area and length of the coil gives the remaining four factors in the probe response, Eq. (2.6). The θ dependence of the external field at the outer surface is contained in compound trigonometric functions which can be expanded as Fourier-Bessel series in $c_n(k_y b)\cos n\theta$ and $s_n(k_y b)\sin n\theta$. In general, the series coefficients c_n and s_n depend only on the shield outer radius b and the transverse wavelength λ_y (and λ_x, if included). The integral over θ picks out only the $n=0$ term, and the coefficient $c_0(k_y b) = J_0(k_y b)$ therefore determines the transverse wavelength behavior of the probe response. If the finite toroidal wavelength λ_x had been retained, the transverse portion of the response, factor [2], would have been modified to $|J_0(k_x b)||J_0(k_y b)|$. Thus, the sensitivity of the probe to both transverse wavelengths is determined entirely by the *shield outer radius* and is independent of the *coil radius* r_c. An experimental test of this prediction is

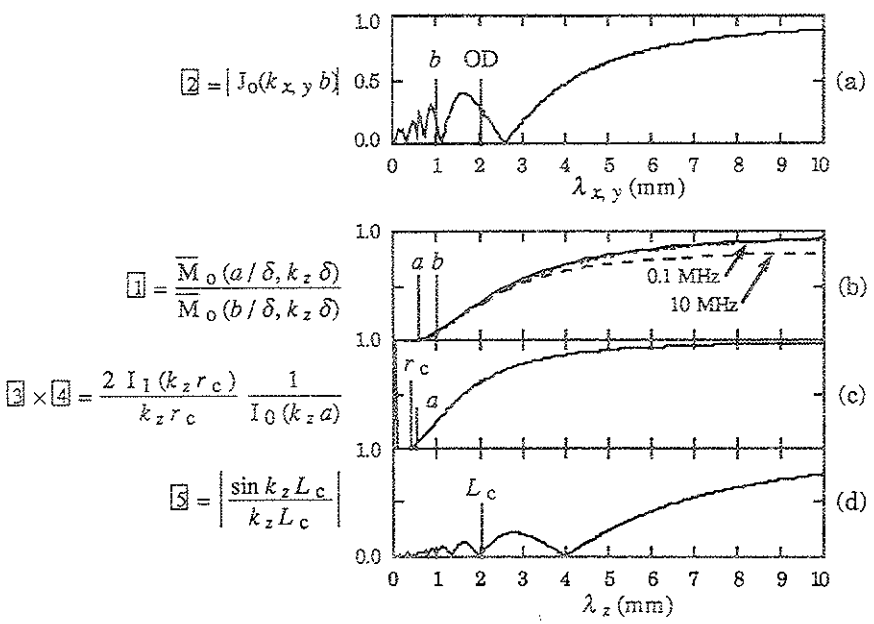

Figure 2.8. Portions of the total response to (a) transverse wavelengths $\lambda_{x,y}$ and (b-d) axial wavelengths λ_z for the 2mm OD graphite mini-probe (long-coil version, Table 2.2). r_c=0.36mm , a=0.55mm , b=1mm and L_c=2mm .

described at the end of this section.

The Bessel function factor [2] imposes upon the overall probe response a wavelength-dependent 'modulation' which produces zeros and maxima in the probe response as a function of the transverse wavelengths λ_y and λ_x. These factors are important only for short, probe-diameter-size wavelengths and approach unity for larger wavelengths. The transverse wavelength response, plotted in Figure 2.8(a) for a 2 mm mini-probe, falls to 1/2 of its maximum value at $\lambda_{x,y}/b = 4$. For $\lambda_{x,y}/b < 4$ the response oscillates between zero and successively smaller local maxima. Using the 1/2-amplitude

criterion as the definition of the approximate limit of resolution, the smallest resolvable transverse wavelength is

$$\lambda_{x,y}^{\max} / b \approx 4.0, \quad \text{or} \quad \lambda_{x,y}^{\max} \approx 2 \times \text{shield diameter}. \tag{2.9}$$

The dependence on the axial wavelength λ_z enters in four of the five factors in the probe response. The effect of finite $k_z \delta$ on the shield attenuation factor, 1, and the phase shift was mentioned above. The axial wavelength response of the probe is set primarily by three probe parameters: the coil length L_c, the coil radius r_c and the shield inner radius a. The $\mathrm{sinc}(k_z L_c)$ function, factor 5, resulted from integrating the preserved z dependence over the length of the coil and describes how the length of the coil affects the sensitivity of the probe to axial wavelengths. This dependence, plotted in Figure 2.8(d), is independent of shield characteristics and is the same dependence one would obtain from an unshielded coil. The other dependencies on *plasma axial* wavelength λ_z occur in connection with the *probe transverse* scale lengths a, r_c, and δ. The $k_z r_c$ factor, 3, and $k_z a$ factor, 4, come from the integration over r in the flux computation and are tied to the radial behavior of the field solutions. The coil radius r_c enters only in the third factor and is scaled to the axial wavelength λ_z. This observation coupled with the fact that transverse wavelength dependence is set entirely by the parameter $k_y b$ implies that the coil radius r_c affects not the *transverse* resolution but the *axial* resolution of the probe. Similarly, the $k_z a$ factor, 4, which came from matching solutions at the inner surface $r = a$, depends on

the axial wavelength λ_z and the inner radius a.

The recurrent and perhaps unexpected mixing of the plasma axial scale length λ_z with the probe transverse scales can be traced to the form of the prescribed external field, Eq. (2.1). In the absence of an axial variation ($k_z = 0$), an external field $\mathbf{B} = \hat{\mathbf{z}} B_z(r,\theta,t)$ satisfies $\nabla \cdot \mathbf{B} = 0$. The field is periodically compressed in the x and y directions, but the field lines remain parallel to each other and to the z axis. In this case there is no mixing. If, on the other hand, an axial variation is permitted in addition to variations in one or both transverse directions ($k_x, k_y, k_z \neq 0$) the field $\mathbf{B} = \hat{\mathbf{z}} B_z(r,\theta,z,t)$ does *not* satisfy $\nabla \cdot \mathbf{B} = 0$. To maintain a divergence-free field, a nonzero radial component $B_r(r,z,t)$ must be added to the external field. This radial component alters the spatial properties of B_z. The field lines suffer periodic bending in addition to the compression. (Where $|B_z|$ is large, $B_r = 0$ and $\mathbf{B} \parallel \hat{\mathbf{z}}$. Where B_z is zero, $|B_r|$ is maximum and $\mathbf{B} \perp \hat{\mathbf{z}}$.) The scale of variation of both B_z and B_r in the *axial* direction is λ_z (by hypothesis). The scale of variation of B_z (and B_r) in the *radial* direction is also λ_z (by analogy with antenna theory). Roughly speaking, this is the mechanism by which the *axial* wavelength λ_z couples to the *transverse* probe scales.

The response of the probe to axial wavelengths is determined by four factors with complicated dependencies on all five probe scales. For this reason one cannot write down a useful general expression for the approximate minimum resolvable axial wavelength. However, if the 1/2-amplitude criterion is used to define $\lambda_z^{\min}$ for each of the λ_z-dependent parts of the total response, we have

$$\begin{aligned} &\text{factor } \boxed{3} \quad \lambda_z^{\min}/r_c \approx 2.5, \\ &\text{factor } \boxed{4} \quad \lambda_z^{\min}/a \approx 3.5, \\ &\text{factor } \boxed{5} \quad \lambda_z^{\min}/L_c \approx 3.3. \end{aligned} \tag{2.10}$$

Because these ratios are similar in value, if one of the probe scale lengths is much greater than the others, it will determine the upper limit on the minimum resolvable axial wavelengths. For the long-coil-length mini-probe and the micro-probe used in this thesis (Table 2.2), the largest probe scale was the coil length ($L_c >> a > r_c$). The short-coil-length mini-probe had comparable probe scale lengths ($L_c \geq a \geq r_c$). And for the standard 1/4 inch probe the largest scale length was the inner shield radius ($a > r_c >> L_c$). The 1/2-amplitude cutoff of the shield attenuation factor $\boxed{1}$ is too complex to be summarized by a single simple expression and its contribution should be considered on a case-by-case basis. A simple test of the predicted axial wavelength response of the probe is mentioned at the end of this section.

At high frequencies, short transverse wavelengths, but long axial wavelengths, the k_z-dependent factors $\boxed{3} \times \boxed{4}$ and $\boxed{5}$ in the probe response approach unity. In addition, the shield attenuation ratio, factor $\boxed{1}$, approaches the limit indicated by Eq. (2.8). In this limit the probe response simplifies to

$$\frac{\left|\varepsilon^{\max}\right|}{\omega N B_0 A_c} = \frac{M_0(a/\delta)}{M_0(b/\delta)} \left|J_0(k_y b)\right| \left|J_0(k_x b)\right|, \tag{2.11}$$

where $M_0(x) = \overline{M}_0(x,0) = J_0\left(i^{3/2}x\right)$. The phase shift Eq. (2.7) simplifies in a similar way. As in the general case, the probe response is bounded by 0 and

1. The response is symmetric in λ_x and λ_y and is characterized entirely by the shield outer radius b as plotted in Figure 2.8(a) and summarized by Eq. (2.9).

The standard application of a $\dot{B}$ probe is in the limit of low frequencies ($\delta >> a, b$) and long wavelengths ($\lambda_{x,y} >> b$, $\lambda_z >> a, r_c, L_c, \delta$). In this limit the skin effects and spatial averaging are negligible, and the probe response factors $\boxed{1}, \boxed{2}, \boxed{3} \times \boxed{4}$, and $\boxed{5}$ approach unity (Figure 2.8). In fact, the expression $\left|\varepsilon^{\max}\right| / \omega N B_0 A_c = 1$ is the basis for the low-frequency method of calibration with effective area $A_{\text{eff}} = NA_c$.

Tests of the Predicted Poloidal and Axial Wavelength Response

The effect of coil radius and shield radius was studied using three probes: a standard 6.35 mm shield with a ~3 mm diameter coil (labeled BB for big coil in a big shield), a 2 mm shield with a ~1 mm diameter coil (labeled SS for small coil in a small shield), and a 6.35 mm shield with a ~1 mm diameter coil (labeled SB for small coil in a big shield). The length of the coil in the SS probe and the inner radii of the SB and BB probes were similar, and each was the dominant scale length for determining the overall axial (plasma-radial) wavelength response of their respective probes. Thus, these three probes respond differently to poloidal wavelengths but respond in a similar way to radial wavelengths. (Low-frequency measurements and most tokamak turbulence models indicate that toroidal wavelengths are much longer than poloidal wavelengths, $\lambda_x >> \lambda_y$. Under this assumption the response to the toroidal wavelengths lies in the long-wavelength regime

and is identical for each probe used here. The experimental approach is described in greater detail in Section 4.1.) Figure 2.9 shows the averaged power spectra measured by each probe at x=6 cm in $q_a \approx 1$ discharges. The gap between the low-frequency and high-frequency spectra was caused by an early version of the amplifier/digitizer systems. The high-frequency spectrum measured by the SS probe shows a strong enhancement of power compared to that of the BB probe (a factor of ~10). However, the power measured by the SB probe is nearly identical (within a factor of ~2 total uncertainty) to

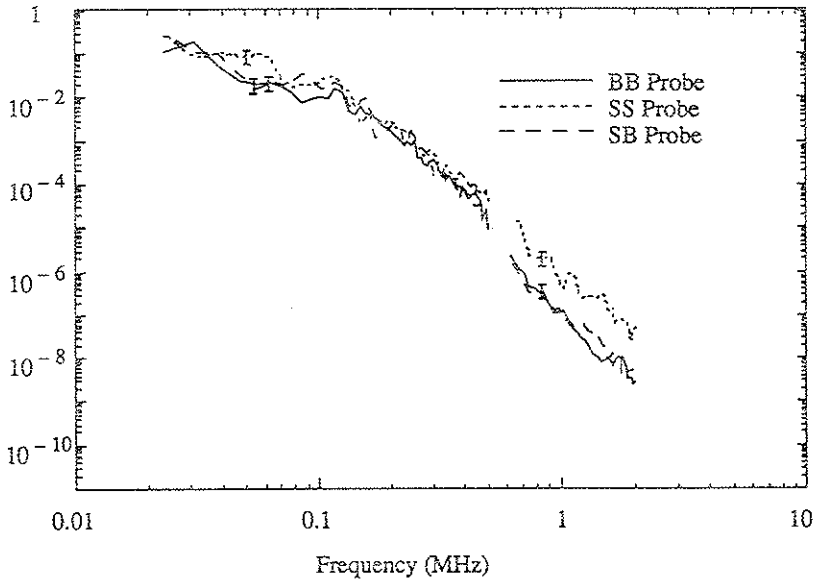

Figure 2.9. Power spectra measured by the BB, SB and SS probes ($q_a \approx 1$, x=6 cm). The error bars represent statistical scatter in the data. The SS probe measured significantly more power at higher frequencies than the SB and BB probes, which measured similar spectra. The ability to resolve short probe-transverse wavelengths depends on *shield* radius rather than *coil* radius.

the power measured by the BB probe. This implies that it is the *shield* radius, not the *coil* radius, which determines the sensitivity of the probes to poloidal wavelengths. This result is consistent with the results derived above.

A power comparison test of the response of the probes to short axial wavelengths (described in detail at the end of Section 4.2) shows that probes with short coils resolve more power than probes with longer coils. This result is also consistent with the results of the calculation performed above.

2.4.3 Amplifier and Filter Systems

The frequencies of interest span nearly 3 decades from drift frequencies corresponding to large-scale modes (~10 kHz for m=1 in Tokapole II) to drift frequencies at c/ω_{pe} scales (~5 MHz). The total dynamic range of the raw (unamplified) $\dot{B}$ signals over this frequency range can span 5 to 6 orders of magnitude, ranging from ~1 V at the lowest frequencies in low-q_a discharges to ~1 μV and below at the highest frequencies in the high-q_a discharges. Thus, the dynamic range required to amplify and store these signals is beyond the capability of any single amplifier and digitizer combination. To circumvent this problem the frequency range of interest was divided into two experimental bands each with its own set of amplifiers and filters.

The data presented in this thesis and the electronics used to acquire the data are classified as either *low frequency* (10 kHz – 750 kHz) or *high frequency* (0.5 MHz – 7 MHz). The high-frequency amplifiers and filters are modifications of the system designed and built by D. Kortbawi[13] and T. Lovell. Low-frequency amplifiers (stock AM502s) were added by M.

LaPointe[14] to acquire magnetic fluctuation data over a wide range of low and high frequencies simultaneously. This versatile system was modified further to obtain the low- and high-frequency $\tilde{B}_r$ data presented in this thesis. The signals from each $\dot{B}$ probe were input simultaneously to the low-frequency and high-frequency amplifier/filter/digitizer systems. A typical setup of the electronics is shown schematically in Figure 2.10. The system was also used by I. Tan[15] to measure electrostatic fluctuations at low and high frequencies in Tokapole II.

In the low-frequency range Tektronix AM502 variable-gain differential amplifiers were used to amplify and partially filter the $\dot{B}$ probe signals. The AM502 has a simple RC filter with a variable corner (3 dB point) at the input and output. The high-pass filter at the input was set to attenuate the low-frequency (<10 kHz) magnetic fluctuation signal associated with large-scale MHD activity. [Anyone wishing to use the AM502 in a similar way should consider modifying the high-pass filter (internally or by adding an external filter module at the input to the amplifier) to obtain a steeper rolloff than that provided internally by the simple, low-performance, single-pole RC filter. This would effectively increase the dynamic range of the low-frequency system.] Two low-pass filters, the internal AM502 RC filter and an external filter module, were used as anti-aliasing filters. The corner of the AM502 low-pass was set at 1 MHz, the highest setting possible. Because the roll off of the AM502 single-pole RC filter is slow (20 dB/decade, the slowest possible for passive networks), there is significant signal amplitude at frequencies up to several MHz. The second low-pass filter, placed at the

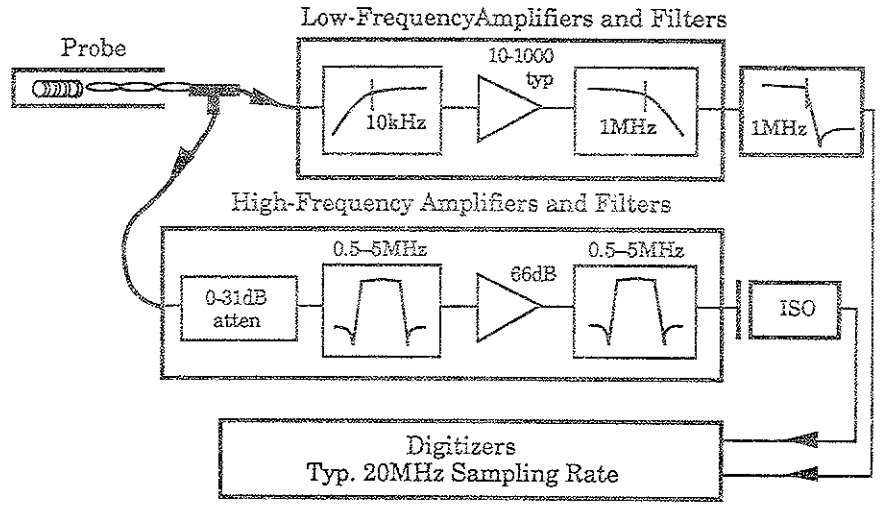

Figure 2.10. Typical system configuration of amplifiers, filters and digitizers used to acquire low and high frequency magnetic fluctuation data simultaneously.

output to the AM502, was designed to be used when the digitizer sampling rate was as low as 5 MHz, thus requiring that signal amplitudes be attenuated into the range of the digitizer bit noise at the Nyquist frequency of 2.5 MHz. An n=5 elliptic function filter design[16] was chosen for this filter because of its combination of fast roll off, large stop-band attenuation and relatively simple design and construction. The response of this filter has a corner at 1MHz and a stop-band attenuation of ~ 45 dB above 2 MHz. The average roll off is ~45 dB/octave, ~150 dB/decade, or ~7 times faster than the single-pole RC filter. The design of all filter modules was tested and evaluated before construction by simulating its response in I-G SPICE[17], an interactive

circuit simulation software package.

The high-frequency amplifier and filter system has a fixed gain of ~66 dB (~2000) with a variable 0–31 dB attenuator at the input to adjust the overall gain and dynamic range of the system. The high frequency system also contains two removable band-pass filter modules. For the results presented in this thesis the filter modules used were n=3 Cauer-Elliptic band pass filters [13]. They were chosen because of their sharp corners, relatively simple design and ease of construction and tuning. The ground for the low-frequency and high-frequency electronics was taken from the CAMAC racks through the long (~8 m) cables connecting the output of the amplifier system to the digitizers. To avoid ground loop problems, the high-frequency signals were passed through low-inductance isolation transformers. RG55 coaxial cable was used to carry both the low-frequency signals and the ground reference for all the electronics to the digitizers. The RG55 cable is equivalent to the more common RG58 cable with one important exception: RG55 has a double braid shield whereas the RG58 has only a single braid shield. Maintaining a good, low-impedance path to ground for the high-gain, high-frequency electronics was essential to minimizing noise problems in the high-frequency range. The electrostatic shields of the $\dot{B}$ probes were grounded directly to the vacuum vessel. Both the low-frequency and high-frequency $\dot{B}$ probe data were recorded on DSP model 2001A digitizers with 32 kilobytes of memory. These digitizers can sample at rates up to 100 MHz but were typically run at 5, 10, 20 or 50 MHz. The dynamic range of a 2001A is ±256 mV with 8 bit (2 mV/bit) resolution. The high-frequency

amplifiers had a noise level of ~10 mV. These amplifiers were designed to be used with 10 mV/bit LeCroy 8210 digitizers for which the 10 mV noise levels represented ~1bit. With the DSP2001A, however, the noise level represented nearly 5 bits. The combination of relatively small digitizer dynamic range and large amplifier noise level made difficult the task of adjusting gains and attenuations to maximize the signal-to-noise ratio while keeping a significant portion of the fluctuating signal out of saturation. Unless noted otherwise, all data presented in Chapter 4 were recorded at a sampling rate of 20 MHz.

2.4.4 Calibration of the Magnetic Probes

At high frequencies and short wavelengths, the probe response is very complicated. Because the calibration for the effects of short wavelengths could not be performed, the results of Section 2.4.2 are used to help interpret the fluctuation measurements made with the small probes at high frequencies. This is described in more detail in Section 4.1. The calibration for the frequency-dependent effects is straightforward to perform and apply. It is described in remainder of this section.

Because the power comparison measurements described in this thesis required accurate measurements of fluctuation power levels across two different amplifier systems and two to three decades of frequency, a careful and detailed amplitude calibration of each $\dot{B}$ probe was performed. Each probe, low-frequency or high-frequency amplifier and filter system, and all cables were calibrated 'end-to-end' as a single system. Each calibration was

performed in a physical and electrical configuration that most closely matched the hardware setup actually used to take data. (Helmholtz coil and generator replaced the vacuum vessel, oscilloscope replaced digitizer, and so on.) This was especially important for the high-gain, high-frequency system in which proper termination, correct and adequate grounding, and careful isolation were absolutely essential for obtaining consistent and accurate calibration data. A sure sign of a calibration problem is a mismatch at adjacent ends of the calibrated low-frequency and high-frequency spectra of the same $\dot{B}$ signal.

The calibrations were performed using the 12″ diameter, 0.56 G/A (nominal), low-frequency Helmholtz coil set and the 8″ diameter, 0.091 G/A (nominal) high-frequency "Constant Current Calibrator" (CCC) constructed by D. Kortbawi. The CCC was built for the driven Alfvén wave research on Tokapole II and was designed to operate in constant-current mode over several narrow bands of frequencies. Because the CCC could not maintain a sufficiently constant current over the broad range of frequencies of interest in this thesis, the CCC was operated in its "Out-of-Control" mode which bypassed the feedback circuitry that attempts to hold the drive current constant. At low frequencies (<500 kHz) the Tektronix or Wavetek function generators are adequate for driving the Helmholtz coils. Above about 0.5 MHz the Hewlett-Packard 606A tube-based oscillator is far superior to its solid state successors. The HP606A provides large output voltages for large drive currents and large probe signals, rock-solid frequency stability (better that 1 part in 10^5 to 10^6 over one hour when warmed up) and very low

harmonic content. The low harmonic content is critical for accurately tuning the elliptic-function filters used in the high-frequency system.

Anyone who wishes to use a Helmholtz coil set for making accurate amplitude and phase calibration measurements should *not* use the Helmholtz coil at frequencies above or within a decade of its self-resonant frequency unless careful and independent measurements are made of its gauss-per-amp (G/A) characteristic (*i.e.* the field generated per Ampere of drive current). For the low- and high-frequency coils the lowest resonant frequencies lie near 1 MHz and 10 MHz, respectively. The location of the resonance can and typically does vary with grounding schemes and should always be verified before calibrating. This consideration is particularly important for the high-frequency Helmholtz set which is intended to be used at frequencies that are within one decade of the self resonance. In addition, for making accurate amplitude and phase calibration measurements, especially at high frequencies, one should measure the drive current directly rather than calculating it from measurements of the voltage across a current-limiting resistor. Use a high-quality current transformer (which is essentially a Rogowski operated in the self-integration regime[18]) to measure the drive current to the coil. An excellent choice is the Pearson Model 110 Current Monitor. It is a nearly ideal passive device that gives a voltage proportional to I, rather than dI/dt, that is accurate to within 1% in amplitude and phase from 20 Hz to 20 MHz. However, a precise measurement of the drive current flowing *to* the coil does not ensure an accurate measurement of the G/A characteristic. At frequencies as low as one-tenth

of the first self resonance, the portion of the drive current that produces axial magnetic field in the Helmholtz coil begins to decrease. The net result is a reduction in the axial magnetic field generated by a known *drive* current and a smaller-than-expected G/A characteristic at the higher frequencies. Figure 2.11 shows the frequency-dependent correction factor to the nominal G/A characteristic of the high-frequency Helmholtz coil over its intended operating range of operation. The nominal 0.091 G/A rating was measured at 2.0 MHz by D. Kortbawi. The actual value varies by as much as 30% above and below 2 MHz. The values on the curves in Figure 2.11 are normalized to the nominal 2.0 MHz value. The values below about 500 kHz have a larger relative error due to low signal-to-noise ratio. There may be a systematic error of ~4% because the values at 2.0 MHz measured by D. Kortbawi and myself disagree by ~4%. The characteristic was measured with a large (~3/4 ") coil of carefully measured area and with no electrostatic shielding to distort the field being measured. To avoid the inevitable frequency-dependent gain of a high-frequency amplifier, the signal from the large coil was fed directly into an oscilloscope. The correction factor was applied to the high-frequency calibration curves and power spectra presented in Chapter 4.

At frequencies below ~100 kHz (one-tenth of the first self resonance of the low-frequency Helmholtz coil, and far below the frequencies at which attenuation and phase shift due to the probe electrostatic shielding are important), the standard "effective area" calibration is adequate. In this method a single, frequency independent number, the effective area A_{eff} of the probe, is used to characterize the probe. The effects of electrostatic

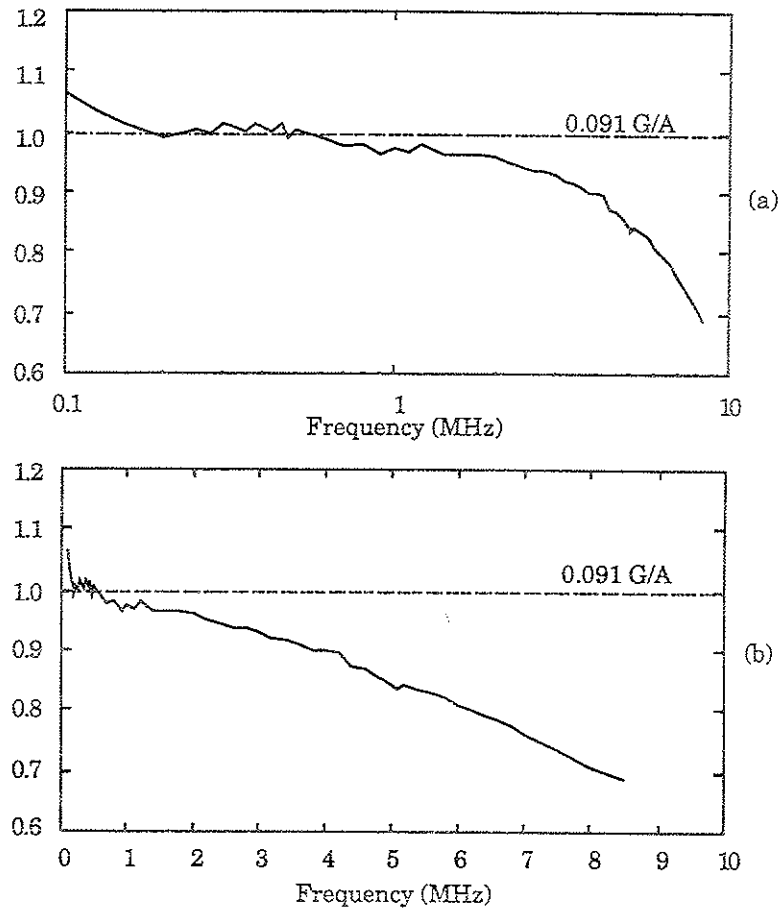

Figure 2.11 The gauss per amp characteristic of the high-frequency "Constant Current Calibrator" norm alized to the nominal value 0.091 G/A.

shielding, cables, and the variation of amplifier gain with frequency are ignored without consequence. The A_{eff} is obtained from Faraday's law $\varepsilon = \omega NBA_{eff}$ as the slope of the plot of the probe emf ε against ωB, where B is

assumed to be constant. Typically A_{eff} agrees well with the area of the coil form times the number of turns on the form.

At frequencies above ~100 kHz, the situation is quite different. Numerous frequency-dependent quantities enter into the calibration. Skin effects associated with the conducting electrostatic shield, variability of amplifier gain, distortions due to long coax cables, isolation transformers, and attenuators are a few of the more important frequency-dependent effects that contribute to the calibration. All these effects are taken into account in an end-to-end calibration of the entire system in a configuration similar to that used to acquire the data. The values of probe-system output voltage amplitude (and phase if desired) for a given Helmholtz drive current are recorded over many frequencies in the range of interest. The voltage and current measurements are used with the G/A characteristic information to generate a calibration table of the probe-system sensitivities (in Gauss per Volt) for each frequency. The ensemble-averaged power spectra are corrected in frequency space by multiplication with the square of a spline fit of the G/V calibration vector.

References

[1] A. P. Biddle, R. N. Dexter, R. J. Groebner, D. T. Holly, B. Lipschultz, M. W. Phillips, S. C. Prager and J. C. Sprott, Nucl. Fusion 9, 1509 (1979).

[2] J. C. Sprott and T. W. Lovell, University of Wisconsin–Madison Plasma Physics Group Report PLP #744 (1978).

[3] J. C. Sprott, University of Wisconsin–Madison Plasma Physics Group Report PLP #750 (1978).

[4] R. J. Groebner, Ph.D. Thesis, University of Wisconsin–Madison, (1979).

[5] J. F. O'Hanlon, *A User's Guide to Vacuum Technology*, 2nd ed., (Wiley, New York, 1989).

[6] T. H. Osborn, Ph.D. Thesis, University of Wisconsin–Madison, (1984);
N. S. Brickhouse, *et al.*, in *Proceedings of the Tenth International Conference on Plasma Physics and Controlled Nuclear Fusion Research*, London, 1984, (IAEA, Vienna, 1985) 385;
E. Uchimoto, Ph.D. Thesis, University of Wisconsin–Madison, (1988).

[7] R. A. Moyer, Ph.D. Thesis, University of Wisconsin–Madison, (1988).

[8] J. C. Sprott, University of Wisconsin–Madison Plasma Physics Group Report PLP #889 (1983);
J. S. Sarff, University of Wisconsin–Madison Plasma Physics Group Report PLP #1003 (1987).

[9] H. R. Garner, University of Wisconsin–Madison Plasma Physics Group Report PLP #833 (1980).

[10] J. Goetz, Ph.D. Thesis, University of Wisconsin–Madison, (1990).

[11] E. J. Haines, University of Wisconsin–Madison Plasma Physics Group Report PLP #1073 (1991).

[12] L. J. Briggs and A. N. Lowan, *Table of the Bessel Functions* $J_0(z)$ *and* $J_1(z)$ *for Complex Arguments*, (Columbia University Press, 1943).

[13] D. Kortbawi, Ph.D. Thesis, University of Wisconsin–Madison, (1988).

[14] M. A. LaPointe, Ph.D. Thesis, University of Wisconsin–Madison, (1990).

[15] I. H. Tan, Ph.D. Thesis, University of Wisconsin–Madison, in progress.

[16] A. B. Williams, *Electronic Filter Design Handbook*, (Mc-Graw–Hill, New York, 1981);
A. I. Zverev, *Handbook of Filter Synthesis*, (Wiley, New York, 1967).

[17] A. B. Associates, Inc., computer code I-G SPICE version IV, (Tampa, FL, 1986).

[18] M. B. Stout, *Basic Electrical Measurements*, 2nd ed., (Prentice-Hall, Englewood Cliffs, NJ, 1960), chapter 15.

CHAPTER 3

Review of Theories Of Small-Scale Magnetic Fluctuations

3.1 Introduction

In this chapter I will give a brief overview of the various models of microturbulence as they relate to the small-scale magnetic fluctuation measurements presented in Chapter 4. Particular emphasis will be placed on the theories of electron temperature gradient driven turbulence, or η_e-mode theories. This chapter is not intended to be a review of microturbulence theories nor is it intended to be a survey of the theories of anomalous transport in plasmas. Rather, the goal is to provide a theoretical basis on which to characterize and understand the experimental results.

Small-scale-length magnetic fluctuations have been proposed as a possible explanation of anomalous electron thermal transport in tokamak plasmas. Ohkawa[1] heuristically derived an electron energy diffusion coefficient ($\chi_e \sim (c/\omega_{pe})^2 \nu_e / qR$) in which the collisionless skin depth c/ω_{pe}, which is typically smaller than the ion gyroradius, appears as the step size in a random-walk diffusion process. The Ohkawa formula has subsequently been derived from more detailed theories[2][3] and appears to be consistent with the confinement results obtained in several ohmically heated tokamaks. Linear theories[12][13] of electron-temperature-gradient-driven, or η_e, modes have predicted fluctuations at short spatial scales but have not identified c/ω_{pe} as a characteristic spatial scale. These modes have characteristic scale lengths of the order of the much smaller electron gyroradius and are

primarily electrostatic. The nonlinear η_e simulations performed by Horton, et al.[15][19][20] predict the existence of magnetic fluctuations at spatial scales near c/ω_{pe}. However, the theory is the only nonlinear study performed on the η_e modes and is difficult to assess because it is primarily computational and has limited resolution at the c/ω_{pe} scales. Nonetheless, there is sufficient motivation for an experimental study of short-wavelength magnetic turbulence.

3.2 Summary of Magnetic Microturbulence Theories

The measurements of the radial magnetic fluctuation spectra in Tokapole II (presented in Chapter 4) show the presence of increased magnetic fluctuation power (1) at short poloidal and radial wavelengths near the collisionless skin depth c/ω_{pe}, and (2) at high frequencies near and below the electron diamagnetic drift frequency, $\omega^*_{ne} = k_y v_e^2/L_n \omega_{ce}$, where k_y is the poloidal wavenumber, v_e is the electron thermal speed, L_n is the density gradient scale length, and ω_{ce} is the electron cyclotron frequency. In Tokapole II the drift frequency evaluated for such short scale lengths ($\lambda_y \sim c/\omega_{pe} \lesssim \rho_i \sim 2$ mm) is $\omega^*_{ne}/2\pi \sim 3$ MHz. This is large compared to the drift frequencies associated with low poloidal mode numbers but is somewhat smaller than the ion cyclotron frequency. The enhanced small-scale magnetic fluctuations are likely due to one or more microinstabilities present in the plasma or a turbulent cascade from another frequency and wavenumber range. The goal of this thesis is to present what has been learned about these enhanced fluctuations and its possible causes and to compare the results of systematic experiments with relevant theories.

The Importance of Magnetic Microturbulence

The body of literature devoted to the experimental and theoretical studies of plasma microturbulence in general is quite large. Liewer[4], for example, has compiled a comprehensive review of the subject prior to 1985. More specifically, the theories of drift wave turbulence and transport were reviewed by Tang[5] and Horton[6].

For the purpose of comparing to the experimental results presented in this thesis, however, the majority of the numerous microturbulence theories proposed to date are inadequate because they treat only the electrostatic ($\tilde{B} = 0$) component of the turbulence or they treat the turbulence in the low frequency limit $\omega << \omega_{ci}$. In Tokapole II the frequencies of interest lie well within a decade of ω_{ci}. Electrostatic drift wave turbulence is often thought to play a key role in anomalous transport. However, numerous theoretical studies indicate that magnetic fluctuation are also important, especially at finite β. Callen[7] showed that the small radial magnetic component of drift modes can produce stochastic magnetic island structures and increase radial electron thermal transport in tokamaks. In a discussion of low-frequency electromagnetic fluctuations and related anomalous transport, Horton[6] argued that the electromagnetic component of drift modes can dominate the $\mathbf{E} \times \mathbf{B}$ transport for increased values of β ($\beta >> m_e/m_i$). The view that magnetic fluctuations dominate transport as β rises above m_e/m_i is supported by several other works. Waltz[8] studied numerically a self-

consistent nonlinear fluid model of low frequency electromagnetic fluctuations. He found that the magnetic fluctuation and density fluctuation levels are related by $\left(\tilde{B}_r / B\right)_{\rm rms} \equiv (\beta/2)\, q \left(\tilde{n}/n\right)_{\rm rms}$, and that, for some parameters, even a modest β of ~1% ~ 20 m_e / m_i caused the thermal diffusivity due to $\tilde{B}$ to exceed the particle diffusivity due to $\tilde{E}$. This simple relation is shown to agree with a mixing- length estimate of the magnetic fluctuation level and with probe measurements performed in the MACROTOR tokamak[4].

Rewoldt, Tang and Hastie[9] have developed a numerical model for simulating low-frequency kinetic electromagnetic modes in tokamaks. The model is based on a set of coupled integro-differential equations, and the numerical solution of these equations provides eigenfrequencies, eigenfunctions and quasilinear transport coefficients. They compare particle and energy transport coefficients for the full toroidal drift mode and in the electrostatic limit as a function of β. For $\beta \sim m_e / m_i$ the transport coefficients are almost identical. However, as β increases the electromagnetic and electrostatic coefficients increase and diverge. For $\beta \sim 1.5\% \sim 30\, m_e / m_i$, the electromagnetic coefficients are about 4 times larger than the electrostatic coefficients.

Magnetic Turbulence at c/ω_{pe} Scales

In a large number of tokamaks the electron confinement time increases linearly with plasma density (Alcator-type scaling). Ohkawa[1] first proposed that the linear density dependence of the empirical scaling laws could be

accounted for by short c/ω_{pe}-scale magnetic fluctuations. Such fluctuations are presumed to cause a random walk of electrons across equilibrium magnetic surfaces with characteristic step size $\Delta x \sim c/\omega_{pe} \sim n^{-1/2}$ and confinement times $\tau_E \propto \Delta x^{-2} \propto n$.

Recently, theories of ion[10] and electron[11][12][13] temperature gradient driven turbulence (η_e and η_i turbulence) have been proposed to explain anomalous ion and electron thermal transport in plasmas. The electron- and ion-temperature-gradient parameters, η_e and η_i, are defined by

$$\eta_\alpha \equiv \frac{{\rm d} \ln T_\alpha / {\rm d}r}{{\rm d} \ln n_\alpha / {\rm d}r} = L_n / L_T. \tag{3.1}$$

These theories predict magnetic and electrostatic fluctuation activity at small spatial scales of the order of the ρ_i, c/ω_{pe} or below and at frequencies up to the drift frequency ω^*_{ne}. Compared to most other microturbulence models (which are primarily low-frequency or electrostatic) the η_e and η_i theories predict characteristic spatial scales and frequencies of the turbulence that are in better agreement with the experimental results presented in Chapter 4. The η_i-mode turbulence, however, is characterized by average poloidal wavenumbers in the range[10][14] $\langle k_y \rho_s \rangle \lesssim 1$, where $\rho_s = \tau^{1/2} \rho_i$ and $\tau \equiv T_e / T_i$. (We identify the x, y and z coordinates with the radial, poloidal and toroidal directions in a tokamak.) In Tokapole II ($\tau \sim 2$) the average wavelengths are at least an order of magnitude larger than both ρ_i and the spatial scales of the observed enhancement of magnetic fluctuations. In contrast, the spatial scales of the magnetic turbulence associated with η_e modes is predicted to

be in the range[15] $(k_y c/\omega_{pe}) \sim (k_x c/\omega_{pe}) \sim 0.5$ to 1. This implies characteristic wavelengths that are much closer to the spatial scales in which the enhanced magnetic fluctuations are observed.

The rest of this chapter will summarize the features of η_e turbulence theory which are relevant to making comparisons with the experimental results. In section 3.3 I will review the linear η_e models, and in section 3.4 a nonlinear η_e model will be discussed. The experimental results will be compared against the η_e theories in Chapter 4 and the limitations of both will be discussed.

3.3 Linear η_e-Mode Models

3.3.1 Sheared-Slab Model

Lee, Dong, Guzdar and Liu[12] have studied the linear instability of collisionless, short-λ ($\rho_e < \lambda_\perp < \rho_i$) drift modes driven by electron temperature gradients in a sheared-slab field geometry. The authors treat the electrostatic instability using local and nonlocal Vlasov theory to obtain simple dispersion relations and an estimate for the mode width. The radial localization of the mode is predicted to be quite narrow: $\Delta x \approx \rho_e \sqrt{1 + \eta_e}$.

Lee, *et al.* treat the full electromagnetic character of the mode by deriving and numerically solving a pair of coupled integral equations for the perturbed scalar and parallel vector potentials $\tilde{\phi}$ and $\tilde{A}_\parallel$. It is the fluctuating parallel vector potential that produces the radial magnetic fluctuations important in cross-field transport. [In theories that examine the electromagnetic component of microturbulence, $\tilde{A}_\parallel$ and $\tilde{B}_x = k_y \tilde{A}_\parallel$ figure more prominently

than $\tilde{A}_\perp$ and $\tilde{B}_\parallel$. This is true because the ordering $k_\parallel << k_\perp$ implies (1) that $\omega^*_{ne}/k_\perp << \omega^*_{ne}/k_\parallel < v_A$ for low β (v_A is the Alfvén speed) and thus, (2) that drift-shear coupling ($\omega^*_{ne}/k \sim v_A$ with $\tilde{B} = B_\perp$ and $k = k_\parallel$) occurs more readily and is therefore more important than drift-compressional coupling ($\omega^*_{ne}/k \sim v_A$ with $\tilde{B} = B_\parallel$ and $k = k_\perp$).] The electromagnetic model, an extension of earlier work[16] to finite β ($m_e/m_i << \beta << 1$), includes gyrokinetic effects and is valid to relatively high frequencies, $\omega < \omega_{ce,i}$. From the linearized Vlasov equation, the authors write the perturbed distribution function for the electrons and ions and use these functions in Poisson and Ampere's equations to obtain their model equations for $\tilde{\phi}$ and $\tilde{A}_\parallel$. In the electrostatic limit corresponding to $\beta_e << m_e/m_i$, $\tilde{\phi}$ and $\tilde{A}_\parallel$ are decoupled.

The coupled equations are solved numerically for $\tilde{\phi}$ and $\tilde{A}_\parallel$ for the lowest few modes (*i.e.*, those with the fewest radial nodes). The authors plot the normalized growth rate γ against η_e for the three lowest modes (Figure 3.1 below). The lowest mode is most unstable and has a threshold at $\eta_e \sim 1$. In Tokapole II electrostatic probe measurements[17] of n_e and T_e profiles in the edge region indicate that $\eta_e \sim 1$ - 2.

The eigenfunctions are plotted in both x- and k_x-space for a given k_y. Figure 3.2(a) shows that in the lowest mode (for $k_y \rho_e = 0.5$) $\tilde{\phi}(x)$ is peaked on a resonant surface and is localized to within about one electron gyroradius, consistent with the nonlocal analytical result. The $\tilde{A}_\parallel$ (Figure 3.2(b)) peaks slightly outside the resonant surface and has a larger localization width of about 5 ρ_e. At larger λ_y the modes are less unstable and the eigenfunctions become more tightly localized.

The real and imaginary parts of the mode frequency, ω_r and γ, for the lowest, most unstable mode are shown in Figure 3.3 as a function of k_y for two values of η_e. The normalization of the frequencies is perhaps more meaningful in the form $k_\perp \rho_e / \omega^*_{ne} = L_n / v_e$. The time scale is the time of flight across the density scale length L_n at the electron thermal speed v_e. This time scale is very fast and implies high real frequenies and very rapid linear growth ($\gamma \sim \omega$). This stands in contrast to ordinary, longer-wavelength drift modes which exhibit slower linear growth ($\gamma < \omega$). For Tokapole II parameters[18] ($T_e \approx 100$ eV and $L_n \approx 3$ - 5 cm) this time scale is roughly 0.06 μs corresponding to $\omega \sim 10^8$ rad/s or $f \sim 16$ MHz. The maximum growth rate of the mode (Figure 3.3(b)), however, is one to two orders of magnitude smaller than this frequency scale factor, putting typical growth rates in the 1 μs range. There are three observations to make from Figure 3.3 that are relevant to this thesis. First, the most unstable mode has larger growth rates and higher real frequencies at larger values of η_e. The same is generally true for the other higher order modes not shown here. Second, the mode is maximally unstable at spatial scales between ρ_e and ρ_i ($k_y \rho_e \sim 0.7$, or $\lambda_y \sim 10\, \rho_e \sim 0.5\, \rho_i$ based on $\rho_i / \rho_e \sim 20$ in Tokapole II with $\tau = 4$). In addition, the mode is unstable over a broad range of λ_y with significant growth at wavelengths from $\sim 5\, \rho_e$ up to $\sim 20\, \rho_e \sim \rho_i$. Third, the mode is unstable over a wide range of frequencies below $\sim 0.3\, \omega^*_{ne}$ and exhibits significant growth at frequencies as low as one to two decades below. For Tokapole II parameters in both low-q_a ($B_T \sim 3$ kG, $L_n \sim 5$ cm) and high-q_a ($B_T \sim 5$ kG, $L_n \sim 3$ cm) discharges, this translates to a range of frequencies of ~1 MHz down to ~10 kHz.

The finite-β_e, sheared-slab results plotted in Figures 3.2 and 3.3 were obtained for $\beta_e = 1\%$ (most comparable to Tokapole II low-q_a discharges with $\beta_e \approx 0.5\%$) and shear parameter $L = L_n / L_s = 0.1$ (also comparable to Tokapole II inside the separatrix if $L_n / L_s \sim a / R \approx 0.16$). Lee, *et al.* find that the growth rates are slightly larger in the electrostatic limit ($\beta_e << m_e / m_i$) than for the finite β_e cases, indicating that finite β_e and, hence, the coupling of $\tilde{\phi}$ and $\tilde{A}_\parallel$ tends to stabilize the modes. They also observe that increasing the magnetic shear past a certain threshold value also tends to stabilize the modes (Figure 3.4).

3.3.2 Toroidal Model

Horton and coworkers have studied the linear[13] and nonlinear[15] [19][20] instability of η_e modes in toroidal geometry. Their linear calculations will be discussed in this section and their nonlinear model will be reviewed in section 3.4.

Horton, Hong and Tang performed local hydrodynamic and local Vlasov kinetic calculations, both in the electrostatic regime, to obtain dispersion relations as well as information on the growth rates and real frequencies of the η_e modes. The hydrodynamic calculation is based on the electron fluid equations (continuity, force balance and energy conservation) and adiabatic ion dynamics ($\omega << k_\perp v_i$) in the presence of an electron temperature gradient. The authors assume short wavelengths ($\rho_e \leq \lambda < \rho_i$) and high frequencies ($\omega, \gamma >> k_\parallel v_e$) and include toroidal effects due to VB and curvature drifts.

The authors find that the stability threshold value is $\eta_e^{crit} \approx 2/3$. The maximum growth of the electrostatic mode occurs at $k_\perp \rho_{ei} \leq 1$ which corresponds to spatial scales slightly larger than a few ρ_e (if $\tau = 4$). At these scales the maximum growth rate is

$$\gamma_m \sim \frac{v_{ei}}{L_n}\sqrt{2\,\varepsilon_n} = \frac{v_e}{L_n}\sqrt{2\,\varepsilon_n/\tau}. \qquad (3.2)$$

For Tokapole II parameters, $\gamma_m \sim 0.3\ v_e/L_n$. The frequency scale factor used by Horton, *et al.* is essentially the same as in Lee, *et al.* differing only by the factor of $\tau^{1/2}$. This estimate of γ_m is about equal to the growth rates calculated by Lee, *et al.* (Figure 3.3(b)).

Plots of the normalized real frequency and growth rate against η_e for various $k_\perp \rho_{ei}$ are shown in Figure 3.5 and summarize the results of the linear Vlasov kinetic calculation performed by Horton, *et al.* The growth rates and real frequencies are quantitatively similar to those calculated by Lee, *et al.* Again, the growth rates are very fast and are comparable to the mode frequencies. For $\eta_e \geq 1$ there is less than one oscillation in each e-folding of the mode growth. Figures 3.5(a) and (b) also indicate the variation of the growth rate with k_y. At longer wavelengths the real frequencies decrease and the mode becomes more stable. The linear toroidal kinetic model reduces to the sheared-slab form of Lee, *et al.*[10] in the limit of weak shear and weak toroidicity. Figure 3.6 shows the variation of the growth rate with the toroidicity parameter $\varepsilon_n = L_n/R$. The mode becomes more unstable as ε_n increases to a threshold value of ~0.2 and becomes more stable for larger

toroidicities, possibly due to the stabilizing effects of increased shear. Figure 3.6 is qualitatively and quantitatively similar to Lee, *et al.*'s plot of growth rate against shear parameter L_n/L_s (Figure 3.4) if $L_s \sim R$.

Horton, *et al.* argue that the short-wavelength electrostatic η_e modes nonlinearly excite the longer-wavelength c/ω_{pe}-scale electromagnetic modes and pursue the turbulence into the nonlinear regime. Their nonlinear model will be discussed in section 3.4.

3.3.3 Gyrokinetic Model

The linear models discussed in Sections 3.3.1 and 3.3.2 require a finite ∇T_e ($\eta_e \neq 0$) and predict electrostatic modes with maximum linear growth at ρ_e spatial scales. Generally, these models yield qualitatively similar growth rates and real frequencies. Recently, however, Hirose[21] has studied electromagnetic drift modes that are linearly unstable at the larger c/ω_{pe} spatial scales with smaller growth rates and real frequencies.

In their fluid model Horton, *et al.* assume adiabatic ion response, $\lambda_\perp << \rho_i$, and predict c/ω_{pe}-scale magnetic turbulence. The relation $\rho_i = c/\omega_{pe}\sqrt{(\beta/2)(m_i/m_e)}$ implies that, in most tokamak plasmas ($\beta \sim$ few percent or less), ρ_i is only slightly larger than c/ω_{pe}. Thus, the assumption of adiabatic ion response is not well satisfied, and Hirose argues that both the electrons and the ions need to be analyzed kinetically. Hirose assumes sufficiently low $\beta, \beta_e << (m_e/m_i)\left(L_n/c/\omega_{pe}\right)$, so that the frequencies of interest $\omega \approx \omega^*_{ne}$ lie in the low-frequency regime, $\omega \approx \omega^*_{ne} << \omega_{ci}$, and that the electrons and ions can be described by gyrokinetic (drift kinetic) equations. [This

frequency assumption is not well satisfied in Tokapole II where $\omega^*_{ne} \leq \omega_{ci}$. For $q_a \sim 1$ discharges, for example, $\omega^*_{ne} \sim 3$ MHz at ρ_i scales and $\omega_{ci} \sim 4.5$ MHz. For $q_a \sim 1$ discharges $\beta_e \sim (m_e/m_i)\left(L_n/c/\omega_{pe}\right)$, and for $q_a \sim 3$ discharges $\beta_e \leq (m_e/m_i)\left(L_n/c/\omega_{pe}\right)$.] Under these assumptions, Hirose derives and analyzes a local, collisionless dispersion relation for electromagnetic modes. He considers the simplistic case of a plasma with $\eta_e = 0$ and no trapped particles to argue that instability requires only inverse Landau damping of untrapped electrons and ∇n as the source of free energy. Neither an electron temperature gradient nor trapped electrons is required. A more realistic case including a finite ∇T_e and trapped electrons shows that the growth rates are enhanced. In either case, the growth rates and frequencies are roughly an order of magnitude lower than predicted by the linear theories of Lee, *et al.* and Horton, *et al.* The range of real frequencies corresponding to positive growth does not match well the frequency range of the observed magnetic enhancement.

3.4 Nonlinear η_e Model

Horton and coworkers have performed the only nonlinear investigation to date of the η_e mode turbulence[13][15][19][20]. Their work is a development of a suggestion by Guzdar, *et al.*[11] that the nonlinear evolution of the short-λ drift instabilities driven by ∇T_e at the shorter ρ_e spatial scales may be responsible for turbulence at the longer c/ω_{pe} scales.

In the nonlinear regime two spatial scales play a role in the evolution of the turbulence from linear growth to nonlinear saturation. The maximum

linear growth occurs at the shorter ρ_e spatial scales, the polarization is primarily electrostatic, and the subsequent transport is small compared to that due to other processes (η_i turbulence, for example). Nonlinear mode coupling to larger spatial scales is expected by analogy with results of nonlinear simulations of η_i mode turbulence which have similar model equations. Results of computer simulations performed by Horton, *et al.*,[15][19] show that mode coupling drives the turbulence to longer spatial scales near the collisionless skin depth c/ω_{pe} and perhaps larger.

An Argument for the Existence of Two Spatial Scales

Horton, Hong and Tang give a simple (linear) argument for the existence of two separate spatial scales in the nonlinear regime. They consider magnetic fluctuations with a non-Boltzmann electron response for which the parallel conductivity is $\sigma^e_{\|} = (in_e e^2/m_e\omega)(1 - \omega^*_{pe}/\omega)$. Using Ohm's law, $j_{\|} = \sigma^e_{\|} E_{\|}$, with $\tilde{E} = -\nabla\tilde{\phi} + i\omega\tilde{A}_{\|}\hat{b}$, the parallel component of Ampère's law becomes

$$\left[\nabla_\perp^2 - \frac{\omega_{pe}^2}{c^2}\left(1 - \frac{\omega^*_{pe}}{\omega}\right)\right]\tilde{A}_{\|} = -\frac{\omega_{pe}^2}{c^2}\left(1 - \frac{\omega^*_{pe}}{\omega}\right)\frac{k_{\|}\tilde{\phi}}{\omega}, \tag{3.3}$$

where $\omega^*_{pe} = \omega^*_{ne} + \omega^*_{Te} = \omega^*_{ne}(1 + \eta_e)$. This is used to calculate $\tilde{E}_{\|}$ which takes the form

$$\tilde{E}_{\|} = -\nabla_{\|}\tilde{\phi}\,\frac{k_\perp^2}{k_\perp^2 + k_s^2}, \tag{3.4}$$

where $k_s^2(\omega,k) = (\omega_{pe}/c)^2(1 - \omega^*_{pe}/\omega)$. Substituting the approximate ω and k

corresponding to maximum linear growth (Section 3.3.2) into the form of $k_s(\omega,k)$ with $\tau \sim 1$ and $\eta_e >> 1$ gives

$$k_s c/\omega_{pe} \sim \left(\frac{\eta_e}{2\,\varepsilon_n}\right)^{1/2} = \left(\frac{1}{2}\,\eta_e \frac{R}{L_n}\right)^{1/2}. \qquad (3.5)$$

In Tokapole II, $k_s c/\omega_{pe} \sim 4$, or $\lambda_s \sim 1.5\, c/\omega_{pe}$, which is roughly midway between c/ω_{pe} and ρ_i but much larger than ρ_e. At the small spatial scales, $k_\perp^2 >> k_s^2$, Eq. (3.4) gives $\tilde{E}_\parallel \sim -\nabla_\parallel \tilde{\phi}$ and $\tilde{A}_\parallel \approx 0$, implying primarily electrostatic polarization and weak coupling, $k_\perp^2/\left(k_\perp^2 + k_s^2\right) \approx 1$. At the larger scales, $k_\perp^2 \le k_s^2$, Eq. (3.4) gives $\tilde{E}_\parallel \sim -\nabla_\parallel \tilde{\phi}\; k_\perp^2/k_s^2$, implying $\tilde{A}_\parallel \neq 0$ and the existence of strong coupling, $k_\perp^2/k_s^2 \approx 1$, which reduces $\tilde{E}_\parallel$ and changes the polarization from electrostatic to electromagnetic.

Ampère's law, Eq. (3.3), in this simple case also indicates how the c/ω_{pe} scale length enters the model. Note that in the further simplified case of $\tilde{\phi} = 0$ and long gradient sale lengths or high frequencies ($\omega^*/\omega \to 0$), Ampère's law reduces to $\left[\nabla_\perp^2 - \omega_{pe}^2/c^2\right]\tilde{A}_\parallel = 0$, and the amplitude of $\tilde{A}_\parallel$ falls exponentially in the perpendicular direction with an e-folding scale length of c/ω_{pe}. In a similar way, Ohkawa[1] uses a generalized Ohm's law to derive a differential equation in $\tilde{E}_\parallel$ similar to Eq. (3.3): $\partial^2 \tilde{E}_\parallel/\partial x^2 = \left[k_\perp^2 + \left(\omega_{pe}^2/c^2\right)\left(1 - \omega^*/\omega\right)\right]\tilde{E}_\parallel$. At high frequencies or long gradient sale lengths this equation also gives an exponential decay of $\tilde{E}_\parallel$ in the radial direction with maximum scale length $\sim c/\omega_{pe}$.

The Nonlinear η_e Model Equations

Horton, Hong and Tang[13] treat a set of nonlinear hydrodynamic equations describing η_e turbulence at short spatial scales. Their fluid model is based on the electron continuity equation, parallel force balance and energy conservation. They assume that the dominant nonlinear terms are the $\tilde{B}\cdot\nabla$ magnetic gradient due to field line perturbations caused by the turbulence and the E×B convective derivative ($\frac{\partial}{\partial t} + v\cdot\nabla$ with $v = v_{E\times B}$) acting on fluctuating quantities. The model assumes an adiabatic ion response, which is valid for $\lambda_\perp << \rho_i$ because the ions average over many wavelengths in a single gyro-period. (This assumption turns out to be a critical limitation of the model because the scale lengths of the saturated turbulence are expected to be $\sim c/\omega_{pe}$. In low-β machines like Tokapole II, $c/\omega_{pe} \le \rho_i$ and the assumption of an adiabatic ion response is not well satisfied. Horton and coworkers have plans to include a non-adiabatic ion response in the future[20][22].) Toroidal effects are included by adding ∇B and curvature drifts. To absorb energy transferred to $\lambda \to 0$ the model equations include classical (*i.e.* Braginskii[23]) diffusion coefficients for electron cross-field diffusion, resistivity and parallel and perpendicular thermal conductivity. The equations are normalized and reduced to a set of three coupled nonlinear partial differential equations in $\tilde{\phi}$, $\tilde{A}_\parallel$ and $\tilde{T}_e$ (or $\tilde{P}_e$). The reduction process is aided by assuming $\omega_{pe}/\omega_{ce} >> 1$ (high-density limit). For Tokapole II parameters this assumption is marginally satisfied: $\omega_{pe}/\omega_{ce} \sim 2$ - 4. The reduced equations are weakly 3-dimensional, retaining spatial derivatives in all three directions but with $\partial_\parallel << \partial_\perp$. The authors note that in the electrostatic limit ($\beta_e << m_e/m_i$) the toroidal η_e equations are similar in

structure to the toroidal η_i equations after an appropriate exchange of electron and ion dynamics has been made. The model equations are solved numerically and are discussed further in later works[15][19].

Preview of Stability for Tokapole II Parameters

We can preview the stability of the reduced nonlinear equations by solving the linearized system. If we replace each unknown function in the model equations by a plane-wave component of the form $\mathbf{u} = \mathbf{u}_{\mathbf{k}} \exp\left[i \left(\mathbf{k} \cdot \mathbf{x} - \omega t \right) \right]$ with $\mathbf{u} = (\tilde{\phi}, \tilde{A}_{\parallel}, T_e)$ and $\mathbf{x} = (x, y, z)$, the system takes the form of a generalized eigenvalue problem

$$\mathbf{A}\,\mathbf{u}_{\mathbf{k}} = -i\omega\,\mathbf{B}\,\mathbf{u}_{\mathbf{k}}. \tag{3.6}$$

Here, $\mathbf{A}$ is a general complex 3x3 matrix that depends on $k_\perp$, $k_\parallel$, the diffusion coefficients and other plasma parameters. The 3x3 matrix $\mathbf{B}$ is real, diagonal, non-singular, and depends only on $k_\perp$ and β_i. The inverse of $\mathbf{B}$ is trivial to calculate and can be used to simplify Eq. (3.6). Multiplying on the left by $\mathbf{B}^{-1}$ transforms the generalized eigenvalue problem to an ordinary eigenvalue problem

$$\mathbf{C}\,\mathbf{u}_{\mathbf{k}} = -i\omega\,\mathbf{u}_{\mathbf{k}}, \tag{3.7}$$

where $\mathbf{C} = \mathbf{B}^{-1}\mathbf{A}$. In general, ordinary eigenvalue problems are computationally easier to solve than generalized eigenvalue problems.

A computer code called LINEIGS[24] was used to solve the generalized eigenvalue problem Eq. (3.6) for the maximum growth rate as a function of k_x, k_y, and k_z. Here, maximum growth does not refer to a maximum with respect to variations in k_x, k_y, and k_z; rather, it refers to the largest imaginary part of the three eigenfrequencies obtained by solving Eqs. (3.6) or (3.7). A similar but more general procedure was used in reference [25] to solve the linearized system for the eigenfunctions $\tilde{\phi}$, $\tilde{A}_{\parallel}$, and $\tilde{T}_e$, and to compute linear estimates of electron thermal diffusivity and confinement times.

I obtained a copy of the LINEIGS code primarily so I could calculate real frequency information as well as the growth rates for realistic, Tokapole II parameters. However, the input plasma parameters supplied with the copy of the code I received were mutually inconsistent and unrealistic, corresponding to a cold or collisional plasma. The code which solves the nonlinear model equations was run with the same set of input parameters. The choice of unrealistic input parameters may have been necessary to get the computer solutions to reach a saturated state in a reasonable amount of time. Reference 15 contains the formulas for three of the five normalized diffusion coefficients, but it seems they were not used to generate mutually consistent input parameters. Neither Horton nor Lindberg, the author of the LINEIGS code, had the formulas for the other two coefficients. With assistance from Horton on technical details, I derived the remaining two diffusion coefficients in the normalized units used in the model equations and used Tokapole II parameters to obtain realistic and consistent estimates for the coefficients. The code was also modified to solve the simpler problem

Eq. (3.7) rather than Eq. (3.6) and to reduce storage and processing time requirements.

Figure 3.7(a) shows the maximum linear growth rate computed by the LINEIGS code for Tokapole II parameters for $k_z = 0$ and several values of k_x. On the plot axes, 1 frequency unit / $2\pi \approx 10$ MHz for Tokapole II parameters, and 1 wavenumber unit $\approx$ 18 rad/mm (assuming $\rho_{ci} \approx 0.03$ mm). The peak in the maximum growth rate in the $k_x k_y$ plane occurs in the $k_z = 0$ case for $k_x = 0$ and $k_y \rho_{ci} \approx 0.5$, corresponding to $\lambda_y \approx 13\rho_{ci} \sim 0.4\text{mm} \sim 6\rho_e \sim 0.3\rho_i$. The peak growth rate is $13.8 \cdot 10^6\, s^{-1}$. The location of the peak shifts to lower k_y and the peak value falls as k_y is reduced to zero, indicating that the modes are more stable at longer wavelengths.

Figure 3.7(b) shows the real frequencies corresponding to the maximum growth rates plotted in Figure 3.7(a). The thick portion of each curve marks the real frequencies for which the maximum growth rates are positive. Generally, the range of frequencies corresponding to positive growth rates is broad, spanning ~1 to ~2 decades. For the $k_x \rho_{ci} = 0$ and 0.25 cases, the range of frequencies corresponding to positive growth extends from 200 kHz to 22 MHz. The cross drawn on each curve marks the frequencies corresponding to the peaks of the maximum growth rate curves. The frequencies of peak growth lie between 4 MHz and 6 MHz, with the higher frequencies occurring at larger k_y.

The results of the LINEIGS code runs are in general agreement with the real frequency and growth rate predictions of the linear theories due to Lee, *et al.* (Section 3.3.1) and Horton, *et al.* (Section 3.3.2): rapid linear growth

rates at ρ_e spatial scales and high frequencies. Results of the nonlinear simulations[15][19] (discussed below) indicate that the saturated magnetic turbulence is dominated by components with $k_z = 0$ and $k_x \approx k_y$. Runs of the LINEIGS code modified to calculate γ and ω_r as functions of $k_x = k_y$ for $k_z = 0$ produced plots similar to those in Figure 3.7 with the exception of slightly lower values of γ and ω_r.

Numerical Solution of the Nonlinear η_e Model Equations

The nonlinear η_e model equations solved in reference [13] and described above are solved numerically in References 15 and 19. The code solves the model equations for the eigenfunctions $\tilde{\phi}$, $\tilde{A}_\parallel$ and $\tilde{T}_e$ in k-space and follows the evolution of the modes from the linear growth phase into saturation. The code also calculates the energy contained in the fluctuations associated with each eigenfunction,

$$
\begin{aligned}
E_{\tilde{\phi}} &= \frac{1}{2}\left\langle \tilde{\phi}^2 + \left(\nabla_\perp \tilde{\phi}\right)^2 \right\rangle, \\
E_{\tilde{A}_\parallel} &\propto \frac{1}{2}\left\langle \left(\nabla_\perp^2 \tilde{A}_\parallel\right)^2 + \frac{\beta_i}{2\tau}\left(\nabla_\perp \tilde{A}_\parallel\right)^2 \right\rangle, \\
E_{\tilde{T}_e} &\propto \frac{1}{2}\left\langle \tilde{T}_e^{\,2} \right\rangle,
\end{aligned}
\tag{3.8}
$$

and follows the redistribution of the total energy $E = E_{\tilde{\phi}} + E_{\tilde{A}_\parallel} + E_{\tilde{T}_e}$ among its three components. (In the earlier work and in some of the plots reproduced below the authors calculate the energy $E_{\tilde{P}_e}$ of the electron pressure fluctuations which is related to $E_{\tilde{T}_e}$ by $\tilde{P}_e = \tilde{T}_e - \tau\tilde{\phi}$.) Figure 3.8(a), for example, shows the linear growth phase and saturation of each energy component as

a function of time. The k_y spectrum of the total energy is plotted in Figure 3.8(b) at various times in the evolution of the modes. During the linear growth phase, corresponding to $t \leq t_1$, the spectra are dominated by components at $k_x\rho_{ei} \sim k_z L_n \approx 0$ and $k_y\rho_{ei} \approx 0.8$ [15] with $\gamma_m \sim 0.3\, v_{ei}/L_n$ ($\gamma_m/2\pi \sim 3{\cdot}10^6\, s^{-1}$ for Tokapole II parameters). This is consistent with the results obtained from the LINEIGS code described above. In the steady state, corresponding to $t \geq t_1$, the E × B flows are chaotic in space and the initially small and random magnetic fluctuations have evolved into large-scale ($\geq c/\omega_{pe}$) magnetic vortices. The turbulence is isotropic in x and y as shown in Figure 3.9(a) and (b) and is dominated by components at $k_z \sim 0$ and $k_x\rho_{ei} \sim k_y\rho_{ei} \sim \sqrt{\beta_e/2} \approx 0.05$ to 0.10 (for $\beta_e = 1\%$), the two lowest modes permitted in the x-y box. In terms of c/ω_{pe}, the spectra 'peak' at $k_x c/\omega_{pe} \sim k_y c/\omega_{pe} \approx 0.7 - 1.4$.

The spatial character of the turbulence can be seen in Figures 3.10 and 11 below. A contour plot of the normalized $\tilde{A}_{\parallel}(x,y)$ in saturation is shown in Figure 3.10 along with the ρ_i and c/ω_{pe} scale lengths. The regions of positive and negative $\tilde{A}_{\parallel}$ are enclosed by solid and dashed lines, respectively. Many features appear to have characteristic size $\sim c/\omega_{pe}$. However, one can also see larger spectral components in which the approximate distance between the centers of positive and negative regions is ρ_i. The large, box-size spatial components of the steady-state $\tilde{A}_{\parallel}$ can also be seen in the surface plot of $\tilde{A}_{\parallel}(x,y)$ in Figure 3.11(a). The saturated $\tilde{\phi}(x,y)$ and $\tilde{T}_e(x,y)$, Figures 3.11(b) and (c), have successively finer spatial structure down to $\sim \rho_e$ scales. The isotropic nature of the steady state can also be seen in these plots.

During the transition from linear growth to saturation, mode coupling transfers the fluctuation energy from the ρ_{ei} scales ($k_y\rho_{ei} \lesssim 1$) to the longest wavelengths in the simulation grid ($k_x \sim k_y \sim k_{min} \sim \omega_{pe}/c$)[19]. Thus, one cannot see a distinct peak in the $k_\perp$ spectra near c/ω_{pe} due to a lack of resolution in $k_\perp$ and the limited size of the simulation box. This leads one to ask the question: if the simulation grid were larger, would the energy be transferred to yet larger spatial scales?

Typically the nonlinear simulations were run with $\beta_e = 1\%$ and $\tau = 1$. [Taking $\tau = 1$ implies that $\rho_{ei} = \rho_e$ (and $\rho_s = \rho_i$). This is useful for comparing the nonlinear theory (reference [13]), where lengths are scaled to ρ_{ei}, with the results of the simulations (references [15], [19] and [20]), where ρ_e and ρ_{ei} seem to be used interchangeably.] The value of β_e is important because it sets the relative size of the ρ_e and c/ω_{pe} scales via $\rho_e\omega_{pe}/c = \sqrt{\beta_e/2}$. This ratio specifies the maximum $k_x\rho_e \sim k_y\rho_e$ grid spacing which is consistent with being able to identify a spectral peak at $k_{x,y}\rho_e \sim \omega_{pe}/c$. The value $\beta_e = 1\%$ used in the simulations gives $\rho_e\omega_{pe}/c = 0.07$.

Horton and coworkers have attempted to relieve concerns over the lack of spatial resolution in the simulations at small $k_{x,y}$. References [15], [19] and [20] contain results of simulations run on the original coarse grid of $L_x \times L_y = 10 \cdot 2\pi\rho_e \times 10 \cdot 2\pi\rho_e$ with $k_{x,y}^{min}\rho_e = 0.10 \geq \rho_e\omega_{pe}/c$. The k-spectra generated by these runs (Figures 3.8 and 3.9) lack a distinct peak near $k_{x,y} = \omega_{pe}/c$. The absence of such a peak may be related to the lack of resolution at the small $k_{x,y}$, or the turbulent energy may be trying to make its way to other yet smaller $k_{x,y}$. In later studies using the same model on a spatial

grid twice as large[20][22], the minimum $k_{x,y}$ was reduced by half to $k_{x,y}^{min}\rho_e = 0.05 \leq \omega_{pe}/c$, which marginally satisfies the criterion for resolving a spectral peak near ω_{pe}/c.

Because $E\widetilde{_{A_\parallel}}$ contains contributions from both $\widetilde{B}_\perp^2$ (through $\mathbb{B} = \nabla\times\mathbb{A}$ which gives the $(\nabla_\perp A_\parallel)^2$ term in Eq. 3.8) and $v_{e\parallel}^2$ (through Ampère's law which gives the $\left(\nabla_\perp^2 A_\parallel\right)^2$ term in Eq. 3.8), in the later runs we requested that Horton and coworkers isolate the magnetic fluctuation spectrum[26] from the spectrum of $E\widetilde{_{A_\parallel}}$. Figure 3.12 shows k_x and k_y spectra of the dimensionless magnetic fluctuation power $\widetilde{B}_\perp^2$. The k_x and k_y spectra have been integrated over $k_y k_z$ and $k_x k_z$, respectively. The authors give the mixing length estimate of the radial magnetic fluctuation level as

$$\frac{\widetilde{B}_x}{B} \sim k_\parallel \delta \sim \frac{c/\omega_{pe}}{qR}. \tag{3.9}$$

(For Tokapole II parameters this estimate gives $\widetilde{B}_x/_B \sim 10^{-3}$). The amplitudes of the saturated fluctuations in the numerical simulation are reported to agree roughly with the mixing length estimates and Eq. 3.9. As was the case with the coarse-grid simulations, the magnetic fluctuation energy is transferred to the largest non-zero mode in the simulation grid. Unlike the coarse-grid results, the lowest mode lies slightly below ω_{pe}/c, $k_{x,y}\rho_e = 0.05 \leq \rho_e\omega_{pe}/c$, and a spectral peak appears. However, the existence of the peak seems somewhat uncertain. There is only one point below the location of the peak to establish its existence. The value of $\widetilde{B}_\perp^2$ at $k_{x,y}\rho_e = 0$ is nonzero which is not consistent with $\widetilde{B}_\perp = k_y \widetilde{A}_\parallel$. It is not clear whether

the nonzero "DC" value of $\widetilde{B}_\perp^2$ is due to physics in the model or numerical effects. It is not clear whether the value at k=0 and, therefore, the peak itself, is real and meaningful.

Increasing the box size still more would increase the k-space resolution of the grid and would resolve more clearly and with more certainty a peak at $k_{x,y} \approx \omega_{pe}/c$. However, the box size cannot be increased indefinitely without penalty to the model itself: the assumption of adiabatic ions ($k_\perp \rho_i >> 1$) fails if the box size is too large. The coarse-grid ('small-box') and the fine-grid ('large-box') runs of the simulation had a $k_{x,y}$-space resolution of $k_{x,y}^{min}\rho_i = 4.3$ and $k_{x,y}^{min}\rho_i = 2.15$, respectively. The assumption of adiabatic ions is marginally satisfied for the small-box, low-resolution runs and is a poorer approximation for the larger-box, higher-resolution runs. Thus, a limitation of the present nonlinear model is its inability to clearly resolve a peak at $k_{x,y} \approx \omega_{pe}/c$ and simultaneously satisfy the adiabatic ion assumption for a realistic case in which ρ_i and c/ω_{pe} are similar. This limitation may be removed by revising the model to allow for a non-adiabatic ion response as Horton and coworkers had planned to do[20][22].

Issues Remaining to be Addressed

The studies done by Horton and coworkers on the linear η_e modes have described the characteristics of the primarily electrostatic modes, including the dispersion relations (i.e., $\gamma(k)$ and $\omega(k)$), instability threshold values of η_e, and so on. The results to date of the nonlinear simulations characterize the linear growth and eventual saturation of the high-frequency, electromagnetic

η_c turbulence. Much has been learned from the nonlinear simulations, but many issues have not been addressed. For example, wavenumber spectra of $E_{\tilde{\phi}}$, $E_{\tilde{A}_\parallel}$, $E_{\tilde{T}_e}$, $\tilde{v}_{e\parallel}$ and $\tilde{B}_\perp$ have been computed for model parameters. Of these five quantities, only the k-spectra of $\tilde{B}_\perp$ are routinely measured, and the measurement of k-spectra is not trivial. The nonlinear simulation does not store the time histories of the fluctuating field quantities, so the ensemble-averaged real-frequency spectra of $\tilde{B}_\perp$, $\tilde{\phi}$ and $\tilde{T}_e$ in saturation cannot be calculated. It is unfortunate that frequency spectra are experimentally much easier to generate than wavenumber spectra, and that the reverse is generally true theoretically. The simulations show how energy is transferred from the ρ_{ei} scales of maximum linear growth to the larger c/ω_{pe} scales (and perhaps to yet larger scales) as the turbulence enters the saturated state. But no one knows how the real frequency spectrum changes as the turbulence saturates. Do the real frequencies of $\tilde{B}_\perp$ shift to lower values as the turbulence saturates and the k-spectra peak shifts to smaller k? No one knows how well the linear real-frequency spectra ω_r (computed by LINEIGS) represent the saturated spectra. We have requested that the simulations be adapted to give the ensemble-averaged real-frequency spectra of experimentally measurable quantities such as $\tilde{B}_\perp$, $\tilde{\phi}$ and $\tilde{T}_e$. To date the codes have been modified to give only k-spectra of $\tilde{B}_\perp$ and $\tilde{v}_{e\parallel}$ in addition to $E_{\tilde{\phi}}$, $E_{\tilde{A}_\parallel}$ and $E_{\tilde{T}_e}$. I have supplied Horton and coworkers with the two unpublished formulas for the diffusion coefficients in the units used in the model as well as consistent, realistic values for all five normalized coefficients based on Tokapole II parameters. And I have requested that they attempt a Tokapole

II-like run of the nonlinear simulation modified to give the frequency and wavenumber spectra of $\tilde{B}_\perp$, etc. To date, this has not been done, perhaps because realistic and mutually consistent values of the diffusion coefficients make running the codes computationally impractical. Hopefully, future work will address some of these issues.

Figure 3.1. Normalized growth rate versus η_c for the 3 lowest modes, I–III, from Ref. 12. The lowest mode, I, is the most unstable.

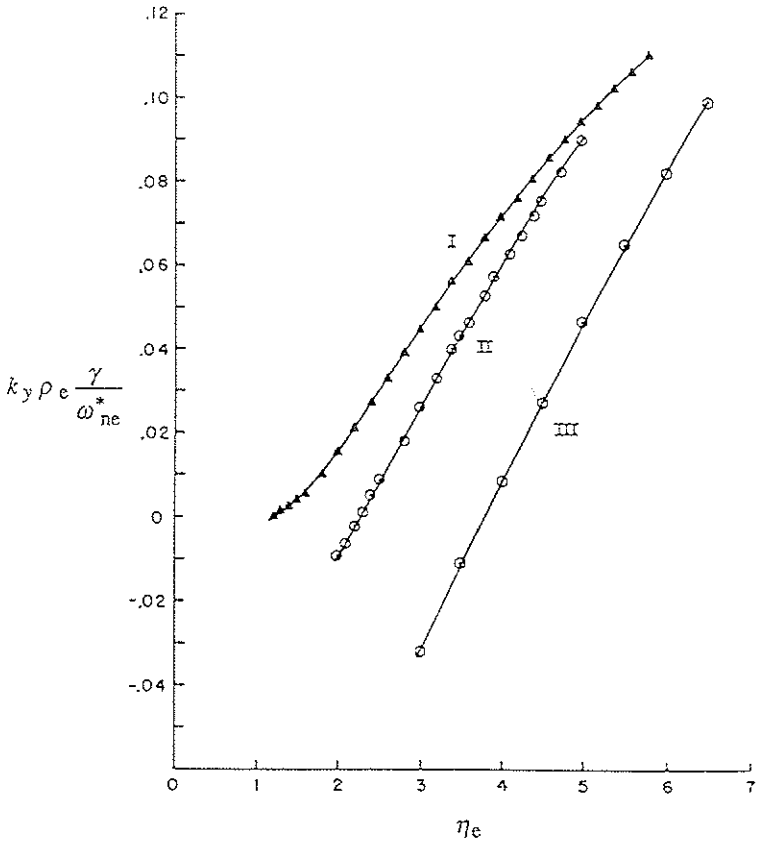

Figure 3.2. Radial solutions (a) $\tilde{\phi}$ and (b) $\tilde{A}_\parallel$ for mode I (———) and mode II (·····) with $k_y \rho_{ei} = 0.5$, $\beta_e = 1\%$, $\eta_e = 2$, and $L_n / L_s = 0.1$ from Ref. 12.

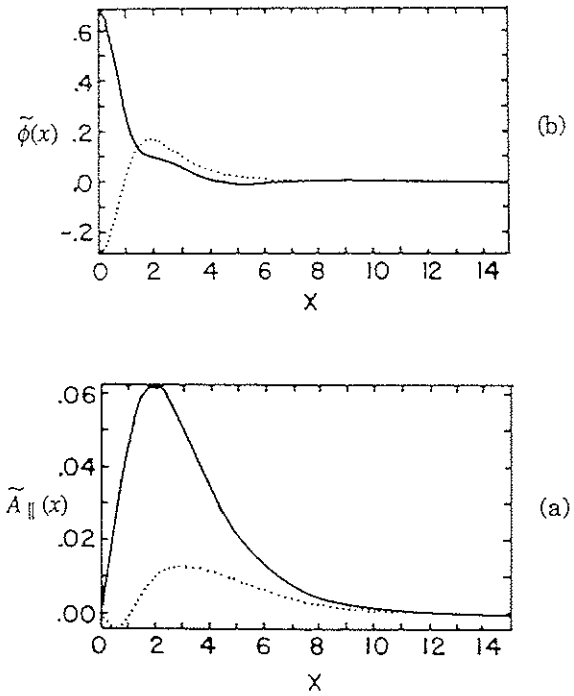

Figure 3.3. (a) Mode frequency ω_r and (b) growth rare γ versus $k_y \rho_{ci}$ for mode I with $\beta_e = 1\%$, $\eta_e = 2$, and $L_n / L_s = 0.1$ from Ref. 12.

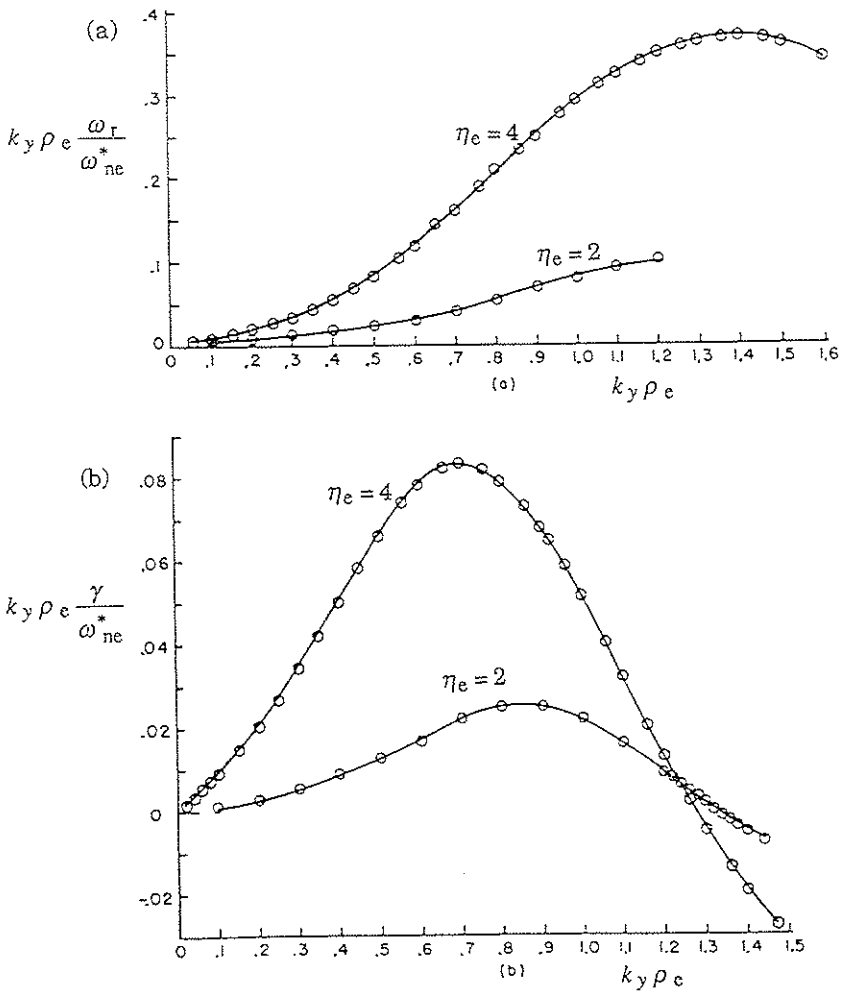

Figure 3.4. Growth rate versus shear L_s^{-1} for modes I–III, $k_y \rho_{ci} = 0.5$, $\beta_e = 0$, $\eta_e = 4$ from Ref. 12.

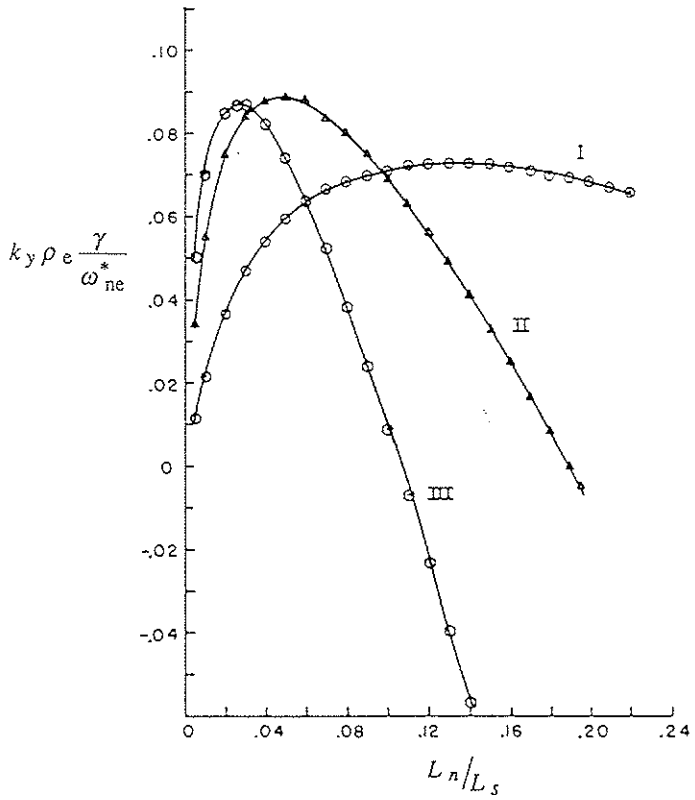

Figure 3.5. Results of kinetic calculation in Ref. 13 showing the variation of (a) mode frequency ω_r and (b) growth rate γ with η_e and the critical value at $\eta_e \approx 2/3$.

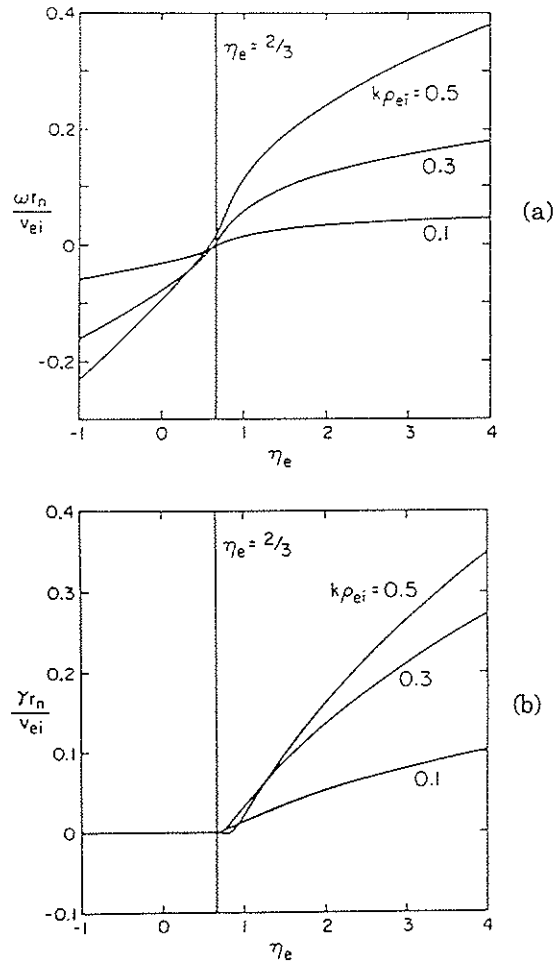

Figure 3.6. Growth rate as a function of toroidicity for $k_y \rho_{ei} = 0.3$ from the kinetic calculation of Ref. 13.

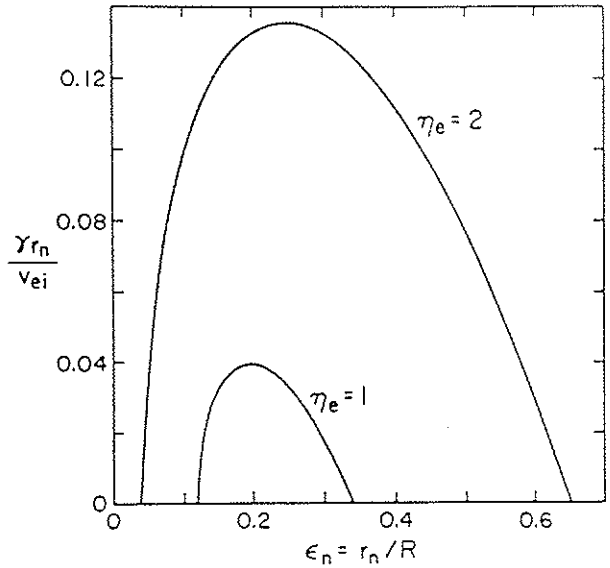

Figure 3.7. (a) Maximum linear growth rates computed by LINEIGS code for Tokapole II parameters $k_z L_n = 0$. (b) Real frequencies corresponding to the growth rates in (a). Thick lines correspond to positive growth. Dimensioned values are based on Tokapole II parameters.

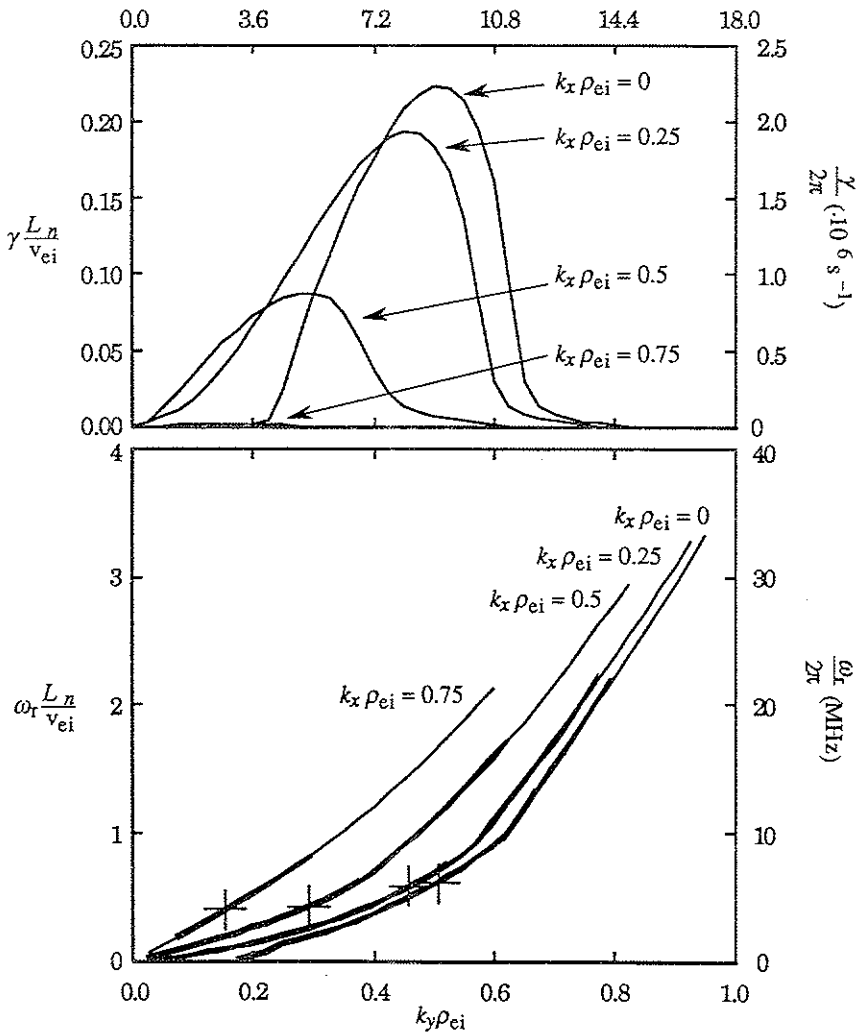

Figure 3.8. (a) Evolution of each component of the total fluctuation energy from the growth phase to steady state. (b) Spectral redistribution of total energy as the turbulence saturates. Taken from Ref. 19.

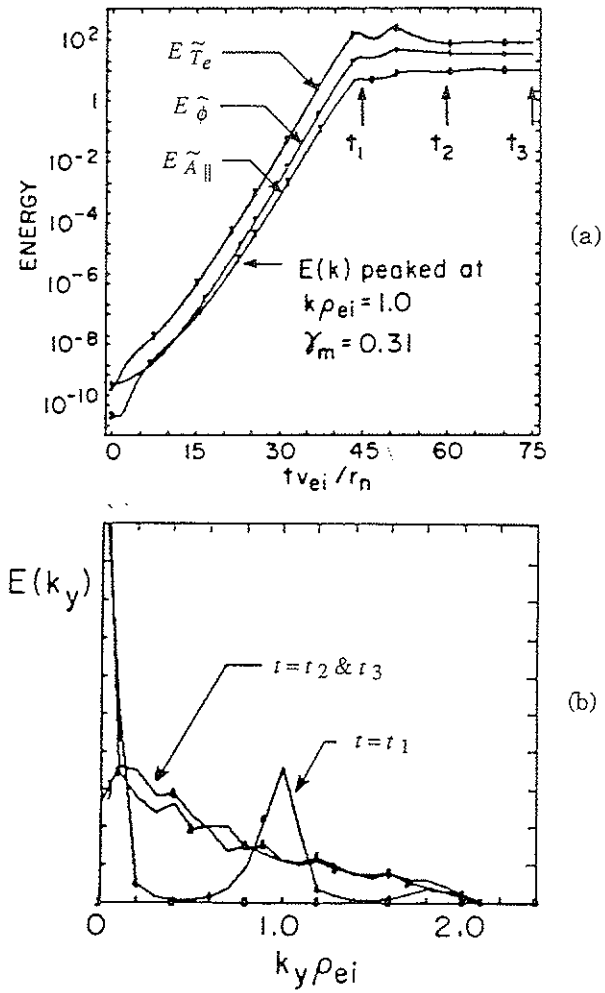

Figure 3.9. Steady-state spectra of energy of electron pressure fluctuations versus $k_x\rho_{ei}$ and $k_y\rho_{ei}$ shows isotropic nature of the turbulence. Taken from Refs. 15 and 19.

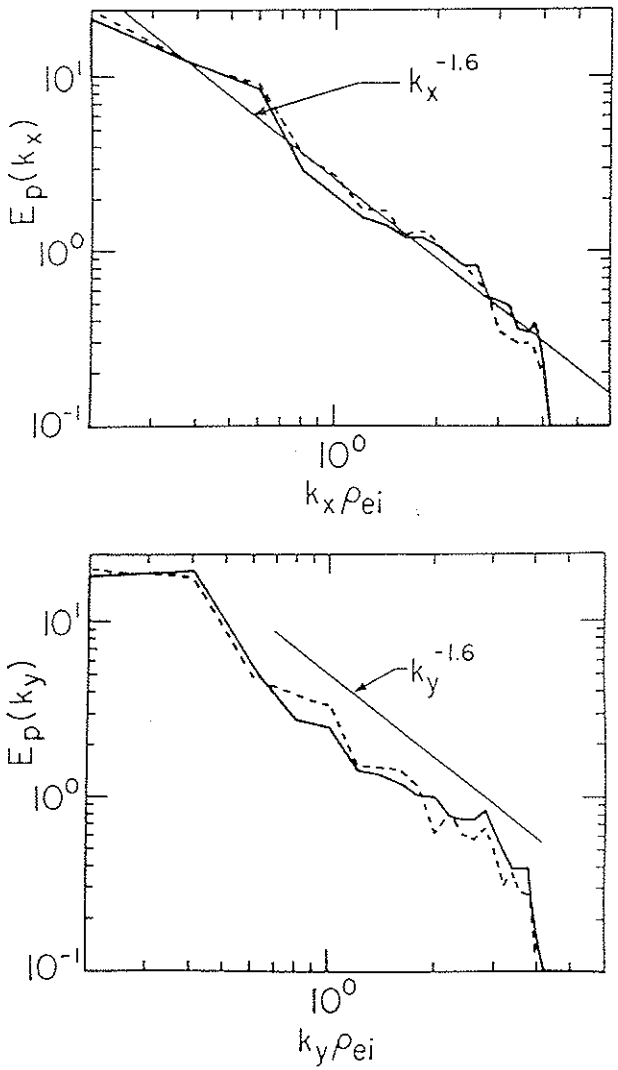

Figure 3.10. Contour plot of normalized $\tilde{A}_\parallel$ in saturation from the large-box, high-k-resolution simulations [20]. Regions of positive and negative $\tilde{A}_\parallel$ are enclosed by ——— and - - - - -, respectively. The ρ_i and c/ω_{pe} scales are indicated.

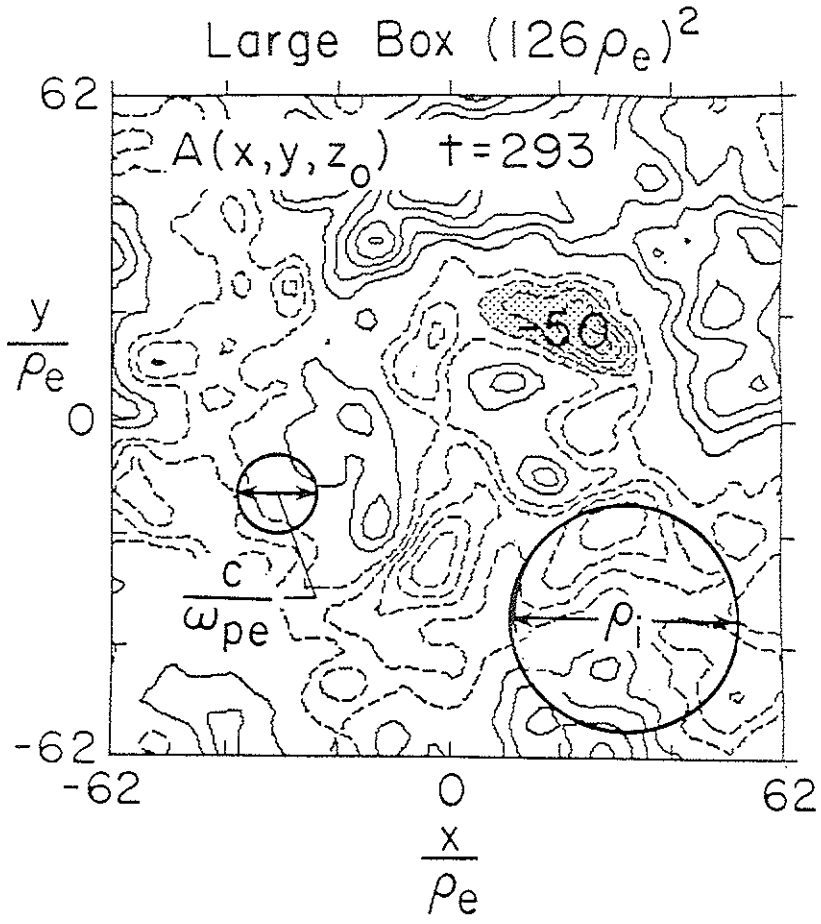

Figure 3.11. Surface plots of normalized (a) $\tilde{A}_{\parallel}$, (b) $\tilde{\phi}$ and (c) $\tilde{T}_e$ in steady state from the small-box, low-k-resolution simulations [20].

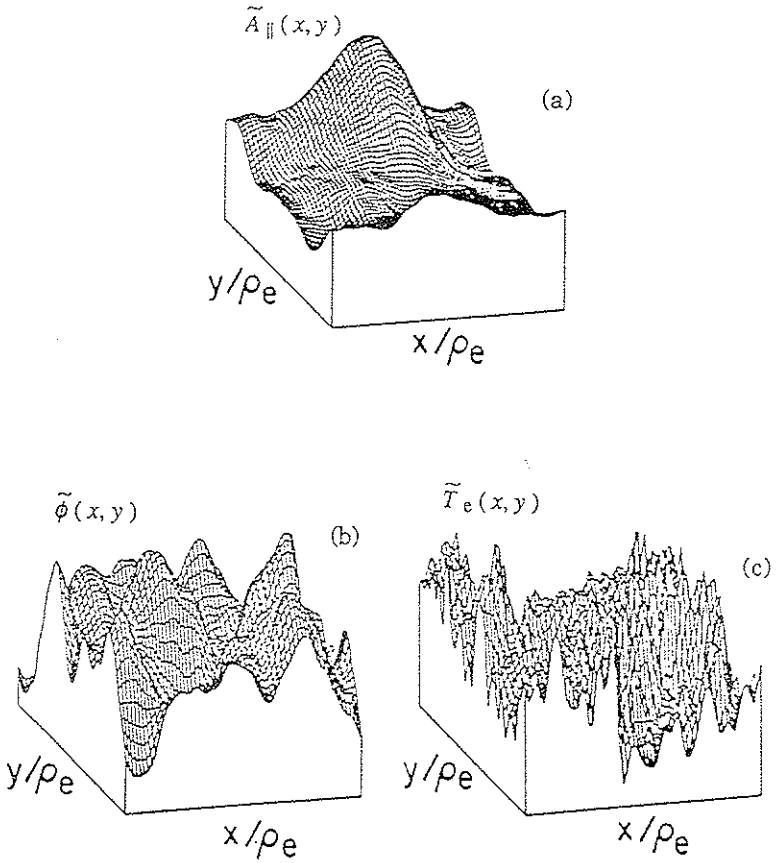

Figure 3.12. Dimensionless magnetic fluctuation power $\tilde{B}_{\perp}^2$ versus (a) $k_y \rho_{ei}$ and (b) $k_x \rho_{ei}$ [26]. The k_y and k_x spectra have been integrated over $k_x k_z$ and $k_y k_z$, respectively. The location of $k_{x,y}\rho_e = \rho_e \omega_{pe}/c = 0.07$ is indicated.

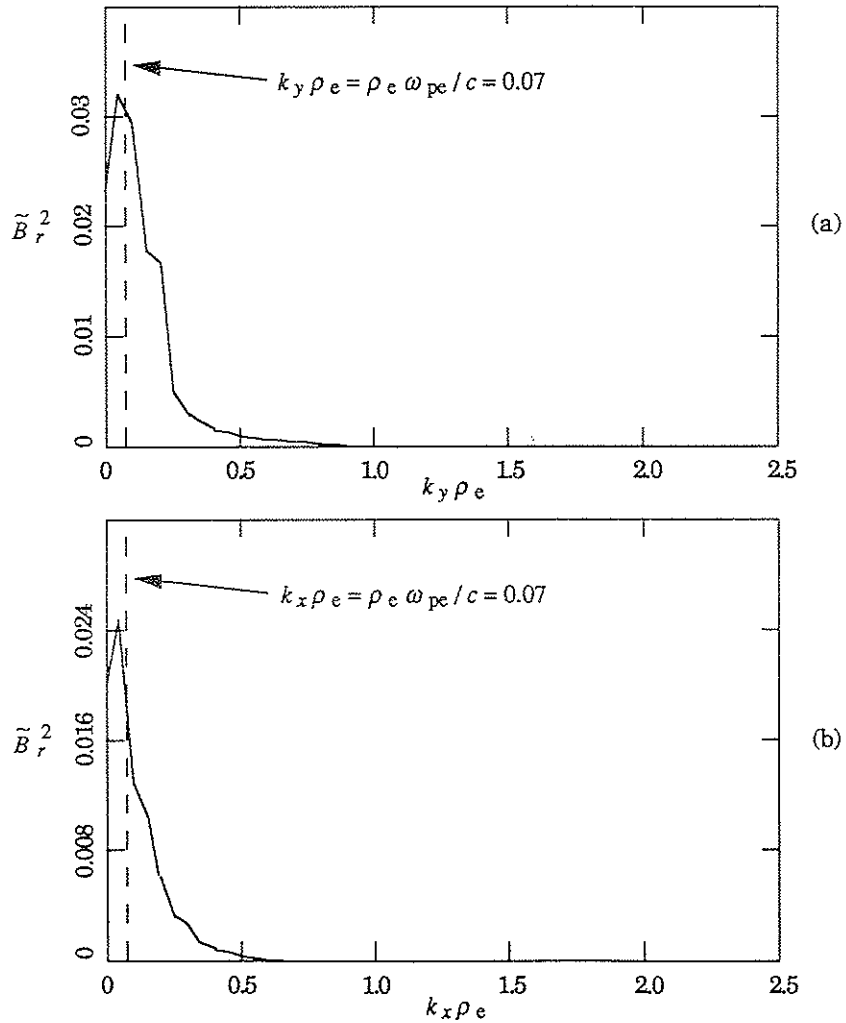

References

[1] T. Ohkawa, Phys. Lett. A **67**(1), 35 (1978).

[2] B. B. Kadomstev and O. P. Pogutse, in *Plasma Physics and Controlled Nuclear Fusion Research, 1978*, Proceedings of the Seventh International Conference, Insbruck (IAEA, Vienna, 1979), Vol. I, p. 649.

[3] V. V. Parail and O. P. Pogutse, in *Plasma Physics and Controlled Nuclear Fusion Research, 1980*, Proceedings of the Eighth International Conference, Brussels (IAEA, Vienna, 1981), Vol. I, p. 67.

[4] P. C. Liewer, Nucl. Fusion 25, 543 (1985).

[5] W. M. Tang, Nucl. Fusion 10, 1089 (1978).

[6] W. Horton, in *Basic Plasma Physics II*, ed. by A. A. Galeev and R. N. Sudan, North Halland, 383 (1985).

[7] J. D. Callen, Phys. Rev. Lett. **39**(24), 1540 (1977).

[8] R. E. Waltz, Phys. Fluids **28**, 577 (1985).

[9] G. Rewoldt, W. M. Tang and R. J. Hastie, Phys. Fluids **30**(3), 807 (1987).

[10] G. S. Lee and P. H. Diamond, Phys. Fluids **29**(10), 3291 (1986).

[11] P. N. Guzdar, C. S. Liu, J. Q. Dong and Y. C. Lee, Phys. Rev. Lett. **57**(22), 2818 (1986).

[12] Y. C. Lee, J. Q. Dong, P. N. Guzdar and C. S. Liu, Phys. Fluids **30**(5), 1331 (1987).

[13] W. Horton, B. G. Hong and W. M. Tang, Phys. Fluids **31**(10), 2971 (1988).

[14] P. W. Terry, J. N. Leboeuf, P. H. Diamond, D. R. Thayer, J. E. Sedlak and G. S. Lee, Phys Fluids **31**(10), 2920 (1988).

[15] W. Horton, B.-G. Hong and T. Tajima, Comments Plasma Phys. Contr. Fusion E **13**(4), 207 (1990).

[16] C. S. Liu, Phys. Rev. Lett. **27**, 1637 (1971).

[17] I. H. Tan, R. N. Dexter, S. C. Prager and T. D. Rempel, Bull. Amer. Phys. Soc. **34** poster 1Q9, 1923 (1989).

[18] R. A. Moyer, Ph. D. Thesis, University of Wisconsin–Madison, 1988.

[19] N. Bekki, W. Horton, B.-G. Hong and T. Tajima, Institute for Fusion Studies Report #364, University of Texas–Austin, February, 1989.

[20] W. Horton, S. Hamaguchi, C.-B. Kim, presented at U.S.-Japan Workshop on Fluctuations in RFP and ULQ Plasmas, University of Wisconsin–Madison, Madison, WI, 1990.

[21] A. Hirose, Department of Physics Preprint, University of Saskatchewan, Saskatoon, SASK, 1991; to appear in Phys. Fluids B.

[22] W. Horton, private communication, March and July, 1990.

[23] S. I. Braginskii, in *Reviews of Plasma Physics*, Ed. by M. A. Leontovich, Consultants Beurau, New York, 1, 205 (1965).

[24] D. M. Lindberg, computer code LINEIGS (Institute for Fusion Studies, University of Texas–Austin, Austin, TX, 1988).

[25] W. Horton, B.-G. Hong, T. Tajima and N. Bekki, in *Theory of Fusion Plasmas*, ed. by J. Vaclavik, F. Troyon and E. Sindoni (Editrice Compositori, Bologna, 1988), p. 483.

[26] W. Horton, private communication, October and November, 1989.

CHAPTER 4

Experimental Results and Their Relation to Theory

Comparisons of radial magnetic fluctuation spectra measured in various ranges of poloidal wavelength are described in this chapter. The measurements span the range of frequencies from ~ 10 kHz to ~ 6 MHz ($0.01 \leq \omega/\omega^*_{ne} \leq 1$, based on $\omega^*_{ne} \sim 3$ MHz for $\lambda_y \sim \rho_i \sim 2$ mm) at spatial scales extending below the collisionless skin depth, c/ω_{pe}, to the ion gyroradius, ρ_i. The basic result is that at the higher frequencies (~ 500 kHz to ~ 2 MHz) the smaller probes measure up to an order of magnitude more power than the large probes. This implies that fluctuation activity is stronger at the short, ρ_i-size wavelengths than at the longer wavelengths at the high frequencies. The focus of the experiments described here, and of this thesis in general, is on measuring and comparing radial magnetic fluctuation spectra and on characterizing the enhanced small-scale fluctuations. The more general topics of magnetic turbulence and transport in Tokapole II are discussed at length by Graessle[1] and LaPointe[2].

Section 4.1 contains a description of the experimental approach. The experimental results are presented in Section 4.2. Frequency spectra and radial profiles are presented for various values of q_a. In each case we compare small- and large-scale fluctuations. Finally, in Section 4.3, the experimental results will be compared with the results of the theoretical and computational work summarized in Chapter 3.

4.1 Description of Experimental Approach

The experimental approach used to observe the increased fluctuation power at small spatial scales is direct, relatively simple, and novel. Magnetic probes were used to measure directly the fluctuations. Because probes with smaller shield diameters resolve fluctuations at smaller probe-transverse wavelengths (Section 2.4.2), $\dot{B}_r$ probes of different diameters were used to measure radial magnetic fluctuation spectra in different ranges of poloidal wavelengths. Two or more probes of different sizes were inserted radially into the discharge from the side of the machine. Comparisons of frequency spectra at various plasma positions show the range of frequency and the locations where the enhanced small-scale fluctuation activity occurs. Such comparisons are straightforward to carry out. The experimental approach is novel because, to my knowledge, no one else has used $\dot{B}$ probes in this way or has studied the short-wavelength, high-frequency response of $\dot{B}$ probes.

Other fluctuation diagnostics are not well suited to measuring small-scale (~ c/ω_{pe} to ρ_i) fluctuations. Microwave, CO_2-laser and FIR scattering diagnostics and heavy-ion-beam-probe diagnostics have the advantage of being noninvasive. But these systems generate volume-averaged measurements which typically cannot resolve c/ω_{pe} or ρ_i spatial scales.

Four probes of different overall diameter were used to acquire most of the data presented here: one 6.35 mm (1/4") probe; two 2 mm probes, one with a long coil (2.0 mm) and the other with a short coil (0.6 mm); and one 1 mm probe. Table 2.2 summarizes the physical characteristics of the probes

in more detail. Table 4.1 gives for each probe the minimum resolvable wavelengths in each direction and the probe scales that determine the λ_{min}. The toroidal separation of adjacent pairs of probes was 30° (the minimum possible) for most of the experiments. The measurements were performed in discharges with $q_a \approx 1, 2,$ and 3. Time series of the radial magnetic fluctuations were measured over a broad range of radial positions outside, across and inside the separatrix ($0.5 \lesssim r/a \lesssim 1.4$, where a is the separatrix position). Tokapole II discharges are sufficiently cool that even the smallest, most fragile probes can usually survive extended runs anywhere in the machine. However, discharge quality and reproducibility are typically degraded if the probe is inserted too far past the separatrix.

	6.35 mm (1/4") Probe	2 mm Probe (long coil)	2 mm Probe (short coil)	1 mm Probe
$\lambda_{y,z}^{min}$	10.7	4.0	4.0	2.0
outer radius b	2.67	1.0	1.0	0.5
max λ_x^{min}	8.9	6.6	2.0	7.9
based on	a=2.54	L_c=2.0	a=0.56	L_c=2.4

Table 4.1. Estimates for minimum resolvable wavelengths in the probe-transverse (y, z) and probe-axial (x) directions for each probe listed in Table 2.2. The units on all values are millimeters. The $\lambda_{y,z}^{min}$ is determined by the shield outer radius b and Eq. (2.9). The response to λ_x depends on four factors in Eq. (2.6). This table gives the largest of the three λ_x^{min} estimated using Eq. (2.10).

To compare data from different toroidal locations, we assume that the

turbulence is toroidally homogeneous, as expected from axisymmetry. This assumption was tested by swapping probes at different locations and checking the similarity of the measured spectra. Figure 4.1(a) shows radial magnetic fluctuation spectra measured at x=6 cm and x=12 cm by a 6.35 mm probe and a 2 mm probe. Both probes were located on the midplane at toroidal angles 180° and 270°. Figure 4.1(b) shows the spectra measured after the probes had been swapped. Other than the location of the probes the conditions were the same. With respect to change of probe location, the spectra are generally similar at both radial positions. There is a tendency for the probes at 180° to measure more power than the probes at 270°. This may indicate a toroidal asymmetry. The largest difference is at the lowest frequencies and may correspond to large-scale MHD activity and island structures. This swapping experiment was done for $q_a \approx 1$ discharges. The gap in the spectra was due to a limitation in an earlier configuration of the electronics which was not optimized for wide-band frequency response. At x=12 cm the spectra overlay fairly closely, but at x=6 cm the small-probe spectra in the high-frequency band are larger than the large-probe spectra. This difference is greater than the ~40% statistical scatter in these ensemble-averaged power spectra. The investigation of this difference is the subject of this thesis and will be described in greater detail in Section 4.2.

Two additional points must be made concerning the experimental approach and the short-wavelength response of the probes. First, the response of each $\dot{B}_r$ probe in Table 4.1 (except the short-coil 2 mm probe) to radial wavelengths is similar despite having very different coil lengths. Identical

radial response functions among different probes are difficult to create because the λ_x response is a complicated function of all five probe parameters (r_c, a, b, δ, and L_c). Each factor in the overall λ_x response can be characterized by a minimum resolvable radial wavelength $\lambda_x^{\min}$ at which the contribution from that factor to the response is reduced to 1/2. The largest $\lambda_x^{\min}$ can be taken as a lower bound on the 1/2-amplitude wavelength for the overall response. (The actual 1/2-amplitude λ_x will always be larger than the largest $\lambda_x^{\min}$.) Because all but the short-coil 2 mm probe have similar values for the largest $\lambda_x^{\min}$, they have a similar λ_x response. Therefore, we interpret these three probes as measuring approximately the same range of *radial* wavelengths. The second point is that a cylindrically symmetric probe cannot distinguish between poloidal and toroidal wavelength effects because its response to poloidal and toroidal wavelengths is identical (Eq. (2.11)). However, low-frequency measurements and most tokamak turbulence models (including the nonlinear η_e model in Section 3.4) indicate that $\lambda_z >> \lambda_y$. Under this assumption the response to the toroidal wavelengths lies in the long-wavelength regime and is identical for each probe used here. Hereafter we interpret probes with different diameters as measuring different ranges of *poloidal* wavelength. Thus, the three probes mentioned are reasonably well suited to discern the short *poloidal* wavelength character of Tokapole II turbulence. The three probes with similar radial response functions were used to make most of the measurements presented in this chapter.

Fluctuation Data Analysis

Data records used in the statistical ensembles were chosen to satisfy three general criteria. First, the records were taken at times corresponding to relatively flat q_a. Second, the records were taken at times before the first major sawtooth crash (as monitored by the soft x ray emissions) and not during periods when the SXR signals were varying rapidly. Third, the records were not chosen if they contained anomalous bursts or sudden variations in the general signal level. (The second and third criteria are not always the same in practice.) The second criterion is necessary because large-amplitude, rapid variations in the high-frequency $\dot{B}$ signals typically accompany rapid variations in the SXR emissions, especially for coils located inside the separatrix. This 'burstiness' is attributable to intermittent high levels of MHD activity.

The low-frequency $\dot{B}$ signals are not as sensitive to SXR activity. In fact, low-frequency raw data records corresponding to times of increased SXR activity often look very similar to low-frequency data taken during times of relatively quiet SXR activity. For these reasons the criteria listed above often exclude more high-frequency records than low-frequency records. In order to make the comparison of low-frequency and high-frequency spectra as fair as possible, the set of acceptable data records (i.e., those satisfying the criteria) were chosen to correspond as closely as possible to the same time periods. While it is always desirable to maximize the number of records in an ensemble to reduce the statistical scatter in the results, consistency

between low-frequency and high-frequency records is a more important consideration. All too often a compromise between minimizing statistical scatter and maintaining low-frequency/high-frequency consistency was made, but when ever possible, the latter consideration was favored. The amplifier/filter systems and the calibration of data are discussed in greater detail in Section 2.4.

4.2 Experimental Results

The discussion of the results is arranged by the edge-q value of the discharges in which the data was taken. Because β_e decreases as q_a increases in Tokapole II discharges, the arrangement of results by increasing q_a is equivalent to an arrangement of results by decreasing β_e. Electrostatic probe measurements[3] of n_e and T_e profiles in the edge region of Tokapole II discharges indicate that $\eta_e \sim 1-2$. Other characteristics of the discharges are described in Section 2.2.

$q_a \approx 1$ Results

Frequency spectra of the radial magnetic fluctuations in $q_a \approx 1$ discharges (with $\beta \sim 10\, m_e/m_i$) were measured at several radial positions in three ranges of poloidal wavelengths with three probes of different diameters as described above. The calibrated power spectra (*i.e.* the power spectral densities PSD's), were calculated for each probe and plotted for comparison. The PSD (proportional to G^2/kHz) measures the energy per unit bandwidth and does not depend on the sampling rate or on the length

of the records analyzed. The PSD is, therefore, preferred over other spectral estimates for making comparisons of frequency spectra.

The $q_a \approx 1$ results were obtained during two different run periods separated by more than a year. The first run was made with the 6.35 mm and 2 mm probes. After the 1 mm micro-probe was developed the run was repeated with the 1 mm and 6.35 mm probes. The spectra measured by the 6.35 mm probe in each run were similar over the most of the range of frequencies measured and typically did not differ by more than a factor of 2. The 1 mm probe results were added to the previous results. The power spectra measured inside the separatrix (x=6 cm) and outside (x=11 cm) are shown in Figures 4.2 and 4.3. Below the power spectra are plots of the ratio of the power measured by the 1 mm and 2 mm probes to that of the 6.35 mm probe. Ratios greater than unity indicated enhanced fluctuation activity at poloidal wavelengths between the minimum resolvable wavelengths of each probe. The $q_a \approx 1$ discharges exhibited the largest small-scale enhancement of any of the discharges examined. The enhancement was largest at x=5 cm and x=6 cm and between ~3 MHz and ~600 kHz, although increased power levels extended down to ~100 kHz. At x=6 cm the range of poloidal wavelengths $\lambda_y \geq 2$ mm resolved by the 1 mm probe contained as much as 20 times more power than the range $\lambda_y \geq 13$ mm measured by the 6.35 mm probe. And the range of poloidal wavelengths $\lambda_y \geq 4$ mm resolved by the 2 mm probe contained as much as 8 times more power than the range measured by the 6.35 mm probe. Though the small-probe power levels at the higher frequencies are much larger than for the 6.35 mm probe, they are still well below the power

levels measured by all probes at the lower frequencies.

The enhanced power levels may extend to frequencies above 3 MHz, but the flattening of the 6.35 mm and 2 mm probe spectra at the highest frequencies makes this unclear. The flattening of the spectra occurs when the $\dot{B}_r$ system calibration is applied to signal levels close to or below the noise levels. The high-frequency data from the 1 mm probe obtained during the later run had a larger signal-to-noise ratio and was fairly uniform in slope up to ~7 MHz.

The statistical scatter in the ensemble-averaged spectra for all q_a values varied greatly with frequency and radial position. A standard error (error in the mean) of ~40% was typical but was sometimes larger. Statistical scatter, toroidal asymmetry and other systematic errors may contribute to the difference between the spectra. As a general rule, a ratio of spectra greater than two will be considered significant. The error bars on the power spectra show the size of this overall factor of 2 uncertainty at various frequencies.

The degree to which the spectra converged at low frequencies varied greatly with q_a, radial position and the set of data records analyzed. In some cases the low ends of the spectra agreed to within 10%. In nearly all cases, however, the difference at the lowest frequencies was within the factor of ~2 total uncertainty. The fact that the 1 mm probe spectrum in Figure 4.2 does not show a tendency to converge with the other two spectra may indicate the presence of a systematic error between the two data runs. If this is the case, and if the same systematic error is present across the entire spectrum, then the 1 mm probe spectrum and its ratio are too low by a factor of ~2, and the

enhancement at the smallest measured scales is even larger than indicated by Figure 4.2. The variability of the convergence of the spectra at low frequencies may also be related to the low spectral resolution of the low-frequency spectra. For the $q_a \approx 1$ data the spectral resolution was $\Delta f = 19.53$ kHz. The lowest point shown in Figure 4.2 at 19.53 kHz is the only point above DC. Finer spectral resolution would presumably produce a more faithful reproduction of the spectra. Also, the frequency at which the spectra converge may lie below this point. This was seen in some cases for the $q_a \approx 2$ and $q_a \approx 3$ results which were taken more recently with finer spectral resolution in the low-frequency band.

Near the separatrix (x~8 cm) the difference between the small- and large-probe spectra is smaller than inside the separatrix. But the small-probe power levels are still significantly larger than those measured by the 6.35 mm probe. The range of poloidal wavelengths $\lambda_y \geq 2$ mm resolved by the 1 mm probe contained as much as 10 times more power than the range $\lambda_y \geq 13$ mm measured by the 6.35 mm probe. And the range of poloidal wavelengths $\lambda_y \geq 4$ mm resolved by the 2 mm probe contained as much as 5 times more power than the range measured by the 6.35 mm probe.

Outside the separatrix (Figure 4.3, x=11 cm) no significant increase of the small-scale fluctuations was observed. Below ~1 MHz all three probes measured spectra that were similar to within the factor of ~2 total uncertainty. Above ~1 MHz the spectra were not similar because the system noise dominated the signal. The calibrated spectra in this frequency range indicate an upper bound on the actual fluctuation spectra. The noise levels are different

because the overall system gains are different.

The cause of the narrow peak in the spectrum near 4.5 MHz for the two large probes (Figure 4.2, first data run) is unknown. The peak is located just below the ion cyclotron frequency (f_{ci} = 4.8 MHz) for these discharges. The peak was very reproducible during the run period and appeared consistently near and inside the separatrix. However, the peak was not seen in the later runs in the same discharges. The peak was also not seen in the $q_a \approx 2$ or $q_a \approx 3$ discharges, possibly because clean signals of sufficient amplitude could not be obtained in the range $f_{ci} \approx 7.5$ MHz for those discharges. The peak was probably not caused by resonant phenomena within the high-frequency amplifier/filter system because the peak was not seen outside the separatrix or during no-plasma shots.

Figure 4.4 summarizes the $q_a \approx 1$ small-scale fluctuation measurements. The ratios of the small-probe profiles to the 6.35 mm probe profiles in the low-frequency (f > 20 kHz) and high-frequency (f > 0.5 MHz) ranges are plotted in (a) and (b), respectively. The ratios of the profiles show the enhancement as a function of radial position. The error bars in each plot indicate the statistical scatter in the underlying data. At the higher frequencies (plot (b)) the 1 mm ($\lambda_y \geq 2$ mm) and 2 mm ($\lambda_y \geq 4$ mm) probes measure ~4 and ~2 times the fluctuation amplitude of the reference probe ($\lambda_y \geq 13$ mm). At the lower frequencies (plot (a)) the small probes measure slightly more power than the reference probe. The profiles of $\tilde{B}_r / B$ measured by each probe at low and high frequencies are shown in plots (c) and (d). The vertical scales of (c) and (d) are given in units of the common value at

the edge. The edge values of the fluctuation levels are $\sim 10^{-4}$ and $\sim 10^{-6}$ in the low- and high-frequencies, respectively, and are indicated by the dashed lines on plots (c) and (d). The maximum enhanced fluctuation level for the $q_a \approx 1$ discharges is $\sim 3 \cdot 10^{-5}$ and occurs at x=5 cm for f > 0.5 MHz. Inside the separatrix or at the higher frequencies the small-λ_y fluctuation levels rise faster than the long-λ_y or low-frequency fluctuation levels. Outside the separatrix the fluctuation levels are similar in both frequency ranges and the profiles are flat.

The value of $\tilde{B}_r$ is calculated from an integral of the power spectrum and, because of the shape of the spectrum, is weighted at the end of the spectrum nearest the lower limit of integration. Thus, much of the information about the shape of the spectrum and the frequency regions of enhancement is lost in the calculation of $\tilde{B}_r$.

The enhancement of the short poloidal wavelength fluctuations is summarized in Figure 4.5. The power measured in the different ranges of λ_y can be converted into a simple histogram that shows the approximate distribution of power in k_y. The k_y distribution measured at x=6 cm and x=11 cm for a few frequencies below and within the range of enhancement is shown in Figure 4.5. The histograms at the radial locations and frequencies shown are representative of the histograms at similar x and f. For comparison, the range of k_y corresponding to $k_y = 2\pi/\rho_i$ and $k_y = \omega_{pe}/c$ for Tokapole II parameters is indicated. The area in the first bin ($k_y \leq 0.5$ rad / mm) represents the power measured by the 6.35 mm probe in the poloidal wavelength range $\lambda_y \geq \lambda_y^{min} \approx 12.7$ mm. The heights of all bins at each frequency are normalized

to the height of the first bin. Note the change of vertical scales at the different frequencies. The total area in the first and second bins ($k_y \leq 1.57$ rad / mm) represents the power measured by the 2 mm probe ($\lambda_y \geq \lambda_y^{min} \approx 4$ mm). And the total area in all three bins ($k_y \leq 3.14$ rad / mm) represents the power measured by the 1 mm probe ($\lambda_y \geq \lambda_y^{min} \approx 2$ mm). The strong spectral enhancement that is evident for x=6 cm near f≈2 MHz in Figure 4.2 appears in Figure 4.5 (a) for f≈1.91 MHz as a sharply increasing k_y distribution. The experimental distribution increases as k_y *increases* toward the ρ_i scales. However, the computation of the η_e modes (Section 3.4) predicts that the k_y spectrum increases as k_y *decreases* toward the c/ω_{pe} scales. The experimental and computational results presently lack resolution in the region of k_y above $k_y = 2\pi/\rho_i$ and below $k_y = \omega_{pe}/c$, respectively, so neither can demonstrate conclusively the existence of a peak near the ρ_i scales or near the c/ω_{pe} scales. Below the frequencies of enhancement ($f \leq 0.6$ MHz) the distribution decreases monotonically with k_y.

$q_a \approx 2$ Results

For the $q_a \approx 2$ discharges (with $\beta \sim 2\, m_e/m_i$) the largest degree of small-scale enhancement occurred just inside the separatrix. Figure 4.6 shows the spectra measured by the three probes at x=8 cm. Also shown are the ratios of the 1 mm probe and 2 mm probe spectra to the 6.35 mm probe spectra. The frequency range over which the strongest enhancement occurred was 600 kHz ≤ f ≤ 4 MHz with significant enhancement extending to 200 kHz, nearly the same range as for the $q_a \approx 1$ discharges. The range of poloidal

wavelengths $\lambda_y \geq 2$ mm resolved by the 1 mm probe contains nearly 5 times more power than the range $\lambda_y \geq 13$ mm measured by the 6.35 mm probe. And the range of poloidal wavelengths $\lambda_y \geq 4$ mm resolved by the 2 mm probe contains about 4 times more power than the range measured by the 6.35 mm probe. The enhancement measured by the two small probes relative to the 6.35 mm probe is smaller than for the $q_a \approx 1$ case. And the gap between the power measured by the two small probes is also smaller. The convergence of the low-frequency spectra was generally better than for the $q_a \approx 1$ data, possibly because the $q_a \approx 2$ and $q_a \approx 3$ data were analyzed with a finer spectral resolution in the low-frequency band.

Outside the separatrix (Figure 4.7, x=11 cm) no significant increase of the small-scale fluctuations was observed. All three probes measured similar spectra (within a factor of ~2) across both the low- and high-frequency bands. The narrow peak at 5 MHz is discussed with the $q_a \approx 3$ results.

In Tokapole II, discharges with $q_a \geq 2$ are perturbed more easily by probes inserted past the separatrix than are $q_a \approx 1$ discharges. In order to maintain consistency of global discharge parameters, the largest probe was not inserted more than a few centimeters past the separatrix. The $q_a \approx 2$ and $q_a \approx 3$ data runs provide power comparisons between the 1 mm and 2 mm probes over the same range of plasma positions as the $q_a \approx 1$ runs. However, comparisons with the 6.35 mm probe are only available from outside to just inside the separatrix. As the 6.35 mm probe was moved to x<7 cm the $q_a \approx 2$ discharges began to degrade noticeably and the fluctuation spectra began to decrease. Data was taken with the 6.35 mm probe at x=7 cm and was then

pulled out while the 2 mm and 1 mm probes were advanced to x=5 cm. It is not known if the enhancement between the 6.35 mm probe and the smaller probes persists inside the separatrix. Figure 4.8 compares the power spectra measured by the two small probes at x=6 cm and gives the ratio of the 1 mm probe power to the 2 mm probe power. The two small probes measure no significant difference in power at any frequency between 10 kHz and 5 MHz

Figure 4.9 summarizes the radial character of the $q_a \approx 2$ small-scale fluctuations in the same format as Figure 4.4. The profiles show that the small-scale enhancement is strongest just inside the separatrix and in the high-frequency band (plots (b) and (d)). At the higher frequencies (plot (b)) the 1 mm ($\lambda_y \geq 2$ mm) and 2 mm ($\lambda_y \geq 4$ mm) probes measure only ~2.4 and ~1.3 times the fluctuation amplitude of the reference probe ($\lambda_y \geq 13$ mm). At the lower frequencies (plot (a)) the small probes measure essentially the same power as the reference probe. The edge values of the low- and high-frequency fluctuation levels are $\sim 2 \cdot 10^{-4}$ and $\sim 3 \cdot 10^{-7}$. Inside the separatrix or at the higher frequencies the small-λ_y fluctuation levels rise faster than the long-λ_y or low-frequency fluctuation levels. The increase inside the separatrix of the high-frequency fluctuation amplitudes relative to the edge values (Figure 4.9(d)) is larger than that for the $q_a \approx 1$ discharges (Figure 4.4(d)). Outside the separatrix or in the low-frequency band the enhancement is reduced or does not exist. The reduction in the fluctuation amplitudes below x=7 or 8 cm that is evident in each plot in Figure 4.9 may be due to the perturbing effects of two probes on the plasma which were not evident in the global discharge characteristics. LaPointe[2] has observed that high-

frequency fluctuations are more sensitive to perturbation by probes than are low-frequency fluctuations.

A histogram showing the approximate distribution of power in k_y is given in Figure 4.10 in the same format as Figure 4.5. The histogram was generated from the spectra measured at x=8 cm (Figure 4.6), where the largest small-scale enhancement occurred. Because the enhancement of the small-scale fluctuations in the $q_a \approx 2$ discharges is much smaller than that in the $q_a \approx 1$ discharges (cf. Figures 4.2 and 4.4 with Figures 4.6 and 4.9), the k_y distribution shows little tendency to increase with k_y and shows no evidence of a peak at the c/ω_{pe} scales. The histograms at other x where the enhancement is smaller are similar to those in Figure 4.5(b).

$q_a \approx 3$ Results

The $q_a \approx 3$ discharges (with $\beta \sim 1\ m_e/m_i$) exhibited the smallest degree of small-scale fluctuation enhancement of all the discharges investigated. The largest enhancement occurred near the separatrix at x=9 cm and x=10 cm. Figure 4.11 shows the spectra measured by the probes at x=10 cm and the ratios of the 1 mm probe and 2 mm probe spectra to the 6.35 mm probe spectra. The frequency range of the strongest enhancement was 400 kHz $\lesssim f \lesssim$ 3 MHz with significant enhancement extending to ~200 kHz. This range is similar to that for the $q_a \approx 1$ and $q_a \approx 2$ discharges. The range of poloidal wavelengths $\lambda_y \geq 2$ mm resolved by the 1 mm probe contained only about 4 times more power than the range $\lambda_y \geq 13$ mm measured by the 6.35 mm probe. And the range of poloidal wavelengths $\lambda_y \geq 4$ mm resolved

by the 2 mm probe contained slightly more than twice the power of the range measured by the 6.35 mm probe. The enhancement measured by the 2 mm probe is barely larger than the factor of ~2 total uncertainty and may not be significant.

Outside the separatrix (Figure 4.12, x=11 cm), all three probes measured similar spectra (within the factor of ~2 total uncertainty) across both the low- and high-frequency bands. Above 2 MHz the spectra flatten indicating that the signal levels are close to the noise levels. Further evidence that the signal levels are small is the sharp, narrow peak at 5 MHz. The 5 MHz component is generated by the DSP2001A ("fast") digitizers and is only present while the digitizers are sampling. This component is actually a *small* (but significant) part of the high-frequency system noise level but appears quite prominently in the frequency spectra.

Due to the sensitivity of the $q_a \approx 3$ discharges to the large probe, data was taken with the 6.35 mm probe inserted only to x=9 cm and was then pulled out while the 2 mm and 1 mm probes were advanced to x=5 cm. Figure 4.13 shows the power spectra measured by the two small probes inside the separatrix at x=6 cm and the ratio of the 1 mm probe power to the 2 mm probe power. There is a slight tendency for the probes to measure different power levels. As with the $q_a \approx 2$ data, it is not known if the enhancement between the 6.35 mm probe and the smaller probes exists for x<9 cm.

Figure 4.14 summarizes the radial character of the $q_a \approx 2$ small-scale fluctuations in the same format as Figures 4.4 and 4.9. The enhancement is

largest near the separatrix and in the high-frequency band (plots (b) and (d)) but is smaller than in the $q_a \approx 1$ or $q_a \approx 2$ discharges. At the higher frequencies (plot (b)) the 1 mm ($\lambda_y \geq 2$ mm) and 2 mm ($\lambda_y \geq 4$ mm) probes measure only ~2.3 and ~1.2 times the fluctuation amplitude of the reference probe ($\lambda_y \geq 13$ mm). At the lower frequencies (plot (a)) the small probes measure essentially the same power as the reference probe. The edge values of the low- and high-frequency fluctuation levels are $\sim 3 \cdot 10^{-5}$ and $\sim 4 \cdot 10^{-7}$. The increase of the fluctuation levels inside the separatrix in both frequency ranges is similar to that for the $q_a \approx 1$ discharges (Figure 4.4). For $x \leq 6$ cm the discharges were perturbed by the two small probes. This may have caused the reduced fluctuation amplitudes inside the separatrix.

The approximate k_y distribution of power measured at x=10 cm (Figure 4.11) corresponding to the largest $q_a \approx 3$ enhancement is shown in Figure 4.15. As with the $q_a \approx 2$ discharges, because the enhancement is small the histogram shows no evidence of a peak at the c/ω_{pe} scales.

Short Radial Wavelength Dependence of the Fluctuation Enhancement

The results presented above were obtained with probes that had a similar overall radial wavelength response. A power comparison experiment was performed to investigate the effects of *coil length* on the difference in the measured spectra. The effect of coil length was studied using the two 2 mm probes listed in Table 2.2. One had a 2-layer coil that was 2.0 mm in length. The other had a 4-layer coil that was 0.6 mm in length. The shield parameters and, thus, the response of the probes to probe-transverse wavelengths were

identical. The minimum resolvable axial wavelength given by Eq. (2.10) (and summarized in Table 4.1) for the 2 mm probes is $\lambda_x^{\min}$=2.0 mm for the short-coil probe and $\lambda_x^{\min}$=6.6 mm for the long-coil probe. Assuming no toroidal asymmetries, any differences in the power measured by the two probes can be attributed to the different axial response functions resulting from different coil lengths.

Figure 4.16 shows the power spectra measured by the two 2 mm probes at x=6 cm in $q_a \approx 1$ discharges. In the range of plasma-radial wavelengths $\lambda_x \geq 2.0$ mm the short-coil probe measured ~3 times more power than in the range $\lambda_x \geq 6.6$ mm measured by the long-coil probe. Thus, there appears to be ~ρ_i-scale radial variations in the high-frequency magnetic turbulence in Tokapole II plasmas. The range of frequencies in which the enhanced fluctuations occur is 100 kHz $\leq f \leq$ 500 kHz, which is somewhat lower than the frequency range of the enhanced poloidal fluctuations. Outside the separatrix (at x=11 cm) there was no difference between the spectra measured by the two 2 mm probes. The spectra were similar in all respects to those in Figure 4.3 ($q_a \approx 1, x$=6 cm case).

The enhancement of the short radial wavelength fluctuations is summarized in Figure 4.17. The power measured in the different ranges of λ_x at x=6 cm for a few representative frequencies was converted into a k_x histogram similar to the k_y histogram in Figure 4.5. The area in the first bin ($k_y \leq 0.95$ rad / mm) represents the power measured by the long-coil 2 mm probe in the radial wavelength range $\lambda_x \geq \lambda_x^{\min} \approx 6.6$ mm. The total area in the first and second bins ($k_x \leq 3.1$ rad / mm) represents the power measured

by the short-coil 2 mm probe ($\lambda_x \geq \lambda_x^{\min} \approx 2$ mm). Even near the frequencies of the strongest enhancement (100 kHz < f < 600 kHz), the enhancement is not strong enough to produce an increase in the k_x distribution similar to that in the k_y distribution of Figure 4.5. The numerical simulation of the toroidal η_e modes (Section 3.4) predicted that the magnetic fluctuation spectra are isotropic in the poloidal and radial directions. The experimental results do not support this prediction. The enhancement associated with short *poloidal* wavelengths was a factor of ~8 between the ranges $\lambda_y \geq 4$ mm and $\lambda_y \geq 13$ mm, whereas the enhancement associated with short *radial* wavelengths was at most a factor of ~3 between ranges of radial wavelengths $\lambda_x \geq 2.0$ mm and $\lambda_x \geq 6.6$ mm with *smaller* lower limits. If the k_x spectrum of the fluctuations were similar to the k_y distribution of Figure 4.5 (isotropic in x and y), one might expect the radial-wavelength enhancement (Figures 4.16 and 4.17) to be *larger* than the poloidal-wavelength enhancement (Figures 4.2 and 4.5) because the minimum resolvable radial wavelengths were smaller than the minimum resolvable poloidal wavelengths.

4.3 Relation of Results to Theory and Computation

Although the results are suggestive, the short-wavelength magnetic fluctuation experiments performed to date cannot positively identify η_e mode activity as the cause of the observed spectral enhancement. The main reason is that there are many areas were the results of experiments and theory/computation either disagree or cannot be compared. In this section I will summarize the areas where the experiments and theory/computation

reviewed in Chapter 3 agree, disagree, or cannot be compared due to shortfalls in the experiments or the theory/computation.

Areas of Agreement

The experimental parameters overlap quite well with the assumptions of the theory of η_e microturbulence. To our knowledge, no other microturbulence model offers a better match of assumption and experimental parameters than the η_e theories. And, to our knowledge, no other model predicts electromagnetic fluctuations between ρ_{ei} and ρ_s scales, as were observed in the experiments described above.

The experimental scale lengths are comfortably separated and are suitable for looking for η_e mode activity:

$$\rho_{ei} << \lambda^{min}_{1\ mm\ prb} \lesssim \rho_i \sim \lambda^{min}_{2\ mm\ prb} < c/f_{pe} < \lambda^{min}_{6.35\ mm\ prb} < \lambda_{\eta_i\ modes}. \quad (4.1)$$

The minimum resolvable poloidal wavelength for the 1 mm probe is much larger than the electron gyroradius but is slightly smaller than the ion gyroradius. The c/f_{pe} wavelength lies between the minimum resolvable poloidal wavelengths for the 2 mm and 6.35 mm probes, all of which lie between the ion gyroradius and the wavelengths at which η_i modes are predicted to be active.

The assumption of an adiabatic ion response ($\lambda_\perp < \rho_i$), though not required, is marginally satisfied for the wavelengths of the strong enhancement ($\lambda^{min}_{1\ mm\ probe} \sim 0.8\,\rho_i$). The assumption of non-adiabatic

electrons ($\omega / k_\parallel v_e > 1$), which *is* required, is satisfied over most of the range of enhancement: $\omega / k_\parallel v_e \gtrsim 1$ for $f \gtrsim 0.5$ MHz if $k_\parallel = 1/qR$. The high-density limit ($\omega_{pe}/\omega_{ce} >> 1$) assumed by the reduced nonlinear η_e model equations is also marginally satisfied ($\omega_{pe}/\omega_{ce} \sim 2-4$).

The frequency range of the enhanced short poloidal wavelength radial fluctuations (0.4 MHz $\lesssim f \lesssim$ 4 MHz) is consistent with range of ω_r in which η_e modes are predicted to be linearly unstable ($\omega < 0.3\ \omega^*_{ne}$, or $f < 1$ MHz). And the range of poloidal wavelengths associated with the strongest enhancement is located near the c/ω_{pe} scales as the nonlinear computation suggests.

In Tokapole II, β falls from $\sim 10\ m_e/m_i$ in $q_a \approx 1$ discharges to $\sim 1\ m_e/m_i$ in $q_a \approx 3$ discharges. This fact taken together with the result that the levels of enhancement fall rapidly with increasing q_a is consistent with the prediction that the magnetic component of the microturbulence becomes less important as β falls toward m_e/m_i.

Areas of Disagreement

Perhaps the most obvious area of disagreement is between the measured enhanced fluctuation levels and the mixing length estimates of the fluctuation levels which are reported to agree with the computational results. The fluctuation levels for the case of the strongest spectral enhancement was *at most* $\tilde{B}_r/B \sim 5 \cdot 10^{-5}$ ($q_a \approx 1$, x=5–6 cm, f>500 kHz). However, the mixing length estimate given by Horton, et al. (Section 3.4) gives $\tilde{B}_r/B \sim k_\parallel c/\omega_{pe} \sim 10^{-3}$ if $k_\parallel = 1/qR$. The factor of ~ 20 disagreement may be due in part to the fairly

low β values of Tokapole II plasmas which would tend to produce low values of $\tilde{B}_r/B$. However, the experimental β for $q_a \approx 1$ discharges is only about half that used in the nonlinear simulations. The use of unrealistic and mutually inconsistent values for the plasma parameters and diffusion coefficients in the nonlinear simulations (Section 3.4) may be related to the large values of $\tilde{B}_r/B$.

Some of the discrepancy may be related to the wavelength-dependence of the response functions shown in Figure 2.8. The response of the probe falls to zero as the poloidal or axial wavelengths decrease below some cutoff value for each term in the response. In Sections 2.4.2 and 4.2 the cutoff was chosen to be at the 1/2-amplitude wavelength. The wavelength-dependent attenuation could not fully be taken into account in the analysis of the data. Therefore, at short wavelengths near the cutoff, the actual values of $\tilde{B}_r(\omega)$ and $\tilde{B}_r/B$ are *larger* than the measured values by some wavelength dependent factor. The difference between the measured (k-averaged) and actual values is small if the actual wavenumber spectrum varies gradually at short wavelengths near and below the cutoff. If the actual wavenumber spectrum is rapidly increasing below the cutoff, then the probes could not resolve the short-wavelength power and the error would be larger.

Another area of obvious disagreement is the location of the increase in the k_y spectra. Neither the experiments performed here nor the nonlinear computation described in Section 3.4 could demonstrate the existence of a peak in the k_y spectra (cf., Figures 4.5 and 3.12). The simulated spectrum (Figure 3.12) increases near $k_y = \omega_{pe}/c$ (and perhaps at yet smaller k_y),

while the measured k_y spectrum increases near $k_y = 2\pi/\rho_i$, well above $k_y = \omega_{pe}/c$. It was argued in Section 3.4 that the 'peak' in the simulated spectrum may actually be located *below* $k_y = \omega_{pe}/c$. If this is were the case, the discrepancy between the measured and simulated spectra would be even larger.

The dependence of the magnetic fluctuations on poloidal and radial wavelengths is similar in that there are significant short(ρ_i)-scale variations in both the poloidal and radial components. However, the degree of the enhancement of the poloidal and radial components of the fluctuations and the ranges of f and λ over which the enhancement occur are not similar. This can be seen by comparing the k_y distribution (Figure 4.5) with the k_x distribution (Figure 4.17). Thus, the isotropy of the turbulence in the x and y directions that is predicted by the η_c simulations (Section 3.4) is not supported by the experimental results. In the future, a systematic study of the short radial wavelength character of the turbulence should be carried out to provide more complete experimental information on this issue.

Areas Where No Comparison Can Be Made

Because of several shortfalls in both experiment and theory/computation there are several areas in which no comparison can be made.

Shortfalls of Experiment

With the present mini- and micro-probe technology and the experimental techniques described in Section 4.1, one cannot resolve poloidal or radial

wavelengths smaller than ρ_i. Because of this limitation, the experiments described here could neither prove nor disprove the existence of a peak in the poloidal wavenumber distribution (Figure 4.5). All that can be inferred from Figure 4.5 is that the k_y spectra corresponding to maximum enhancement increases at ρ_i spatial scales, well below the c/f_{pe} scales at which the simulated spectra reportedly peak (Section 3.4).

Another limitation of the present method is its inability to generate wavenumber spectra. To measure k_y spectra, for example, would require at least two identical shielded small coils. Constructing the probes is one difficulty in measuring the k_y spectra. Another is that the probes must be spaced very closely, separated by at most *half* the smallest λ_y one wishes to resolve (Nyquist sampling theorem).

According to the nonlinear simulations, a signature of the η_e modes is a transfer of fluctuation energy from ρ_e to c/ω_{pe} scales as the modes enters saturation. A diagnostic that could identify such a signature would be very powerful, indeed. However, measurements of fast-growing microturbulence modes in laboratory plasmas must be assumed to be made in the fully saturated state. Therefore, experiments cannot observe the characteristics of the linear growth, saturation and transfer of energy in k-space that are predicted by various microturbulence models. Currently, the best one can only hope to do is measure the nonlinear coupling in the *saturated* state of the turbulence. This limitation applies to all present fluctuation diagnostics.

The direction of propagation of the fluctuations measured could not be determined. The frequency measurements made in these experiments do

not take into account the Doppler shift due to $E \times B$ rotation of the plasma in the toroidal or poloidal directions. There was no information available on the equilibrium electric field or the plasma rotation.

Shortfalls of Theory / Computation

The nonlinear simulations cannot accommodate wavelengths longer than c/ω_{pe} because of the assumption of adiabatic ion response. In addition, the simulations run to date show that the k_y spectra of magnetic fluctuation power increases as k_y decreases toward the c/ω_{pe} scales but cannot positively identify a peak in the spectra. As the size of the simulation grid is made larger to permit smaller k_y, the "peak" in the spectra moves to the largest scale of the box (Section 3.4). If the restriction on the ion response can be removed, perhaps the simulations can resolve the unanswered questions about the reality of the peak.

The simulations that have been run to date leave other questions unanswered as well. What do the frequency spectra of the saturated magnetic fluctuations look like? Do the real frequencies of $\tilde{B}_r$ shift to lower values as the turbulence saturates and the k-spectra peak shifts to smaller k? How do the frequency spectra of the other model variables change as the mode enters saturation? How well does the linear k spectra of ω_r represent the saturated spectra? Because the time histories of the simulation variables were not saved, these questions remain unanswered. Because the simulations generate primarily k spectra and the experiments generate primarily frequency spectra, direct comparison between experiment and simulation

is limited.

Comparison of simulation and the experiment can be made easier if spectra, for example, of experimentally measurable quantities were generated rather than spectra of 'mixed' quantities such as those given in Eq. (3.8). Horton and coworkers have responded by separating the k spectra of $\widetilde{B}_{\perp}$ from the spectra of $E\,\widetilde{A}_{\parallel}$. It would be interesting to compare spectra of $\widetilde{\phi}$ and $\widetilde{T}_e$ from simulation and experiment as well. It also would be interesting to see the results of the nonlinear simulations run with realistic and mutually consistent plasma parameters and diffusion coefficients. This issue was discussed in greater detail at the end of Chapter 3.

Finally, the current η_e theories and simulations are not self-consistent. They do not take into account the spatial or temporal variations in η_e caused by variations in n_e or T_e that would accompany fully turbulent plasmas. To our knowledge, no model has yet been proposed which adequately takes such refinements into account.

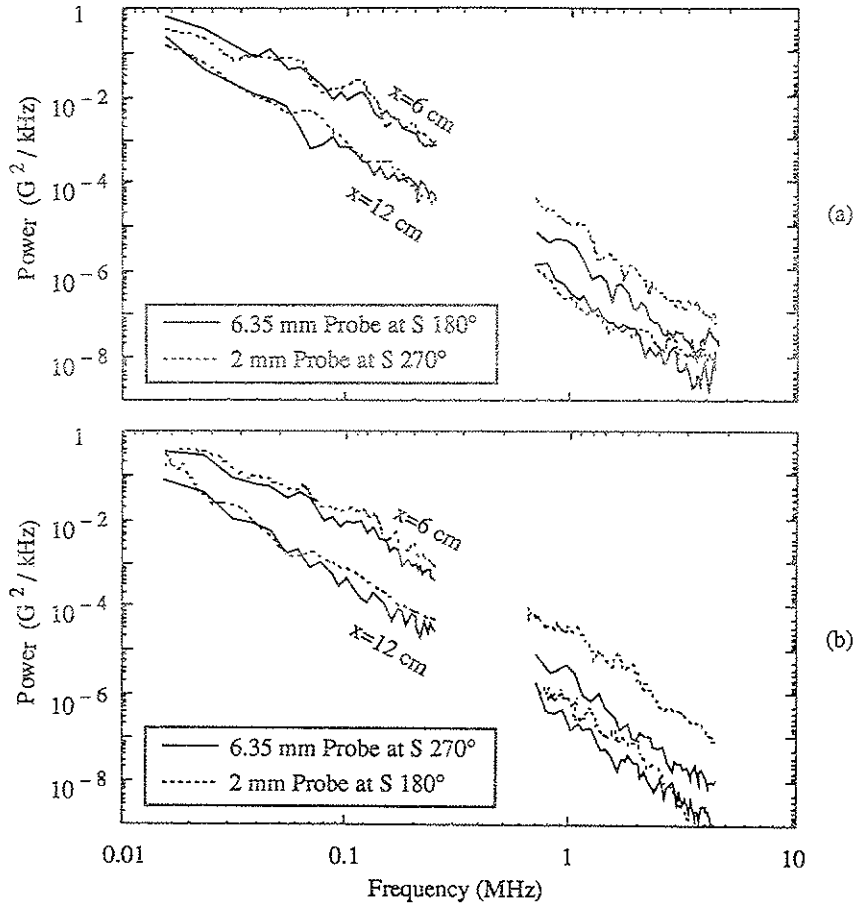

Figure 4.1. Test of toroidal symmetry. Spectra measured by 6.35 mm and 2 mm probes at x=6 and 12 cm with probes at (a) 180° and 270°, respectively. (b) Probes were then swapped to locations at 270° and 180°, respectively. Probes at 180° tended to measure slightly more power.

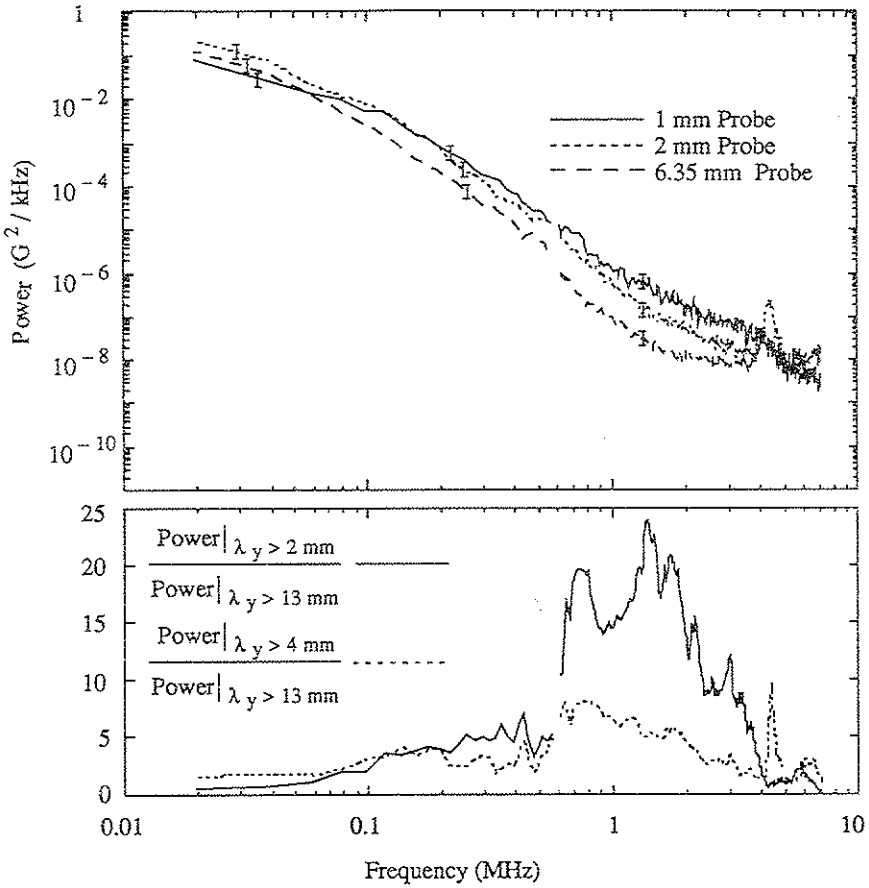

Figure 4.2. $q_a \approx 1$, x=6 cm
Top: Power spectra measured by each probe. Error bars indicate factor of ~2 overall uncertainty. Bottom: The ratios of small probe power to large probe power for the two smaller probes show the enhancement of fluctuations at small spatial scales.

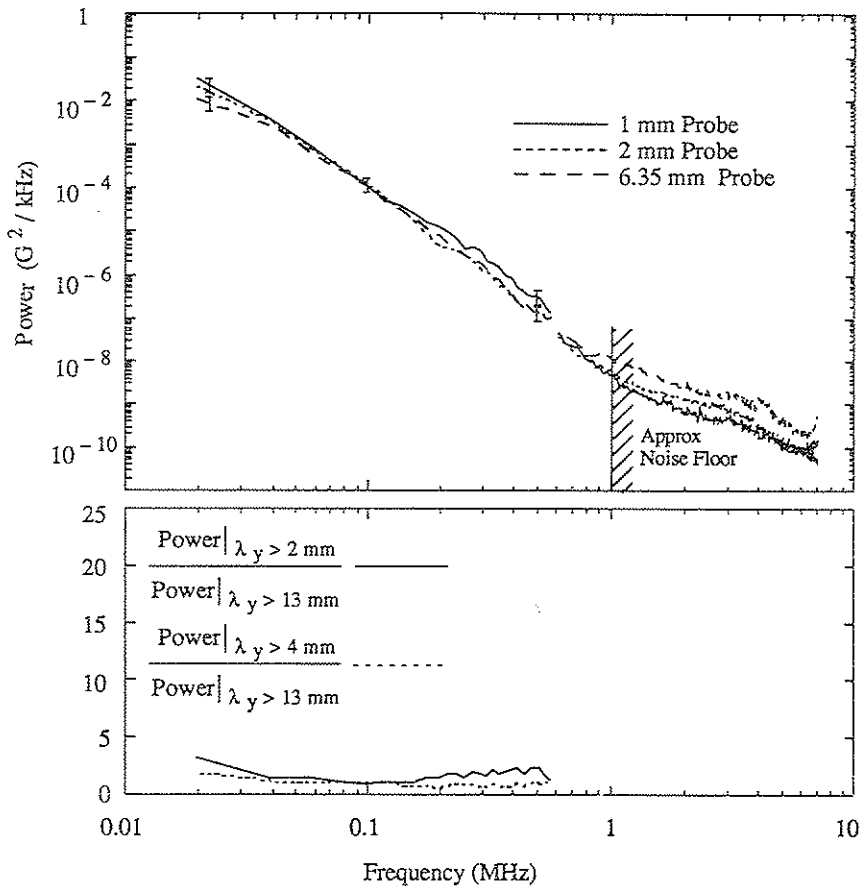

Figure 4.3. $q_a \approx 1$, x=11 cm
Top: Power spectra measured by each probe. Error bars indicate factor of ~2 overall uncertainty. Frequencies where the noise dominates the signal are indicated. Bottom: The ratios of small probe power to large probe power for the two smaller probes show no significant enhancement outside the separatrix.

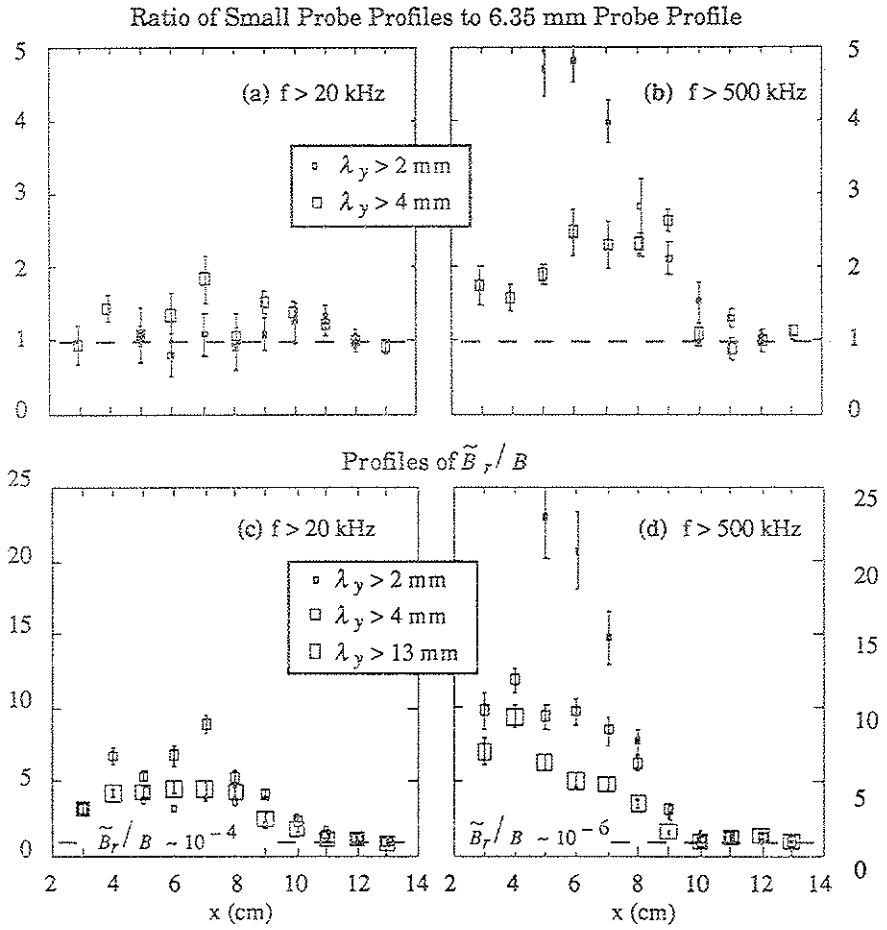

Figure 4.4. $q_a \approx 1$ fluctuation profiles in the low- and high-frequency ranges. Ratios of small-probe profiles to the 6.35 mm probe profiles, (a) and (b), show the enhancement as a function of x. The profiles of $\tilde{B}_r / B$ are shown in plots (c) and (d) in units of the common value at the edge. The edge values of $\tilde{B}_r / B$ are indicated by the dashed line in (c) and (d).

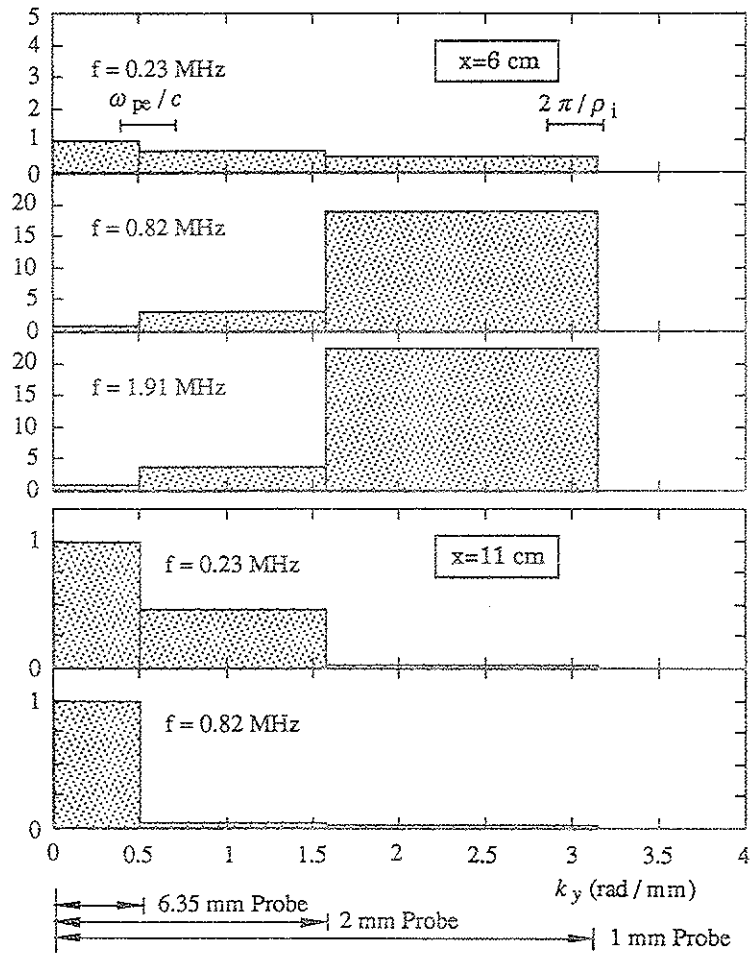

Figure 4.5. $q_a \approx 1$, x=6 & 11 cm
Approximate k_y distribution of fluctuation power inferred from three ranges of λ_y resolved by the probes. Bin heights are normalized to height of the first bin. Note change of vertical scales. The c/ω_{pe} and ρ_i scales are indicated.

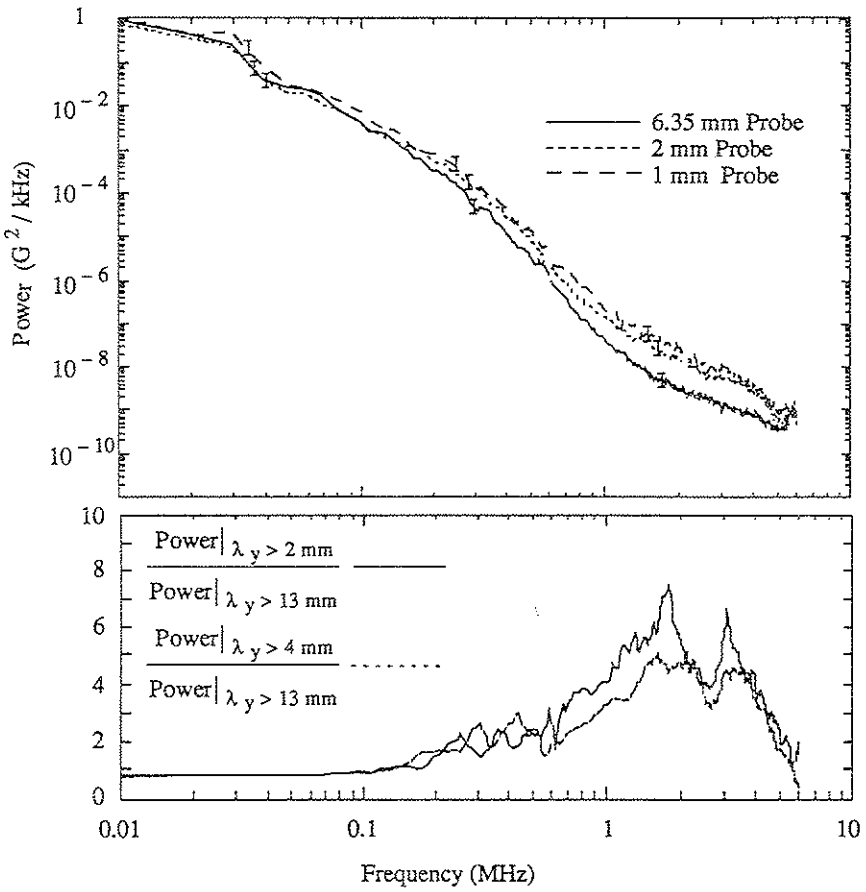

Figure 4.6. $q_a \approx 2$, x=8 cm
Top: Power spectra measured by each probe in the region of greatest enhancement for the $q_a \approx 2$ discharges. Error bars indicate factor of ~2 overall uncertainty. Bottom: The ratios of small probe power to large probe power for the two smaller probes show less enhancement than the $q_a \approx 1$ case, Figure 4.2.

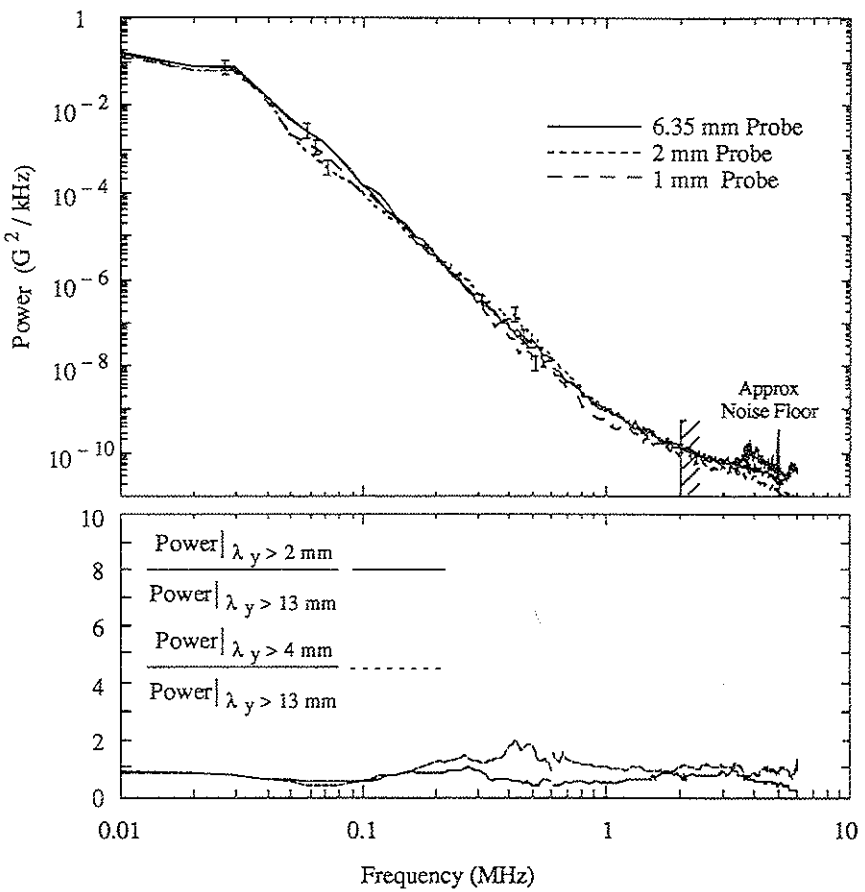

Figure 4.7. $q_a \approx 2$, x=11 cm
Top: Power spectra measured by each probe. Error bars indicate factor of ~2 overall uncertainty. Frequencies where the noise dominates the signal are indicated. Bottom: The ratios of small probe power to large probe power for the two smaller probes show no significant enhancement outside the separatrix. (cf. Figure 4.3.)

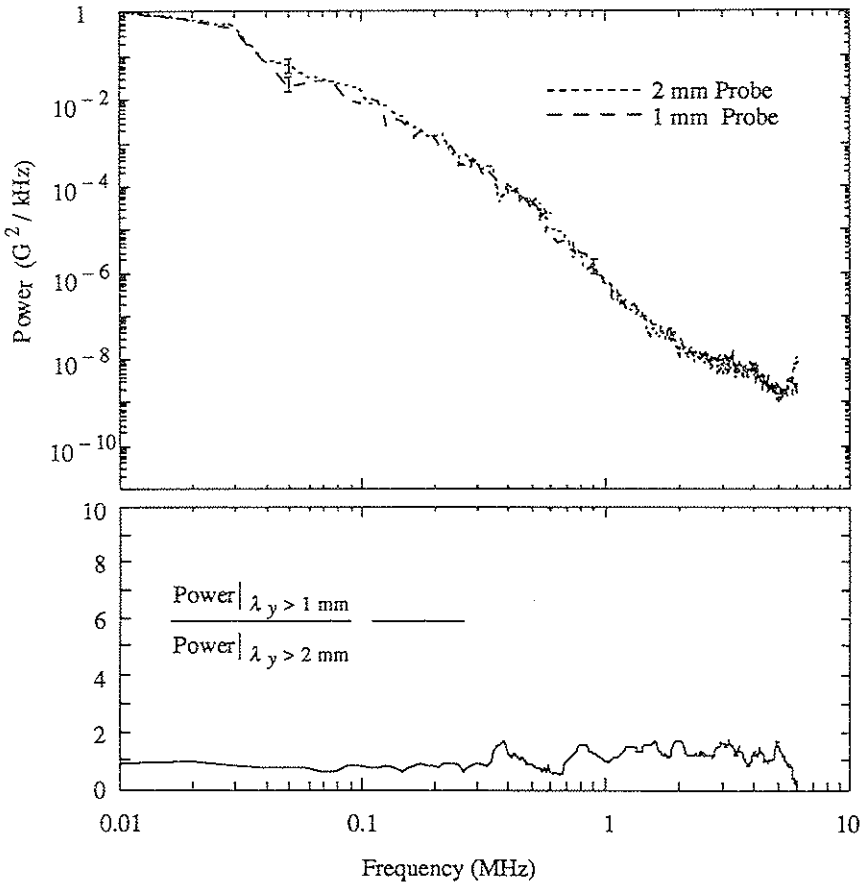

Figure 4.8. $q_a \approx 2$, x=6 cm
Top: Power spectra measured by the two small probes. Error bars indicate factor of ~2 overall uncertainty. Bottom: The ratio of 1 mm probe power to the 2 mm probe power shows no significant enhancement inside the separatrix in contrast to Figure 4.2.

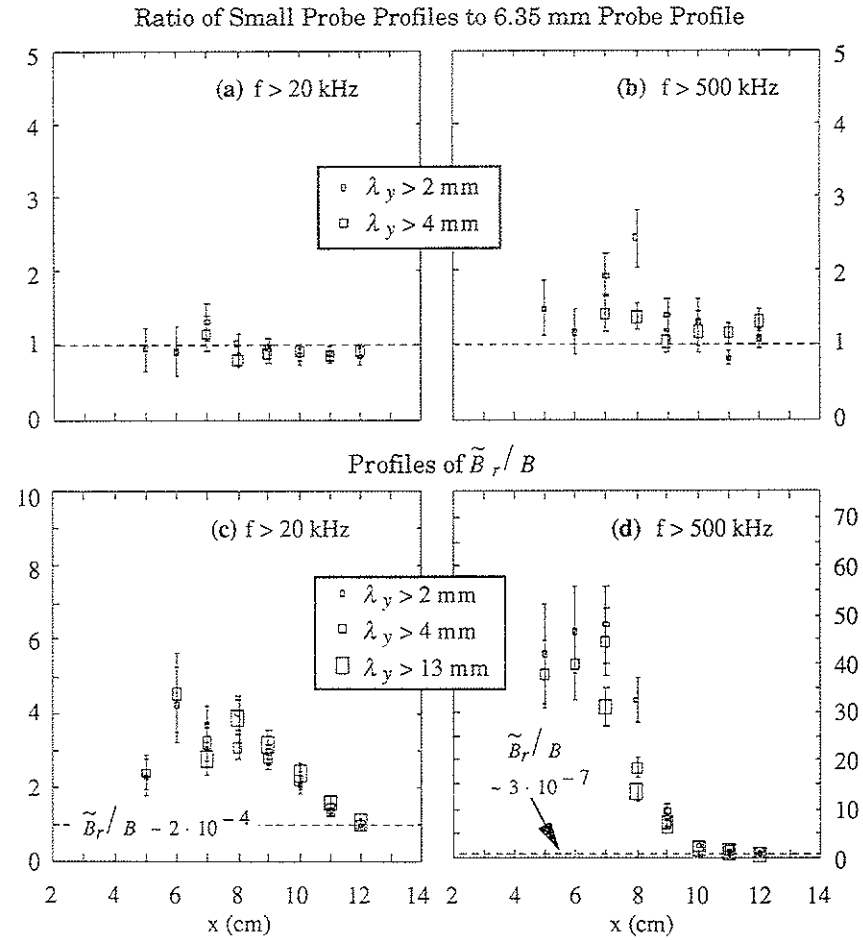

Figure 4.9. $q_a \approx 2$ fluctuation profiles in same format as Figure 4.4.

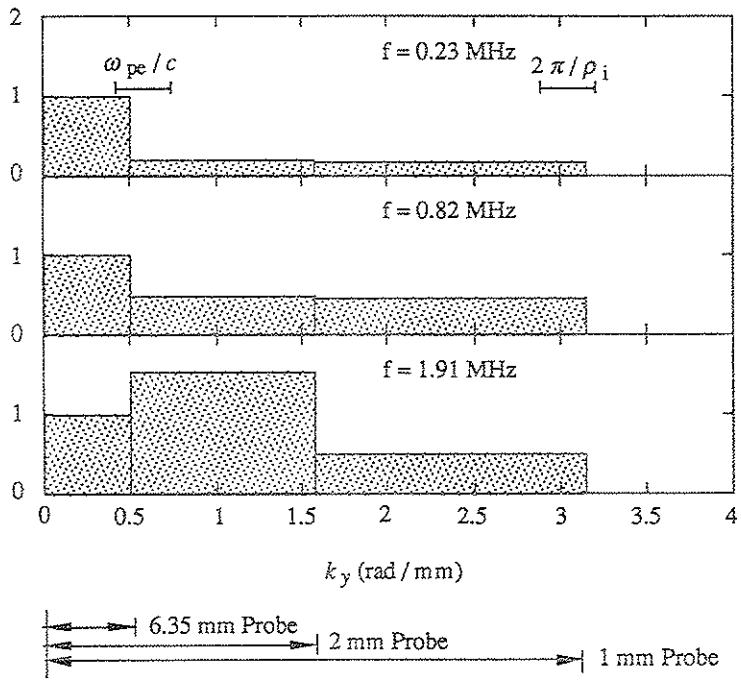

Figure 4.10. $q_a \approx 2$, x=8 cm
Approximate k_y distribution of fluctuation power inferred from three ranges of λ_y resolved by the probes. Bin heights are normalized to height of first bin. The c/ω_{pe} and ρ_i scales are indicated.

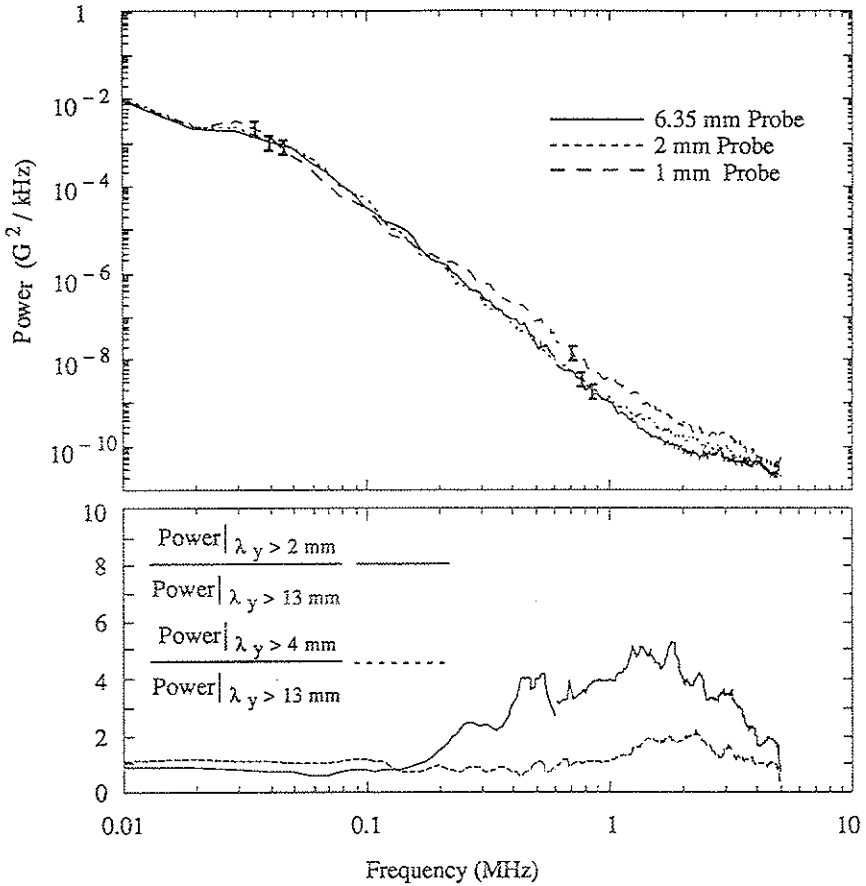

Figure 4.11. $q_a \approx 3$, x=10 cm
Top: Power spectra measured by each probe in the region of greatest enhancement for the $q_a \approx 3$ discharges. Error bars indicate the factor of ~2 overall uncertainty. Bottom: The ratios of small probe power to large probe power for the two smaller probes show less enhancement than the $q_a \approx 1$ (Figure 4.2) and $q_a \approx 2$ (Figure 4.6) cases.

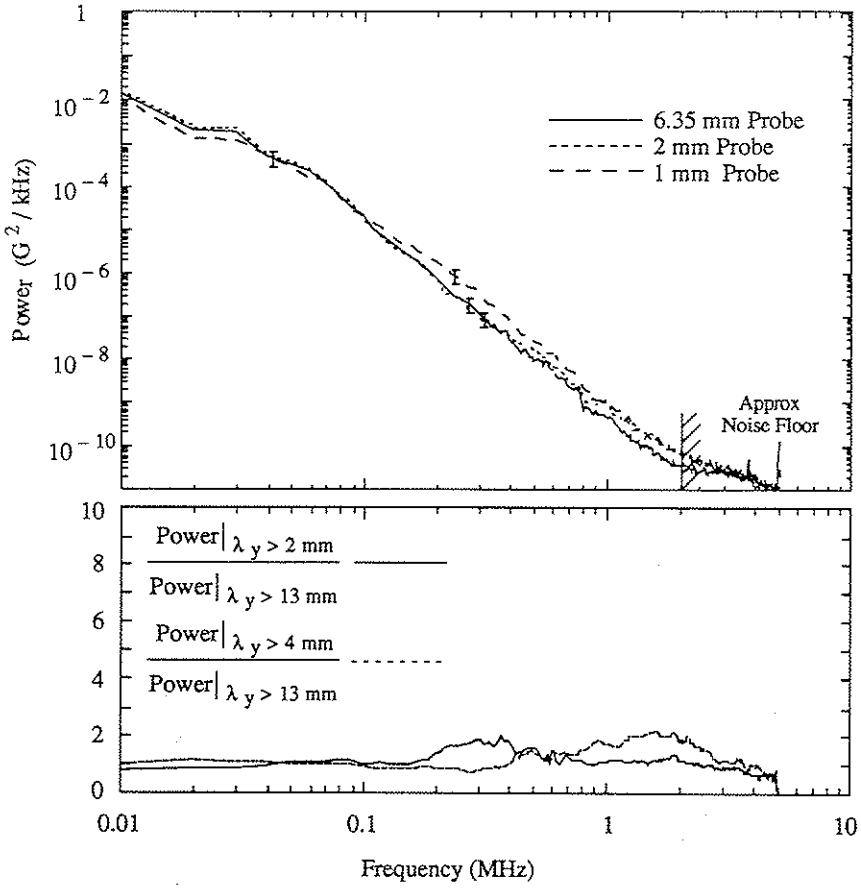

Figure 4.12. $q_a \approx 3$, x=11 cm
Top: Power spectra measured by each probe. Error bars indicate the factor of ~2 overall uncertainty. Frequencies where the noise dominates the signal are indicated. Bottom: The ratios of small probe power to large probe power for the two smaller probes show no significant enhancement outside the separatrix. (cf., Figures 4.3 and 4.7.)

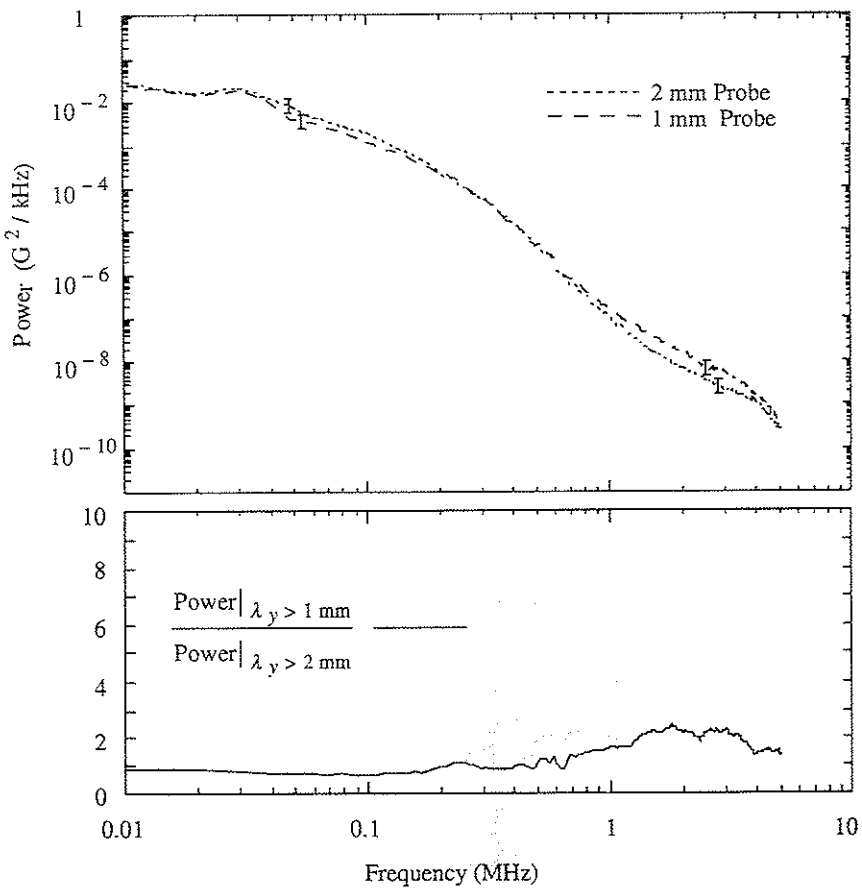

Figure 4.13. $q_a \approx 3$, x=6 cm
Top: Power spectra measured by the two small probes. Error bars indicate factor of ~2 overall uncertainty. Bottom: The ratio of 1 mm probe power to the 2 mm probe power shows only a slight enhancement inside the separatrix.

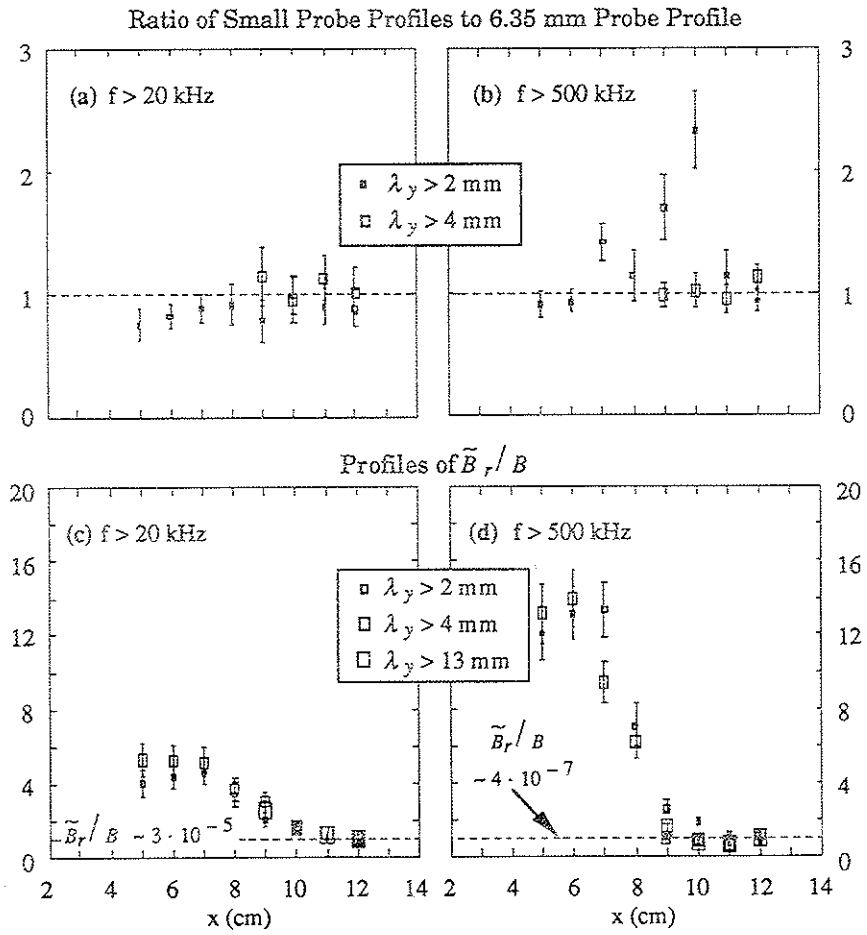

Figure 4.14. $q_a \approx 3$ fluctuation profiles in the same format as Figures 4.4 and 4.9.

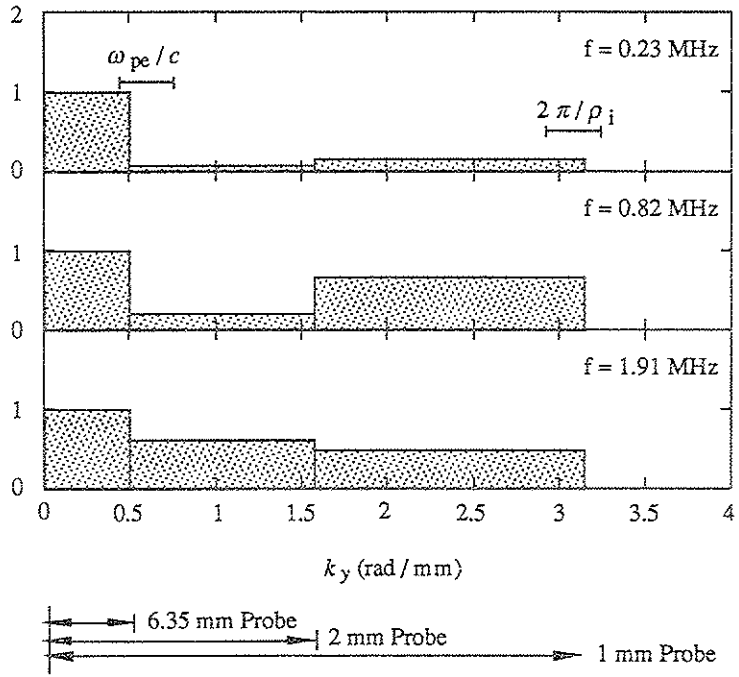

Figure 4.15. $q_a \approx 3$, x=10 cm
Approximate k_y distribution of fluctuation power inferred from three ranges of λ_y resolved by the probes. Bin heights are normalized to height of the first bin. The c/ω_{pe} and ρ_i scales are indicated.

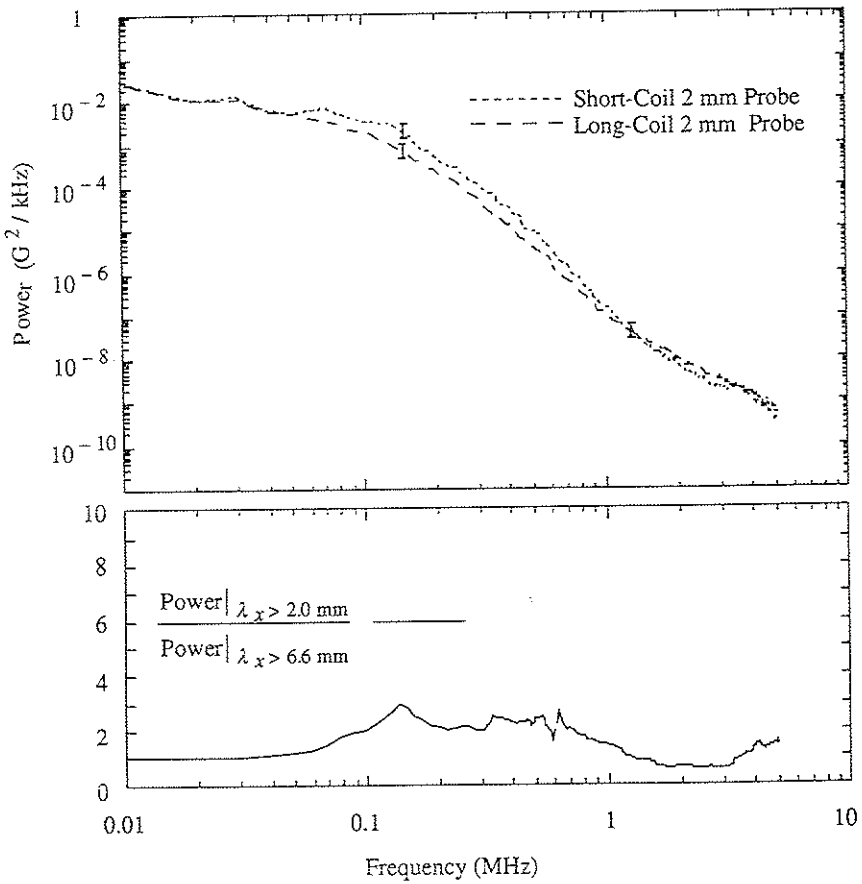

Figure 4.16. $q_a \approx 1$, x=6 cm, Effect of Coil Length
Power spectra measured by two 2 mm probes with different coil lengths. The short-coil 2 mm probe ($\lambda_x \geq 2.0$ mm) measures about 3 times more power at higher frequencies than the long-coil 2 mm probe ($\lambda_x \geq 6.6$ mm) indicating the presence of a short-scale variation in the radial component of the magnetic turbulence.

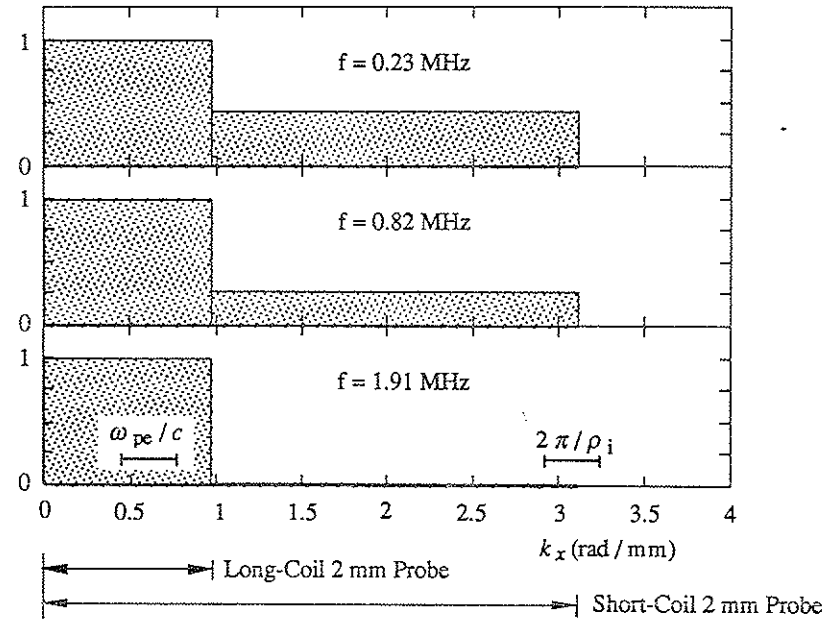

Figure 4.17. $q_a \approx 1$, x=6 cm, Effect of Coil Length
Approximate k_x distribution of fluctuation power inferred from two ranges of λ_x resolved by the probes. Bin heights are normalized to height of the first bin. The k_x distribution is not similar to the k_y distribution (Figure 4.5) at the same location in the same discharges. Thus, the fluctuations do not appear to be isotropic in x and y.

References

[1] D. E. Graessle, Ph.D. Thesis, University of Wisconsin–Madison, (1989).

[2] M. A. LaPointe, Ph.D. Thesis, University of Wisconsin–Madison, (1990).

[3] I. H. Tan, R. N. Dexter, S. C. Prager and T. D. Rempel, Bull. Amer. Phys. Soc. 34 poster 1Q9, 1923 (1989).

CHAPTER 5

Summary

5.1. Summary of Results

Smaller probes measured higher fluctuation power levels for high frequencies (~ 0.6 MHz to ~ 3 MHz) and ρ_i-scale poloidal and radial wavelengths in Tokapole II discharges. The scale length of the increased magnetic fluctuation power contradicts the result of the nonlinear simulations that the location of increased power lies near c/f_{pe}. The strongest increase of the short-scale poloidal fluctuations was found in the low-q_a ($q_a \approx 1$), relatively high β ($\beta \sim 10\ m_e/m_i$) discharges inside the separatrix and at frequencies just below the electron diamagnetic drift frequency ω^*_{ne} ~ 3 MHz (evaluated for $\lambda_y \sim \rho_i$). Table 5.1 summarizes the main features of the short poloidal wavelength power comparison experiments. As q_a increased from ~ 1 to ~ 3, the value of β decreased from ~ $10\ m_e/m_i$ to ~ $1\ m_e/m_i$, and the degree of enhancement decreased sharply from a factor of ~ 10 to 20 to less than a factor of 4. This is consistent with the prediction that the magnetic component of the microturbulence becomes less important as β falls toward m_e/m_i. As q_a was increased, the radial location of the strongest increase moved from inside the separatrix to near the separatrix. The range of frequencies associated with significant levels of increase (> factor of 2) was fairly broad, spanning nearly a decade from ~400 kHz to ~3 MHz. This is consistent with the linear η_e mode theories which predict the modes to be unstable over a wide range of frequencies below the diamagnetic drift

frequency (Sections 3.3.1, 3.3.2, and the LINEIGS results of Section 3.3.3).

	Range of Largest Increase		Magnitude of Increase of Small-Probe Power Relative to 6.35 mm Probe Power	
q_a	x (cm)	f (MHz)	1 mm Probe	2 mm Probe
1	6	0.6–3	~20	~8
2	8 *	0.6–4	~5	~4
3	10 *	0.3–3	~4	$\lesssim 2$

Table 5.1. Summary of main results of the power comparison experiments. * The radial location of the greatest enhancement for $q_a \approx 2$ and $q_a \approx 3$ is indefinite due to plasma perturbation uncertainties and because there is no 6.35 mm probe comparison information for $x<7$ cm.

Short, ρ_i-scale *radial* variations have also been observed inside the separatrix but with an intensity that is weaker than for the poloidal component and at somewhat lower frequencies in the range 100 kHz $\lesssim f \lesssim$ 500 kHz. Though there are significant short(ρ_i)-scale variations in both the poloidal and radial components of the magnetic fluctuations, the degree of increase and the ranges of f and λ over which the increase occurs are not similar. Thus, the experimental results obtained to date do not support the prediction of the η_e simulations (Section 3.4) that the turbulence is isotropic in the x and y directions.

As the magnetic probes become smaller and are able to resolve smaller

poloidal (or radial) wavelengths, presumably the increase in the short-wavelength fluctuations will saturate. The fluctuations cannot persist with increasing strength down to arbitrarily short wavelengths. As Table 5.1 suggests, no tendency toward saturation was observed in the $q_a \approx 1$ discharges over nearly a factor of 6 in the range of minimum resolvable poloidal wavelengths above and near the ρ_i scales. However, the $q_a \approx 2$ discharges (and, to a lesser extent, the $q_a \approx 3$ discharges) tended to show a smaller increase in the short-wavelength enhancement, suggesting that very little extra power is contained in the range of wavelengths between the minimum resolvable wavelengths of the two smallest probes for those discharges. Whether this decrease in relative enhancement with increasing q_a is due to the variation of q_a or the variation of β is difficult to say.

Though the small-probe power spectra were increased by an order of magnitude or more compared to the large-probe spectra in the high-frequency range, the power levels were still far below those in the low-frequency range. Thus, the transport caused by the enhanced small-scale fluctuations is too small to compete with transport due the low-frequency magnetic or electrostatic fluctuations. The magnetic fluctuation level $\tilde{B}_r/B$ under conditions of maximum enhancement and the mixing length estimate differ by a factor of 20 or so. Some of the discrepancy may be related to the wavelength-dependence of the response functions. At short wavelengths the attenuation due to spatial averaging becomes significant, and the actual values of $\tilde{B}_r(\omega)$ and $\tilde{B}_r/B$ are *larger* than the measured values by some wavelength dependent factor. The difference between the measured and actual k-averaged

values is small if the actual wavenumber spectrum varies gradually at short wavelengths. The fairly low β values of Tokapole II plasmas may also contribute to low experimental values of $\tilde{B}_r / B$. The unrealistic and mutually inconsistent values for the plasma parameters and diffusion coefficients used in the nonlinear simulations (Section 3.4) may be related to the large values of $\tilde{B}_r / B$.

5.2. Suggestions for Future Work

At present the comparison of experimental results and theory cannot give a definite identification of η_e modes in Tokapole II plasmas. Several reasons for this relating to various shortfalls of experiment and theory were pointed out in Section 4.3. In addition, there are three general areas in which the experiments might be improved to aid the comparison between experiment and theory/computation: the probes and data acquisition hardware, the data that is acquired, and analysis of the data.

First, the construction of even smaller probes and better electronics systems is needed. The type of probes described in Chapter 2 have been made about as small as can be. Further miniaturization is limited by the availability of coil forms, the ability to machine electrostatic shields, etc. Coil forms smaller than 0.1 mm are difficult to wind by hand, even with the smallest wire, because the wire becomes very stiff at such small radii of curvature. A new approach to micro-probe construction will likely be required. If possible, the probe parameters should be chosen in accordance with Section 2.4.2 to more closely match the overall axial wavelength response of a set of

probes used to make comparisons at small poloidal wavelengths. As probes become smaller the effective area of the coil shrinks and the need for more gain at the high frequencies increases. The limitations associated with the low digitizer resolution and relatively high amplifier noise in the high-frequency system (discussed at the end of Section 2.4.3) should be overcome, perhaps with a new low-noise, high-gain amplifier design.

Second, a more complete set of data should be acquired. The difficult task of measuring the poloidal and radial wavenumber spectra should be attempted. The k spectra would give important information about the direction of propagation and the dispersion relation of the fluctuations. The wavelength response predicted in Section 2.4.2 should be verified, if possible. The measured k spectra could also be more completely corrected for the k-dependent probe effects giving a more accurate and consistent picture of the turbulence. A more complete study of the short axial wavelength character of the fluctuations should also be undertaken.

Third, more sophisticated data analysis techniques should be applied. The possibility that nonlinear mode coupling plays a role in the enhancement could be assessed by applying bispectral analysis techniques.